PERIODIC HYDRAULIC TESTS IN A FRACTURED CRYSTALLINE BEDROCK

A THESIS

Presented to the Department of Geological Sciences

California State University, Long Beach

In Partial Fulfillment

of the Requirements for the Degree

Master of Science in Geology

Committee Members:

Matthew Becker, Ph.D. (Chair)
Benjamin Hagedorn, Ph.D.
Nate Onderdonk, Ph.D.

College Designee:

Rick Behl, Ph.D.

By Matthew C. Cole
B.S., 2014, California State University, Long Beach
January 2018

ABSTRACT

PERIODIC HYDRAULIC TESTS IN A FRACTURED CRYSTALLINE BEDROCK

By

Matthew C. Cole

January 2018

A better understanding of groundwater flow through bedrock fractures is critical to applications involving heat and solute transport. Pumping tests performed to characterize these systems are often ill-suited because the radius of penetration quickly expands beyond the inter-well distance, gaining information beyond the well pair of interest. Periodic hydraulic tests allow the radius of penetration to be controlled by the frequency of oscillation, and testing at multiple frequencies gives parameter estimates for a range of spatial scales. Periodic pumping tests were performed at the Mirror Lake experimental fractured rock hydrology field site in New Hampshire. Results suggest a more complex, 3D network of connectivity than previously indicated by constant rate pumping tests. The relative degree of connectivity, given by diffusivity, corresponds to early-time response seen in the constant rate test. This confirms that the periodic tests investigated at a smaller penetration radius than the steady response from constant pumping.

ACKNOWLEDGEMENTS

First and foremost, I owe a debt of gratitude to my advisor, Matt Becker, for the opportunity to conduct this research. His guidance and expertise gave me a solid foundation in the early stages of this field. He managed to instill the importance of hard work and perseverance while at the same time introduce me to self-motivation through his laissez-faire advising style. As a research assistant, I was afforded the opportunity to help him with various projects that brought me to field sites around the world.

Second, I thank all who played a part in this research, especially Chris Ciervo, Thomas Coleman, and Adam Hawkins, for all their hard work in the field. I also thank my fellow grad students who made these past years such a memorable experience. Helpful comments and advice from my committee members, Ben Hagedorn and Nate Onderdonk, were greatly appreciated in writing this thesis.

Finally, I tip my hat to everyone in CSULB Geology. It was a pleasure spending so many years both as an undergrad and grad student involved in this department. The Geology department attracts an eclectic group of students and faculty. From math nerds to rock geeks to field nappers, everyone involved brings a unique perspective, leading to a positive learning environment, teaching valuable life lessons, and creating countless memories. To everyone that has been a part of my time here: rock on.

CONTENTS

Abstract ii

Acknowledgements iii

List of Tables vi

List of Figures vii

Chapter 1 1

Introduction 1

- Motivation 1
- Background 1

Chapter 2 4

Previous Work 4

- Current Standard Methods 4
- Periodic Hydraulic Tests 5
- Period Dependence of Estimated Hydraulic Parameters 8

Chapter 3 12

Site Description 12

- Overview 12
- Geology 13
- Fractures 15
- Hydrologic Setting 18

Chapter 4 21

Methods 21

- Experiment Setup 21
- Sinusoidal Tests 28
- Data Analysis 29
  - Analytic Solutions 29
  - Frequency Domain Analysis 34

Chapter 5 38

Results 38

- Head Responses 38
- Frequency Domain Analysis 44
  - Amplitude and Phase Values 46
  - Ambiguous Responses 49
  - Comparing phase lag and attenuation 55

Parameter Estimation 62
Chapter 6 70
Discussion 70
Discussion of method 70
Period dependence 72
Formation Information 80
Chapter 7 84
Conclusion 84
Appendix A: Standard operating procedure for periodic pumping using voltage control 86
Datalogger and Voltage Module Setup 87
VFD Setup 89
Program Text for CRBasic Editor 90
Appendix B: Matlab code and data files 92
References 93

LIST OF TABLES

Table 1. Summary Table of Results from Field Studies Utilizing Periodic Hydraulic Tests in Fractured Bedrock Formations 9
Table 2. Characteristics of Fractures Significant to Flow 21
Table 3. Well Equipment Summary 24
Table 4. Setup and Parameters for VFD Controller 26
Table 5. Summary of Amplitudes Calculated Using FFT 46
Table 6. Summary of Attenuations (amplitude/injection rate) 47
Table 7. Summary of Phases Calculated Using FFT 47
Table 8. Summary of Phase Lags Calculated from Phases (above) 48
Table 9. Summary of Phase Lags After Corrections of 2π (*) 48
Table 10. Parameter Estimates 67

LIST OF FIGURES

Figure 1. Map of northeastern states showing HBEF (top right), topographic map of Mirror Lake basin (left), and grid showing layout of FSE well field (bottom right) 13

Figure 2. Map of North America and last maximum extent of Laurentide Ice Sheet. Modified from Berger (2013). 14

Figure 3. Segment of roadcut map created by Barton et al. (1997). Green is schist, pink is granite, blue is pegmatite, black lines are fractures, and black hatches are fracture faces. Area mapped is a roadcut along I-93 about 1 km east of the well field. Height of roadcut shown is approximately 6 m; into the page is due east. 16

Figure 4. Histograms of fracture aperture (left) and length (right). From Barton et al. (1997).... 16

Figure 5. Core samples. Complete sample from FSE 5 (left) and fractured section of core sample (above) 17

Figure 6. Top: Log log plot of observed drawdown vs time for a constant rate pumping test with FSE 6 as the pumping well. Bottom: Log log plot of modeled (lines) and observed (symbols) drawdown vs time. Figures 2 and 5a, respectively, from Tiedeman and Hsieh, 2001. 20

Figure 7. Well layout showing the westernmost FSE wells and the barn (see Figure 1 for location). 22

Figure 8. Conceptual model showing packer placement, zones A and B, and pumping location (blue circles). Depth scale is approximate; exact packer depths given in Table 3. 23

Figure 9. Schematic cross section of experiment setup. 25

Figure 10. Picture of storage tank, flowmeters, tubing to pumps, and FSE 6. 27

Figure 11. Plot of head response at observation points and formation injection – 64 min period 39

Figure 12. Plot of head response at observation points and formation injection – 32 min period 40

Figure 13. Plot of head response at observation points and formation injection – 16 min period 40

Figure 14. Plot of head response at observation points and formation injection – 8 min period . 41

Figure 15. Plot of head response at observation points and formation injection – 4 min period . 41

Figure 16. Plot of head response at observation points and formation injection – 2 min period . 42

Figure 17. FFT amplitude for FSE09a, 64-minute period. The “m” after FSE09a refers to meters, as the original pressure data were in feet of head. 44

Figure 18. FFT amplitude for FSE12b, 64-minute period 45

Figure 19. FFT amplitude for FSE12b, 8-minute period. Shown as an example that narrowly passes the criteria because the dominant frequency is just above the transducer resolution........ 50

Figure 20. FFT amplitude for FSE10a, 2-minute period. Pumping frequency is not dominant and is below the transducer resolution.. 51

Figure 21. FFT amplitude for FSE11a, 2-minute period. Although the pumping frequency is dominant, it is below the transducer resolution. 52

Figure 22. FFT amplitude for FSE12a, 2-minute period. Pumping frequency is not dominant and is below the transducer resolution.. 52

Figure 23. FFT amplitude for FSE12a, 4-minute period. Although the pumping frequency is dominant, it is below the transducer resolution. 53

Figure 24. Time and frequency domain response for FSE12b, 4-minute period. Unfiltered time series data included to show steps of ~1 mm, the transducer resolution. 53

Figure 25. Time and frequency domain response for FSE12b, 2-minute period. Unfiltered time series data included to show steps of ~1 mm, the transducer resolution. 54

Figure 26. FFT amplitude for FSE14, 4-minute period. Pumping frequency is not dominant..... 54

Figure 27. FFT amplitude for FSE14, 2-minute period. Pumping frequency is not dominant..... 55

Figure 28. Normalized amplitude vs distance from pumping well. 64-minute period (top left) through 2-minute period (bottom right).. 56

Figure 29. Observation amplitudes normalized by formation injection rate amplitude, plotted against period length. Both axes are logarithmic.. 57

Figure 30. Observation amplitudes normalized by total volume injected, plotted against period length. Both axes are logarithmic. 58

Figure 31. Phase lags vs distance from pumping well. 64-minute period (top left) through 2-minute period (bottom right). Larger values represent greater lag time. 60

Figure 32. Observation phase lags as a function of period. 61

Figure 33. Semi-log characteristic curves, after Ahn and Horne (2011). Phase shift is observation phase minus injection phase and corrected for phase wrap, and attenuation is observation amplitude divided by injection amplitude (table 9 and table 6, respectively). Non-qualifying responses (orange cells in tables) are not included. 61

Figure 34. Semi-log 3D plot of objective function for a range of diffusivity (D) and storativity (S) values. From FSE 9, 32-minute test. Total error is normalized phase error plus normalized amplitude error. 63

Figure 35. Same as figure above, except z-axis is logarithmic to show global minimum 64

Figure 36. Same as above, except larger range of D and S 65

Figure 37. Diffusivity plotted as a function of pumping period. Both axes are logarithmic. 68

Figure 38. Storativity plotted as a function of period. Both axes are logarithmic. 68

Figure 39. Transmissivity plotted as a function of period. Both axes are logarithmic. 69

Figure 40. FSE13a, 2-minute period response. Top is head in the time domain after linear detrending, middle is time domain of filtered head after high pass filter, bottom is filtered head amplitude in frequency domain. 72

Figure 41. Diffusivity versus period for each response and power function trendline of best fit. Second-to-last row, right is the mean of all observation diffusivities for each period. Using geometric mean resulted in robust power law relationship (bottom left). 75

Figure 42. Mean of all responses at each period length. 77

Figure 43. Geometric mean of all responses at each period length. 77

Figure 44. Aperture change for FSE10 (nanometers) from DAS measurements. For these experiments, injection was a square wave (not sinusoidal) and period lengths were shorter (2, 4, 8, 12, 18 minutes). From Becker et al. (2017) 80

Figure 45. Revised conceptual model with well connection based on diffusivity estimates. Colors represent relative degree of connection with green being the strongest connection, followed by yellow, orange, and red. Dots above packers are A zone, below packers are B zone. FSE14 not shown because it did not have a packer installed. Revised after Tiedeman and Hsieh (2001). 83

Figure 46. Diagram of control setup 86

Figure 47. Wiring for datalogger and voltage control module 87

Figure 48. Datalogger to voltage module wiring (from Campbell Scientific SDM-CV04 manual) 88

Figure 49. Screenshot from PC 400 software homescreen 88

Figure 50. Beneath cover of VFD: J-level pins and correct wiring 89

CHAPTER 1

INTRODUCTION

Motivation

The impetus for this work is the need for improved understanding of fluid flow in enhanced geothermal systems (EGS). Geothermal energy represents a vast, largely untapped source of carbon-free energy that does not fluctuate temporally like solar and wind. Its reserves are plentiful, especially in the western US, though natural hydrothermal locations where the energy can be readily extracted are limited. An EGS increases permeability within hot rock to permit fluid circulation for heat extraction.

The quality of the engineered circulation system is often the limiting factor in geothermal energy production. The system must have sufficiently high permeability so that water can be extracted at quantities to support large-scale production. Flow paths must also be diffuse so that water interacts with as much rock as possible. A common phenomenon in these settings is highly “channelized” flow, in which most fluid movement occurs in a few preferred pathways, thus reducing surface area available for thermal exchange. Channelized flow leads to a premature reduction in extracted water temperature. This behavior is referred to as early thermal breakthrough. Characterization that can predict channelized flow and determine hydraulic connection is critical at both development and operation stages of EGS.

Background

Groundwater investigations in homogeneous sediments are relatively straightforward. Estimates of aquifer parameters are obtained by pumping or injecting water and observing the head changes at distant locations. These estimated properties are then used in models or calculations to predict groundwater flow or aquifer storage. Subsurface heterogeneity complicates this process because the estimated parameters typically do not describe the spatial variation; instead they represent the spatially averaged properties. Some of the most heterogeneous hydrogeologic systems are fractured bedrock formations.

Characterizing water flow in fractured rock remains challenging despite decades of research (National Academies of Sciences - Engineering - Medicine, 2015). Water flow and storage is dominated by fractures or fracture zones, the spatial distribution of which are random and difficult to predict (Golder Associates, 2010). Even within a single fracture plane, differences in aperture and wall roughness cause flow to be highly channelized (Tsang and Neretnieks, 1998). While fractures and fracture zones can be located down-well using geophysical testing or drilling log analysis, determining which of them readily transmit water is much more challenging. Predicting the interconnectedness of these fractures between wells presents an even greater challenge and is the focus of this thesis.

This thesis builds on recent research suggesting that periodic hydraulic testing may improve understanding of flow in heterogeneous media, including fractured rock. The theory behind this type of testing has been examined in both the groundwater and petroleum literature, but the number of field-scale tests are limited. In recent years, periodic tests have been performed in confined and unconfined sedimentary aquifers (Rasmussen et al., 2003; Rabinovich et al., 2015), and in discrete fractures and fracture networks (Renner and Messar, 2006; Becker and Guiltinan, 2010; Sayler et al., 2017).

The significant advantage of periodic testing is that the scale being investigated (i.e. radius of influence) can be tuned based on the region in question. Tests performed at multiple frequencies yield more information than a single frequency or constant rate test, and can lead to better understanding of fracture flow. Presented here are periodic tests performed in a bedrock fracture network at Mirror Lake fractured rock research site in New Hampshire. The primary goal is to characterize this heterogeneous network using multi-frequency periodic pumping tests. Controlling the radius of influence and testing at a range of frequencies should elucidate inter-well hydraulic connections better than the constant rate test. A second goal is to analyze the variation in hydraulic properties with frequency. These trends will then be discussed in relation to the periodic hydraulic testing literature, and a mechanism for the observed trends will be evaluated. These two goals will lead to a site-specific characterization for this bedrock fracture network and add to the growing body of work using this type of test.

CHAPTER 2

PREVIOUS WORK

Current Standard Methods

The standard investigative tool in the fields of petroleum, geothermal, and hydrogeology is the hydraulic interference test. In a hydraulic interference test, hydraulic head is perturbed in a source well, usually through pumping or slug insertion, while heads at observation wells are recorded. The resulting head response is then fit to an analytic solution from which hydraulic parameters (e.g. conductivity and storativity) can be inverted.

Pressure (hydraulic head) propagating through a formation is a diffusion process, which is mathematically analogous to heat and electrical flow. The rate of diffusion is governed by the ratio of the medium's transport property to its storage property, which for groundwater flow are transmissivity (T) and storativity (S), respectively. The ratio of transmissivity to storativity (T/S) is called hydraulic diffusivity (D). The radius of investigation of a hydraulic interference test is proportional to $\sqrt{T_c D}$, where T_c is a characteristic pumping time. The radius of investigation can be used to obtain an estimate of the volume of the formation tested for a given pumping test duration. Storativity is a measurement of the change in water stored or released due to a unit change in head, and is mostly influenced by effective porosity. In fractured rock, where effective porosity is very small, storativity values are often several orders-of-magnitude lower than those for porous media. Therefore, diffusivity is several orders of magnitude greater, and the radius of investigation becomes very large even at short pumping times.

Traditional pumping tests in fractured rock have been noted for estimating properties of large volumes of the formation, but missing local heterogeneity (Becker and Guiltinan, 2010). Because the radius of investigation expands so rapidly, only the earliest time data represent near-well properties, and these data are typically obscured by pumping noise. The large-scale estimates are often insufficient because specific fracture flow paths are needed for many applications. Tracer tests are the industry standard method of establishing hydraulic connections among wells, but these are expensive and time consuming. Recent research indicates that hydraulic diffusivity is a good indicator of well connection, as predicted by tracers (Knudby and Carrera, 2006). Hydraulic testing that provides accurate estimates of diffusivity at a useful radius of investigation can therefore serve as an efficient method of predicting connection between wells in fractured rock.

Periodic Hydraulic Tests

A periodic hydraulic test displaces water in a source well periodically. The periodic displacement creates a diffusive hydraulic wave through the formation, which is detected at observation wells. Periodic testing offers logistical advantages, more robust data analysis, and, as recent research suggests, more insight into formation heterogeneity. This type of hydraulic test was first used in the oil industry during the 1970s and throughout the decades has remained useful for measuring skin effects and near-well properties (Hollaender et al., 2002).

An inherent logistical advantage of periodic compared to conventional tests is the option of zero net extraction or net withdrawal. When dealing with contaminated groundwater, water injection and extraction can be alternated so that no net water is removed from the formation, which avoids the problem of contaminated water disposal. Contaminant migration is reduced due to smaller imposed head gradients and less disruption of natural flow directions (Cardiff et al., 2013). Alternatively, periodic rates can be imposed over net withdrawal so that wells may be left in production during testing.

Signal processing is an effective tool for interpreting periodic tests. Renner and Messar (2006), for example, carried out periodic tests in a jointed sandstone formation and used a fast Fourier transform (FFT) to process the flow and pressure data, providing estimates of transmissivity and storativity. Many authors have noted the advantage of having an input signal of known frequency that can be more easily detected against background drift and noise using signal filtering (Cardiff et al., 2013). One commonly encountered problem with conventional pumping tests is the difficulty in distinguishing response to pumping from other factors, such as pumping from a nearby supply well or barometric effects. Cardiff et al. (2013) and others have pointed out the potential to use large-scale periodic inputs (i.e. tides and seasonal recharge) for basin-scale reservoir characterization, a scale not realistically attainable by pumping tests. Rotzoll et al. (2013) used tidal signal attenuation in monitoring wells and a simple analytical model to estimate diffusivities of an approximately 100 km^2 karst aquifer on the island of Guam, USA.

An important characteristic of periodic testing is that the distance of interrogation (i.e. radius of influence) can be varied. This allows hydraulic parameters to be evaluated with respect to a variable distance from the oscillating well. It may also elucidate network connections in the fracture network. Guiltinan and Becker (2015) performed sinusoidal slug tests in a single bedding plane fracture at a scale of several meters. Their diffusivity estimates for different well pairs predicted variations in inter-well connectivity that were not identified through a constant rate pumping test.

Cardiff et al. (2013) created numerical models of periodic pumping tests and produced synthetic maps that showed the spatial sensitivity of parameters (transmissivity and storativity). They noted that changing the frequency of pumping changed these sensitivity structures. Higher frequencies were more sensitive to near-well features and were tightly focused between pumping and observation wells. Lower frequencies produced more diffuse sensitivity maps that gave information about larger scale features. The authors suggested that spatial heterogeneity can be observed by varying pumping frequencies. In their synthetic tests, estimates of hydraulic conductivity became closer to the true values as more test frequencies were included in the inversion (Cardiff et al., 2013).

Periodic testing has been discussed in the petroleum literature for investigating heterogeneous permeability. Rosa and Horne (1997) presented an analytic solution for periodic flow rate variations in a radial model with concentric rings of varying permeability about the pumping well. They compared constant flow rate tests (drawdown) to cyclic pulse tests in this heterogeneous radial model, and found that the pulse tests gave estimates closer to the defined permeability values for each ring. They concluded that the pressure response in heterogeneous reservoirs is “sensitive to the permeabilities of different regions, in a manner that is frequency-dependent”. Rosa and Horne also determined that the optimum testing frequency is that which gives a radius of influence 70-80% of the inner radius of the outermost model ring.

Interestingly, Rosa and Horne (1997) found that pressure response at the pumping well is significantly influenced by properties of the region defined by the radius of influence, but pressure response at an observation well is sensitive to properties of regions beyond that. Permeability estimates obtained by performing the analysis at the pumping well gave less error compared to the defined parameters than when the analysis was performed at an observation well, except for their two outermost zones, for which errors were similar. Examination of their analytical solution corroborated this result.

Building on Rosa and Horne's work, Ahn and Horne (2011) investigated the use of periodic tests at multiple frequencies to reveal heterogeneity. Using frequency domain analysis, they compared numerical results from multiple sinusoid inputs to those from a square wave input, which can be broken down to the dominant frequency plus harmonics. They compared a homogeneous case to cases of heterogeneous permeability and storage [porosity]. Again, they found that testing over a range of frequencies provides the key to heterogeneous reservoir characterization. For each testing frequency, they plotted the measured attenuation against phase shift, forming "characteristic" curves. These curves were then compared for various spatial permeability distributions. Changing the structure of heterogeneity resulted in different characteristic curves; changing only the magnitude of parameters resulted in invariant characteristic curves. They reasoned that these different curves imply a qualitative representation of heterogeneity.

The lack of an analytic solution that includes well-bore storage in periodic hydraulic tests is problematic because well-bore storage can affect attenuation and phase lag of the periodic pressure response measured in an observation well bore. Recognizing this, Ogbe and Brigham (1987) include well-bore storage and skin effects in their semi-analytic solution for pulse tests. They present their solution as a series of correction factors for determining the true amplitude and phase lag based upon well bore dimensions.

Period Dependence of Estimated Hydraulic Parameters

The frequency dependence of modeled properties discussed above has also been observed in field studies. Estimates of diffusivity (*D*) from previous periodic pumping tests in bedrock formations have mostly displayed a decreasing trend in *D* with increasing period (Becker and Guiltinan, 2010; Renner and Messar, 2006). A variety of explanations have been proposed for this phenomenon. **Table 1** summarizes the trends of hydraulic parameters with period length reported just for periodic tests in fractured rock.

Table 1. Summary Table of Results from Field Studies Utilizing Periodic Hydraulic Tests in Fractured Bedrock Formations

Study **Site description and area**	**D**	**T**	**S**	**Other notes**
	With increasing period length			
Guiltinan and Becker, 2010 Altona, NY; single fracture (~10 x 10 m)	Decreased	Decreased	Increased	- Estimates more sensitive to local heterogeneity than constant rate test - *S* more variable among wells than *T*
Becker et al. 2015 (Oral presentation) Ploemeur, France; fracture network (~10 x 10 m)	Decreased	No consistent trend	Increased	- Diffusivity exhibits power-law trend with period length
Renner and Messar, 2006 Kemnader See, Germany; Fracture network (~60 x 30m)	Decreased (interference test)	NA	NA	- Estimates are averaged over the vicinity of the area between pumping and monitoring well
Sayler et al., 2017 Wisconsin; 2 discrete fracture intervals (~10 x 10m)	Mostly decreased*	NA	NA	- *"Highway A" lower interval did not exhibit a strong decrease in *D* with period. For 2D geometry assumption, *D* increased with period
Current study Mirror Lake, NH; fracture network (~60 x 60m)	Decreased	Decreased	Decreased	- *S* more variable among wells, *T* more variable among period lengths
D = diffusivity, T = transmissivity, S = storativity, NA = not reported/applicable				

Renner and Messar (2006) suggested that the decrease in *D* was a result of the greater time available for pressure to equalize between main pathways of flow and dead-end pores. The interplay between main flow pathways (flow backbone) and dead-end pore spaces resulted in a larger apparent storativity as period increases. It appeared to have little effect on apparent transmissivity. Although Becker and Guiltinan (2015) observed both an increase in *S* and a decrease in *T* with period, they inferred that *S* was the driver in this relationship because the relative change in *S* was greater than *T*. Cardiff et al. (2013) argued that what was seen in both field studies may have been simply a manifestation of the particular heterogeneity of T and S at each site.

Rabinovich et al. (2013a,b) looked at dynamic (complex) effective properties of a matrix with spherical inclusions under periodic boundary conditions (i.e. periodic head at the inlet). In the first paper (a), they used a semi-analytical model to compute effective conductivity and capacity (storativity) for a range of inclusion to matrix ratios of K and S. These dynamic effective properties were very close to the steady state approximation for most of these ratios, except when $K_{inclusion}/K_{matrix}$ became small and $S_{inclusion}/S_{matrix}$ became large at a small dimensionless period. Therefore, they imply that heterogeneity should have a greater impact on effective storage than effective conductivity. With decreasing period, S may increase or decrease depending on the difference in storage properties between heterogeneities and the matrix (Rabinovich et al., 2013a). The second paper (b) compared steady state conductivities with effective conductivities as a function of conductivity variance and pumping frequency. Their findings show that dynamic effective conductivity departs from the steady state solution as both frequency and variance (representing heterogeneity) increase (Rabinovich et al., 2013b).

Rabinovich et al., (2015) performed periodic tests in an unconfined aquifer and found that effective conductivity increased as period decreased and that the effective parameters showed little variation at large periods. To explain the mechanism for this they ran a simple model with a single, spherical inclusion with a hydraulic conductivity (K) different than the surrounding matrix. To satisfy the condition that equivalent K increases for shorter periods, K of the inclusion must be smaller than K of the matrix. When decreasing the period, the increase in gradient in the matrix is larger than in the inclusion. This implies that the increase in K with decreasing period is related to both the low conductivity heterogeneities and the resulting change in gradients. Their plot of head gradient versus period showed that for long periods the gradients inside and outside the sphere were equal, but as period decreased the gradient inside relative to outside the sphere decreased. They cite this tendency for flow to favor the more conductive media as the reason for increasing effective K with decreasing period (Rabinovich et al., 2015). These models with spherical inclusions bear little resemblance to fractured rock settings, but the described flow tendency will be useful for comparing to preferential pathways in fractured rock.

CHAPTER 3

SITE DESCRIPTION

Overview

The Mirror Lake Fractured Rock Research Site lies within Hubbard Brook Experimental Forest (HBEF) in the White Mountains of New Hampshire. The research area is a small (~1 km^2) drainage basin near the eastern boundary of the Hubbard Brook watershed that contains several dozen wells including the 100 m^2 Forest Service East (FSE) well field (**Figure 1**), where we performed the experiments. The subsurface at this location is comprised of 15-20 meters of glacial deposits (till, sand, and cobbles) underlain by crystalline bedrock (Tiedeman and Hsieh, 2001).

The wide breadth of documentation and numerous previous investigations at this site led to its selection for these experiments. This information provided the basis for experimental setup and hydraulic parameters to compare to these estimates. The site has been extensively studied over the past few decades and has been characterized using methods including geophysical testing, open borehole and packed off hydraulic tests, and tracer tests (USGS, 2016). As is typical in fractured crystalline rock, these studies confirm that the bedrock hydraulic properties are highly heterogeneous, with conductivity varying at least six orders of magnitude between fractures and intact rock (Johnson and Dunstan, 1998).

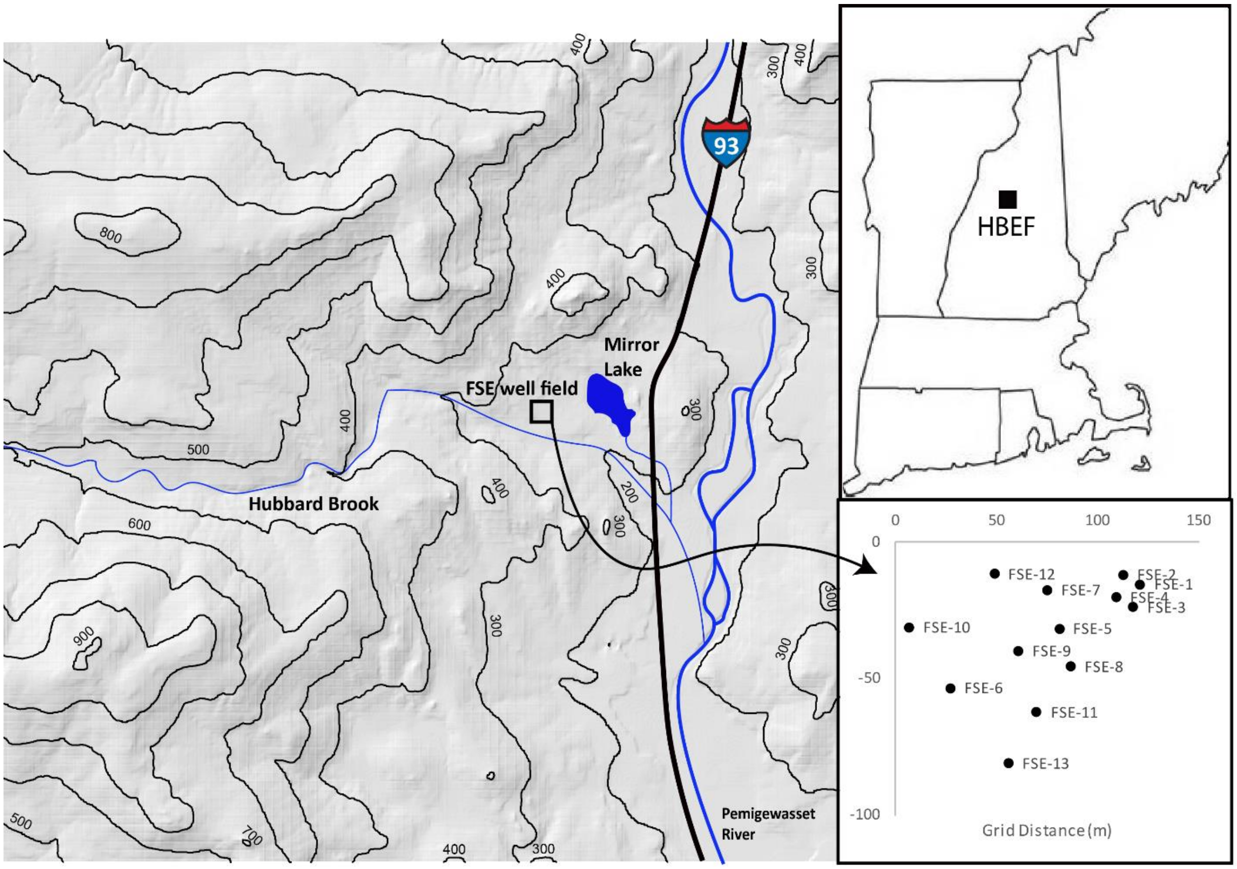

Figure 1. Map of northeastern states showing HBEF (top right), topographic map of Mirror Lake basin (left), and grid showing layout of FSE well field (bottom right)

Geology

Geologic mapping of the area and drilling cores from well construction indicate that the bedrock is a pelitic schist with extensive igneous intrusions. The schist is interpretted to be part of the Silurian Rangeley Formation, a medium to coarse grained, thinly laminated, black and white pelictic schist that was metamorphosed during the Acadian and possibly Alleghenian orogenies of the Middle and Late Paleozoic (Johnson and Dunstan, 1998). Intrusions are mostly Concord Granite, a gray, two-mica granite that is part of the regional Concord Intrusive Suite emplaced during the Acadian orogeny, though some diabase dikes from a later event (Cretaceous or Jurassic) are present as well (Barton et al., 1997). Intrusions occur as fingers and dikes that cut both across and along foliation planes (Johnson et al., 1996).

To summarize the geologic history, clay-rich sediments were eroded and filled a basin during the Silurian period to form the Rangeley. As the Acadian orogeny began around the start of the Devonian period, the Rangeley and other units underwent deformation and sillimanite-grade metamorphism, and later, granite fingers and dikes intruded. During the Pennsylvanian, the Alleghenian orogeny likely caused further deformation. Finally, diabase dikes cut across all units during the Middle to Late Mesozoic. The result is a highly deformed and fractured bedrock with a complex distrubution of lithologies.

Most of Canada and the Northeastern US was covered by the massive Laurentide Ice Sheet during the Wisconsinan glacial period at the end of the Pleistocene (**Figure 2**). As is typical of areas covered by glaciers, ice scoured the ground surface in the Mirror Lake basin and

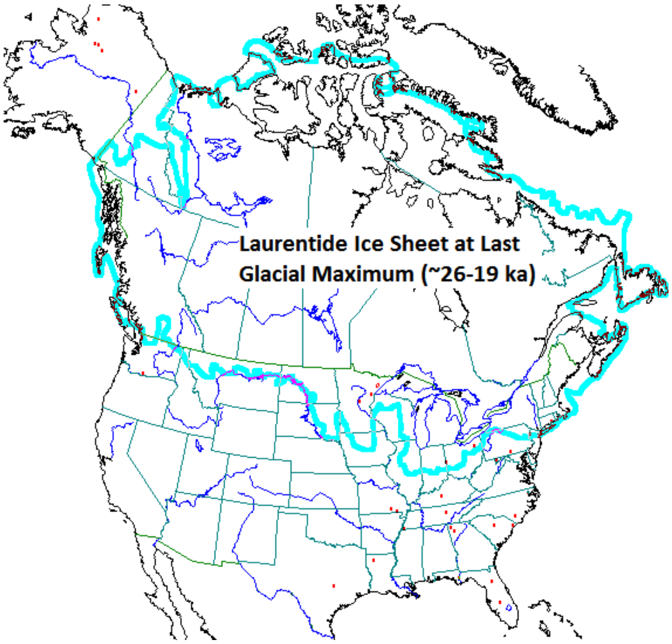

Figure 2. Map of North America and last maximum extent of Laurentide Ice Sheet. Modified from Berger (2013).

stripped away any soils, unconsolidated deposits, and weathered bedrock. After the ice sheet's maximum extent approximately 13,000 years ago, glaciers retreated from the White Mountains leaving till (diamicton) deposits in the Mirror Lake basin (Bromley et al., 2015). The till varies in thickness and composition across the basin from silt and sand to coarse sand and gravel, but near the FSE well field it is predominantly unstratified silty sand with some cobbles and boulders, and is about 15 m thick (Winter, 1984; Johnson and Dunstan, 1998).

Fractures

The fractured bedrock of HBEF has been of interest ever since early hydrologic studes of the watershed accidentally discovered its significance, when assumptions of an impermeable bedrock led to unbalanced water budgets. Because the matrix permeability is much lower than the fractures, essentially all groundwater flow in the bedrock occurs through fractures. Efforts have been made to understand the distribution of these fractures in the Mirror Lake area. For example, Barton et al. (1997) mapped fractures in a roadcut exposed at the nearby interstate highway. A small segment of one roadcut from this map is shown in **Figure 3** to illustrate the orientation of fractures (Barton et al., 1997). Quantitative analysis of these mapped fractures shows variable orientation with preferred strike of 030 degrees and dips ranging from shallowly NW to steeply SE. Aperture ranges from .005 mm to 20 mm and trace length from 1 m to 25 m. Data fit a negative power law relationship for both properties and there was litte correlation between them, meaning the greatest frequency of fractures are short and tight (**Figure 4**).

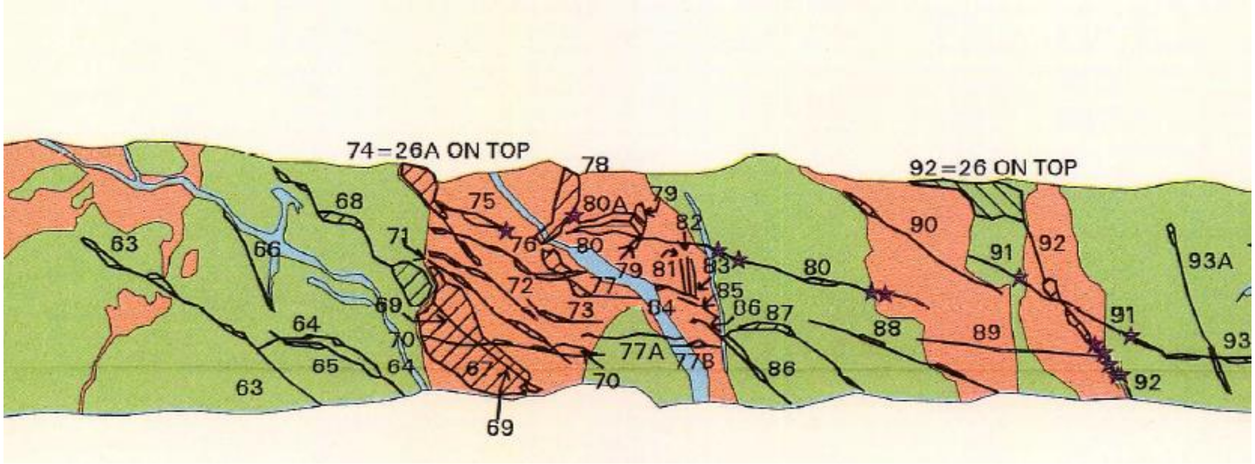

Figure 3. Segment of roadcut map created by Barton et al. (1997). Green is schist, pink is granite, blue is pegmatite, black lines are fractures, and black hatches are fracture faces. Area mapped is a roadcut along I-93 about 1 km east of the well field. Height of roadcut shown is approximately 6 m; into the page is due east.

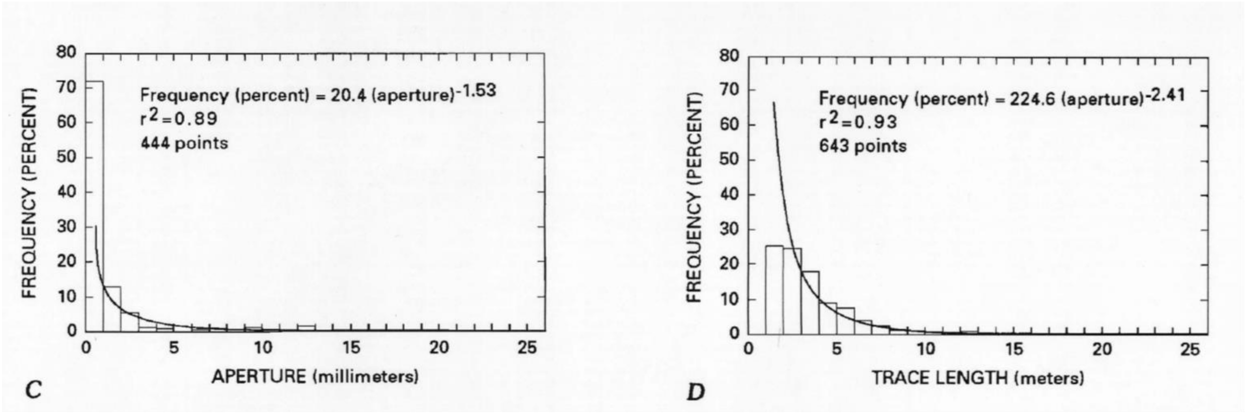

Figure 4. Histograms of fracture aperture (left) and length (right). From Barton et al. (1997)

Fractures were also described using data obtained during the drilling of bedrock boreholes, including images from a submersible camera and well driller's yield (Johnson and Dunstan, 1998). A total of 40 bedrock boreholes were drilled near Mirror Lake, including the 13 FSE wells, and complete core samples were saved for three wells (**Figure 5**). The main conclusions about the fractures from drilling are as follows: the average fracture frequency is 0.47 fractures per meter, with frequency generally decreasing past a depth of about 100 meters; the granitoids are more fractured than the metamorphic rocks, with 73% of fractures in granite, 23% in schist, and the remaining few percent in gneiss, diabase, pegmatite, and quartzite; fractures do not typically occur along lithologic contacts or continue from one lithology to another (Johnson and Dunstan, 1998). Drilling logs for each well in this report, including depths to fractures, provide the basis of experimental design for this study.

Figure 5. Core samples. Complete sample from FSE 5 (left) and fractured section of core sample (above)

Hydrologic Setting

The hydrology of HBEF has been documented through hydrological and ecological research. The humid continental climate is characterized by mild summers and long, cold winters. Precipitation averages around 1400 mm/year distributed evenly over each month. Stream flow rates are highest in March through May, when spring snowmelt occurs, and lowest in the summers when evapotranspiration is highest; groundwater recharge follows this seasonality as well. The perennial Hubbard Brook crosses just south of the Mirror Lake basin, while ephemeral streams and groundwater recharge the lake. Groundwater flow in the glacial deposits is influenced by topography and the distribution of varying types of till, and is closely connected to surface water. Average hydraulic conductivities in the glacial till are between 1E-6 and 2E-7 m/s, but can be two orders of magnitude higher in patches of sand and gravel. Hydraulic conductivity in the bedrock is more variable, ranging from 5E-5 to 1E-10 m/s with the greatest conductivity in zones of interconnected fractures (Tiedeman et al., 1997).

Tiedeman and Hsieh (2001) modeled groundwater flow in the bedrock within the FSE well field and incorporated this zonality. They created a 2D and 3D numerical (MODFLOW) model and compared the results to reference parameters given by well tests in which zones had been isolated by packers. While the 2D model accounted only for lateral heterogeneity, the 3D model could account for heterogeneity in the vertical direction with thin, high conductivity layers representing the fracture zones within the low conductivity bedrock. Results of the numerical models showed that transmissivity estimates were similar to reference transmissivities for both the 2D and 3D cases, but storativity estimates were significantly different for the 2D case while the 3D case was close to reference storativity. This led them to conclude that the differences in storativity were due to misrepresentation of heterogeneity, which was better represented in the 3D model.

Drawdown versus time plots illustrate hydraulic connections in the well field. **Figure 6** displays drawdowns both measured from a constant rate pumping test and predicted from the 3D model. The late time drawdowns approach a constant value, suggesting that heads in the bedrock are being recharged from the overlying glacial sediments. Additionally, drawdowns from FSE8, 9, 11, and 13 converge, suggesting that they are connected by one or more permeable fracture zones (Tiedeman and Hsieh, 2001). It is worth noting that FSE11 is the first to respond to pumping in FSE6 (**Figure 6**, top).

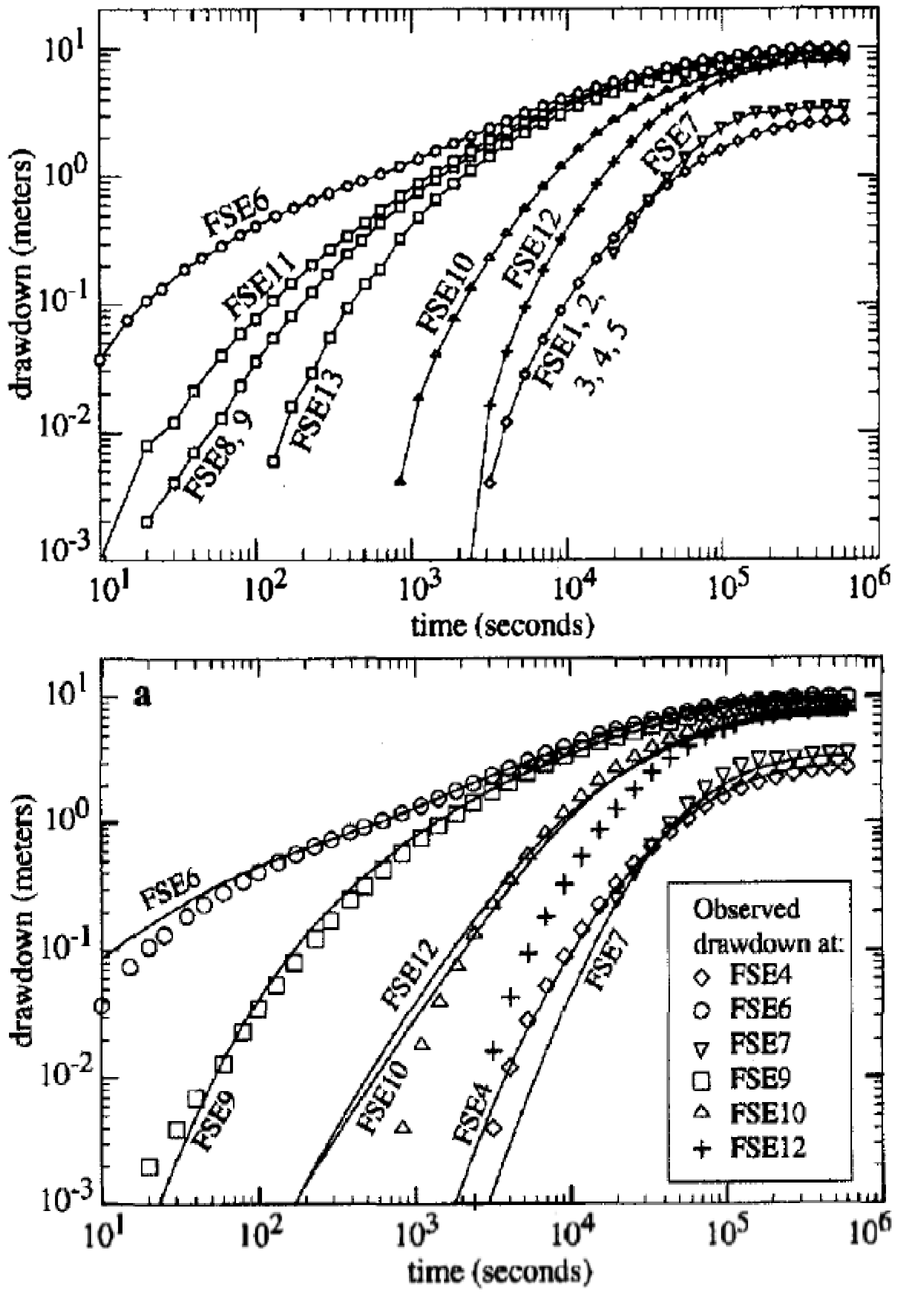

Figure 6. ***Top:*** **Log log plot of observed drawdown vs time for a constant rate pumping test with FSE 6 as the pumping well.** ***Bottom:*** **Log log plot of modeled (lines) and observed (symbols) drawdown vs time. Figures 2 and 5a, respectively, from Tiedeman and Hsieh, 2001.**

CHAPTER 4

METHODS

Experiment Setup

The hydraulic experiments took place during July 2015 in the westernmost Forest Service East (FSE) wells (FSE6, 9, 10, 11, 12, and 13; **Figure 7**, **Figure 8**). Wells in the FSE field are developed with 15.2 cm diameter steel casing that penetrates the glacial deposits and about 3 m into the bedrock. Below this depth the wells are open boreholes approximately 15 cm in diameter and 75-85 m deep, though three wells are 108 m deep and one is 229 m deep (Tiedeman and Hsieh, 2001). According to drilling logs and previous investigations, wells on this side of the well field generally intersect two major transmissive fracture zones: an upper zone “A” and a lower zone “B”. Because the open boreholes provide unnatural vertical conduits between mostly disconnected horizontal fracture zones, inflatable packers were installed between zones A and B in each well (**Figure 8**, **Figure 9**). **Table 2** displays information from drilling logs and previous investigations, which was used to determine packer placement depths.

Table 2. Characteristics of Fractures Significant to Flow

	Driller’s yield from borehole (L/min)*	Depth to most transmissive upper fracture **	Approximate fracture aperture*	Other descriptors from drilling*
FSE 6	30.28	32.88	Wide (>1 cm)	Water bearing during drilling, alteration, borehole enlargement
FSE 9	22.71	42.82	Moderate (0.5-1 cm)	Water bearing during drilling, oxidation, borehole enlargement
FSE 10	3.78	28.33	Narrow (<0.5 cm)	Water bearing during drilling
FSE 11	22.71	45.59	Moderate	Multiple fractures (3)
FSE 12	2.84	56.71	Narrow	Alteration
FSE 13	22.71	37.61	Narrow	Abutting fractures

*** From Mirror Lake Drilling Logs (Johnson and Dunstan, 1998)**
**** From Tiedeman et al., 1997**

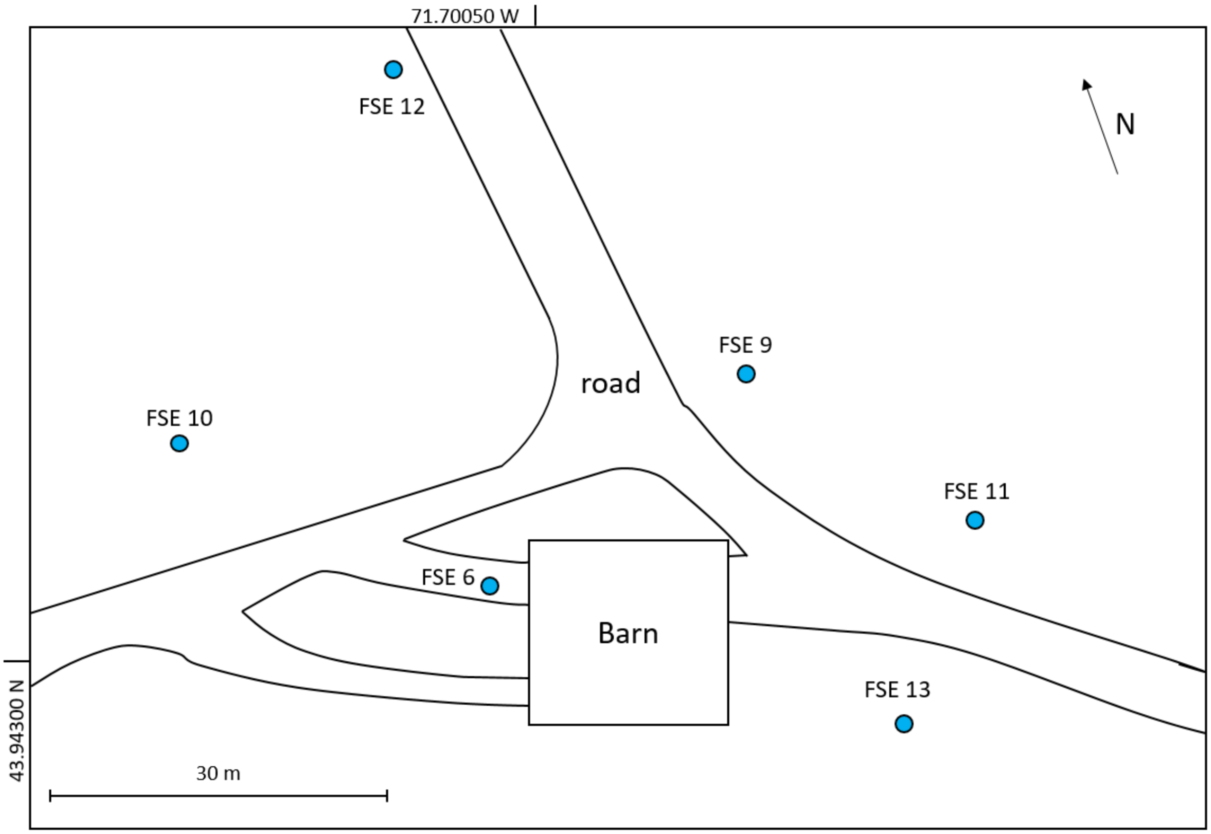

Figure 7. Well layout showing the westernmost FSE wells and the barn (see Figure 1 for location).

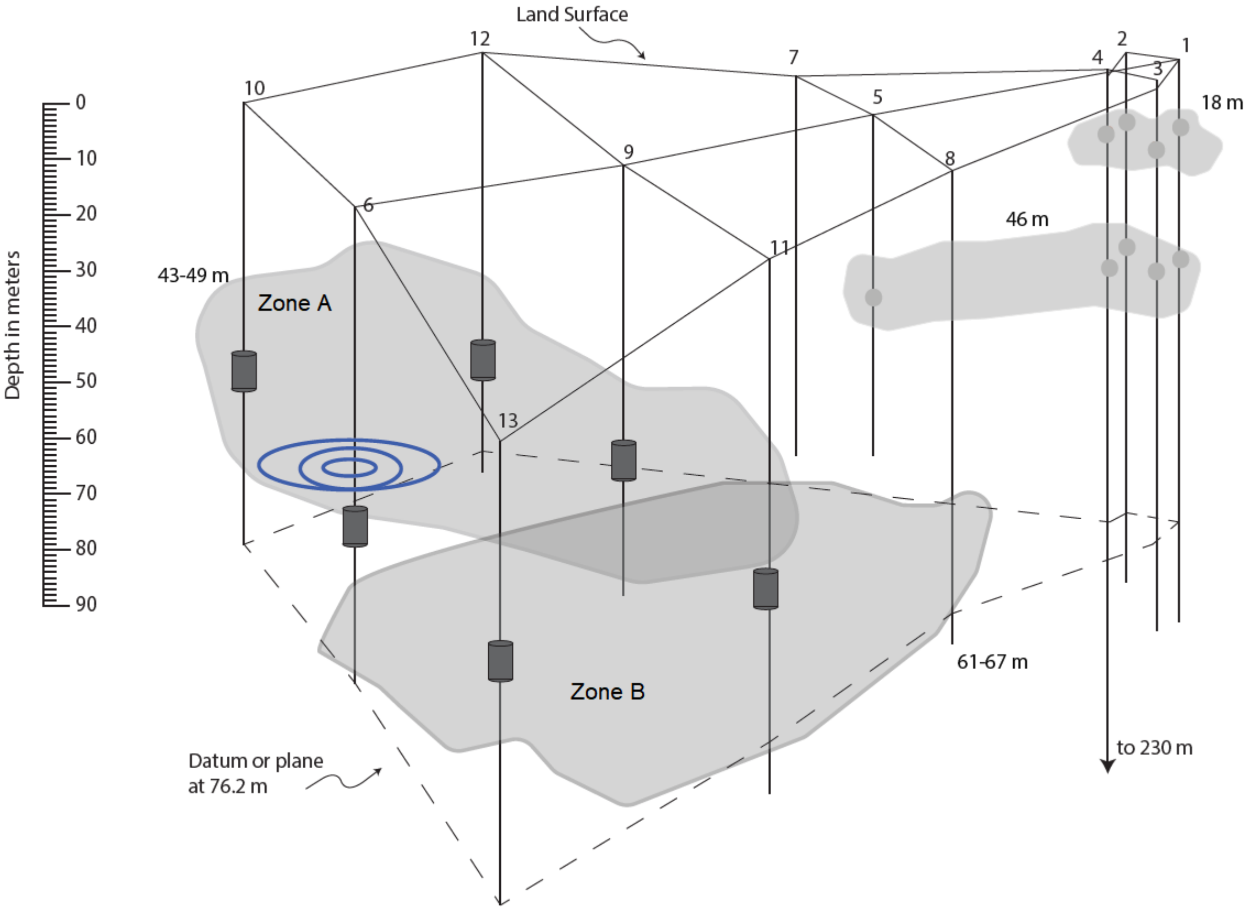

Figure 8. Conceptual model showing packer placement, zones A and B, and pumping location (blue circles). Depth scale is approximate; exact packer depths given in Table 3.

Packers for this experiment (manufactured by Lansas Products, Lodi, CA) were made of a rubber cylinder surrounding an aluminum through-pipe. They were lowered to the desired depth in the well, then inflated to create a water-tight seal against the borehole. ¼ inch nylon tubing ran from the packer's inflation valve to the top of the well. Correct inflation pressure, equal to the recommended pressure of 50 PSI plus hydrostatic pressure at the installed depth, was verified several times a day, ensuring a good seal throughout the experiments. One packer burst soon after installation, likely due to a puncture from a sharp edge in the borehole, and was replaced before running experiments. Each packer was lowered on either rope or PVC pipe, depending on available equipment. Those lowered on PVC pipe enabled pressure monitoring both above and below the packer. **Table 3** shows the equipment used for each well and packer installation depths. All wells on the west side of the well field were used for either monitoring or pumping. FSE 14 is a newer well and its presence was unknown, so no packer was available to install in it.

Pressure transducers were deployed in every well to monitor head in both zones, if possible. Head could be monitored in real time with transducers, while Levelogger data had to be downloaded after retrieval. The type of device used in each well and interval is also listed in **Table 3**. CS transducers are Campbell Scientific® CS-450 (0-10.2 m range, 0.3 mm resolution), KWK transducer is KWK Technologies SPXD-600 (0-35 m range, 1.5 mm resolution), and Leveloggers are Solinst® Levelogger® Model 3001 (0-10 m range, 1 mm resolution).

Table 3. Well Equipment Summary

Well	Well type	Packer on	Packer depth [ft (m)]	Upper Zone A	Lower Zone B
FSE 6	pumping	rope	123.3 (37.6)	KWK transducer	-
FSE 9	monitoring	rope	145 (44.2)	CS transducer	-
FSE 10	monitoring	rope	100 (30.5)	Levelogger	-
FSE 11	monitoring	PVC	160 (48.8)	CS transducer	Levelogger
FSE 12	monitoring	PVC	190 (57.9)	CS transducer	Levelogger
FSE 13	monitoring	PVC	130 (39.6)	CS transducer	Levelogger
FSE 14	monitoring	-	-	Levelogger	

The pumping well for all experiments was FSE 6, located closest to the barn. Periodic pumping was achieved using two pumps, one down well and the other in a plastic storage tank (250 gal) located near the well casing (**Figure 9**). The pumps were Grundfos® Redi-Flo 2 model MP1 (Grundfos Pumps Corporation, Downers Grove, IL) controlled by Baldor® H2 Variable Frequency Drives (VFD) (Baldor Electric Company, Fort Smith, AR) designed specifically for

Grundfos pumps. Each VFD was programmed to accelerate its pump from zero to maximum specified flow and decelerate back down to zero, approximating sinusoidal flow rates. This acceleration curve was followed for ½ period, then the pump sat sit idle for ½ period; the pumps were out of phase by ½ period so that while one was pumping the other was idle. This was accomplished using the *profile run mode* in the VFDs and adjusting the *accel*, *decel*, *max output*, and *min output* parameters. Different pumping periods were imposed by changing the profile run time length for each test. The exact parameters used for each test are described in **Table 4**.

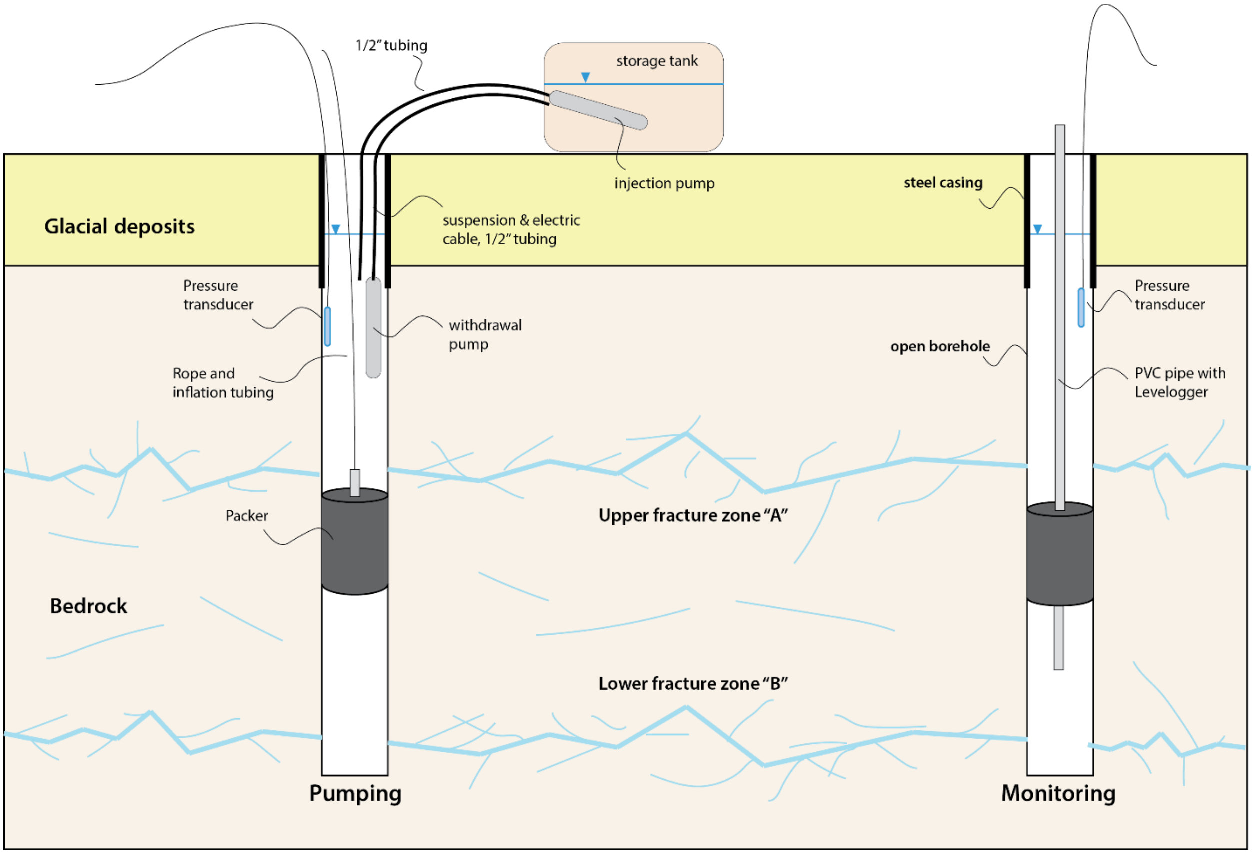

Figure 9. Schematic cross section of experiment setup.

Table 4. Setup and Parameters for VFD Controller

<table>
<tr><td colspan="6">The table below describes operation of <i>profile run</i> mode, a built-in operating mode for Baldor VFD. This automatically cycles through <i>Preset Speeds 1-7</i>, running at each of the 7 speeds for time length set in <i>Profile Time 1-7</i>, and ramping up/down to that speed according to <i>Accel/Decel</i> time.</td></tr>
<tr><td colspan="6">Initial setup notes:</td></tr>
<tr><td colspan="4"><i>Local/remote</i> button</td><td colspan="2">Toggled to <i>remote</i></td></tr>
<tr><td colspan="4"><i>Operating mode (Advanced params > level 1 block)</i></td><td colspan="2">Set to <i>Profile Run</i></td></tr>
<tr><td colspan="4"><i>Profile Run settings (Advanced params > level 3 block)</i></td><td colspan="2"><i>No. of Cycles = 16; Time</i> and <i>Speed</i> = see below</td></tr>
<tr><td colspan="4"><i>Accel & Decel (Basic params)</i></td><td colspan="2">See below</td></tr>
<tr><td colspan="4"><i>Ramp rates (Advanced params > level 1 block)</i></td><td colspan="2"><i>Start S-Accel = 0%, End S-Accel = 100%
Start S-Decel = 100%, End S-Decel = 0%</i></td></tr>
<tr><td></td><td></td><td colspan="2">Withdrawal pump</td><td colspan="2">Injection pump</td></tr>
<tr><td rowspan="2">Parameter:</td><td><i>Preset speed 1, 2, 3-7 (Hz)</i></td><td colspan="2">100, 400, 100</td><td colspan="2">30, 330, 30</td></tr>
<tr><td></td><td><i>Accel & decel (s)</i></td><td><i>Time 1, 2, 3, 4-7 (s)</i></td><td><i>Accel & decel (s)</i></td><td><i>Time 1, 2, 3, 4-7 (s)</i></td></tr>
<tr><td rowspan="6">Test length:</td><td>2 min</td><td>35</td><td>10, 0, 50, 0</td><td>35</td><td>54, 0, 6, 0</td></tr>
<tr><td>4 min</td><td>70</td><td>10, 0, 110, 0</td><td>70</td><td>no data</td></tr>
<tr><td>8 min</td><td>140</td><td>10, 0, 230, 0</td><td>140</td><td>no data</td></tr>
<tr><td>16 min</td><td>280</td><td>10, 0, 470, 0</td><td>280</td><td>48, 0, 432, 0</td></tr>
<tr><td>32 min</td><td>560</td><td>10, 0, 950, 0</td><td>560</td><td>156, 0, 804, 0</td></tr>
<tr><td>64 min</td><td>1120</td><td>Manually accel, decel, or idle every 16 min</td><td>1120</td><td>Manually accel, decel, or idle every 16 min</td></tr>
</table>

Water was pumped through ½ inch diameter nylon tubing. Check valves in each tube line prevented siphoning from the storage tank and the volume of water in tubing from falling back into the well during idle cycles for the injection and withdrawal pumps, respectively (**Figure 10**). Flow meters (Omega® Engineering, FTB4605) measured flow rates through each tube. All transducers and flow meters were wired to a Campbell Scientific® CR800 datalogger which was connected to a laptop PC. We used the Forest Service barn adjacent to the FSE well field to store equipment and set up tables and chairs.

The *profile run* programming method of pump control was used here because it was considered more reliable than other proposed methods and sufficiently accurate. Another method to achieve the desired pumping rates using the same equipment is external voltage control, in which a voltage modulator can send sinusoidal voltages to the VFD, as explained in Appendix 1. This method would also allow process control using feedback from the flowmeters to adjust VFD power output for consistent flow rates.

Figure 10. Picture of storage tank, flowmeters, tubing to pumps, and FSE 6.

Injection and withdrawal flow rates were not perfectly balanced. The VFDs modulate power sent to the pumps, but the resulting flow is affected by head loss between the pump and the outflow point as well as pump power output. The withdrawal pump was set to a greater max output than the injection pump to account for the height that water had to be lifted out of the well, but fluctuating head in the pumping well varied this gravitational energy loss. In addition, there may have been different frictional head losses between withdrawal and injection due to tubing and check valve differences.

Sinusoidal Tests

Hydraulic tests began on the afternoon of July 21st, 2015 and continued into the evening, running tests at period lengths 2, 4, 8, 16, and 32 minutes, then concluded with a 64-minute period test on July 22nd. Each test was run for approximately 8 complete periods. The five tests on July 21st were run using the profile run mode described above, but this was not functioning properly for the 64-minute test; the idle pump would not automatically cycle on after one-half period. This issue was not going to be resolved in a timely manner, so instead, injection and withdrawal pumps were manually alternated every half period. The sinusoidal flow rate was still achieved using the acceleration parameter in the VFD. The only experimental difference this made was that the 64-minute test started with the injection half-period, while all others began with the withdrawal half-period. The above period lengths were based on a simple drawdown model using previous diffusivity estimates from this site. They were selected such that experiments would yield measurable signals, provide a wide range of tested frequencies, and could be performed over a reasonable duration.

Data Analysis

All transducer and flowmeter data were imported into Microsoft Excel from the datalogger after testing. Levelogger data were then matched to datalogger data by time stamp and brought into the same Excel file. The organized spreadsheets were then imported to Matlab® as tables. Data tables consisted of head in each well and the net formation injection. We started with Rasmussen et al. 2003's confined aquifer solution to calculate estimated diffusivity, transmissivity, and storativity (D, T, and S, respectively). This is identical to the Theis solution, except the source term is sinusoidal instead of constant (Rasmussen et al., 2003). Data can be fit to this solution using parameter optimization methods or manual sine curve fitting, or broken down to phase and amplitude components. We opted for the latter so that the responses could be converted to the frequency domain, which we suspected would ease the calculation for weak drawdown responses, especially in the shorter period tests. This is often touted as one of the main advantages of periodic hydraulic testing. The amplitude attenuation and phase lag observed in monitoring wells relative to the source well at the imposed frequency can then be related to aquifer parameters.

Analytic Solutions

The sinusoidal pumping rate, Q, is given by the complex exponential

$$Q = Q_0 e^{i\omega t} = Q_0(cos\omega t + i\ sin\omega t) \tag{1}$$

where Q_0 is the amplitude of the pumping rate, ω is the frequency, t is time, and i is the imaginary number. The boundary value problem is

$$\frac{\partial^2 h}{\partial r^2} + \frac{1}{r}\frac{\partial h}{\partial r} = \frac{1}{D}\frac{\partial h}{\partial t} \tag{2}$$

$$h(r, 0) = 0 \tag{3}$$

$$h(\infty, t) = 0 \tag{4}$$

$$\lim_{r \to 0} r\,\frac{\partial h}{\partial r} = -\frac{Q}{2\pi T} \tag{5}$$

where h is head in the observation well, r is the radial distance from the pumping well, D is hydraulic diffusivity, and T is transmissivity. The differential equation (2) with initial and boundary conditions (3-5) is solved in Laplace space and inverted to the time domain using convolution, which gives

$$h(r,t) = \frac{Q}{2\pi T} K_0\left(r\sqrt{\frac{i\omega}{D}}\right) \tag{6}$$

for the steady periodic response, where K_0 is the zero-order modified Bessel function of the second kind. This solution ignores an initial, non-periodic transient term that decays with time and can typically be neglected after a few periods (Rasmussen et al., 2003). The response (6) can be broken down to amplitude and phase components by taking the modulus and complex argument, respectively:

$$|h| = \frac{Q_0}{2\pi T}\left|K_0\left(r\sqrt{\frac{i\omega}{D}}\right)\right| \tag{7}$$

$$\varphi = arg\left[K_0\left(r\sqrt{\frac{i\omega}{D}}\right)\right] \tag{8}$$

where φ is the difference between observation phase and pumping phase, $\varphi_h - \varphi_0$.

Because of borehole storage, the discharge rate at the well is not equal to the water extracted or returned to the surface tank. The actual volume of water injected into the formation (formation injection) at the pumping well at time, t, is given by

$$Q_t = \left(Q_{inj} - Q_{prd}\right) - \frac{dh}{dt}A, \tag{9}$$

where Q_{inj} and Q_{prd} are the injected and produced flow rates, respectively, measured by flow meters, and A is the cross-sectional area of the pumping well. The negative sign in front of the derivative term implies that for falling head the calculated volume is entering the formation, while for rising head the volume is filling the borehole and not entering the formation. This solves the issue of wellbore storage in the pumping well. However, it was eventually discovered that wellbore storage in the observation well could not be neglected. This was brought to our attention because of some results of concurrently performed tests, which used an inverted plastic liner that completely seals the borehole and measures head in a small tube with screened intervals. Responses in this well, with a sealed borehole and thus no borehole storage effect, to identical pumping rates were a factor of 2 larger, which made it apparent that the effect of observation wellbore storage was not negligible.

To account for observation well storage we adopted the solution presented in Novakowski (1989), which superimposes the effect of wellbore storage in the observation well over the effect of pulse interference testing (Novakowski, 1989). We modified this Laplace space solution by adding a cosine forcing. The same boundary value problem above (2), has initial conditions at the well subjected to a storage factor:

$$2\pi r_w T \frac{\partial h}{\partial r} = C_o \frac{dh}{dt} \tag{10}$$

$$h(0) = 0 \tag{11}$$

The Laplace domain solution to the differential equation (2) under new initial conditions (10 and 11) as given by Novakowski (1989, Eq 17) is:

$$h_{DO} = -\frac{K_0\left(r_D\sqrt{s}\right)K_1\left(\sqrt{s}\right)}{\sqrt{s^3}C_{DO}\gamma} \tag{12}$$

where

$$\gamma = \left[K_0\left(r_D\sqrt{s}\right)\right]^2 - \varepsilon_1\varepsilon_2 \tag{13}$$

$$\varepsilon_1 = \frac{C_{DO}\sqrt{s}\,K_0\left(\sqrt{s}\right) + K_1\left(\sqrt{s}\right)}{C_{DO}\sqrt{s}} \tag{14}$$

$$\varepsilon_2 = \frac{C_{DS}\sqrt{s}\,K_0\left(\sqrt{s}\right) + K_1\left(\sqrt{s}\right)}{C_{DS}\sqrt{s}} \tag{15}$$

s is the Laplace variable, K_1 is the first-order modified Bessel function of the second kind, r_D is dimensionless radial distance, and C_{DO} and C_{DS} are dimensionless observation well and source well storage coefficients, respectively. Note that there is a presumed typographic error in Novakowski's version of equation (15), his equation (17). The dimensionless parameters are:

$$r_D = \frac{r}{r_w} \tag{16}$$

$$t_D = \frac{tT}{r_w^2 S} \tag{17}$$

$$\omega_D = \frac{2\pi r_w^2}{PD} \tag{18}$$

$$C_{DO} = \frac{C_O}{2\pi r_w^2 S} \tag{19}$$

$$C_{DS} = \frac{C_S}{2\pi r_w^2 S} \tag{20}$$

where r_D is dimensionless radial distance, t_D is dimensionless time, ω_D is dimensionless frequency, r is inter-well radius, r_w is wellbore radius, P is the period of oscillation, D is aquifer diffusivity, S is storativity, and C_O and C_S are the cross-sectional areas of the observation and source wells, respectively. Adding a cosine forcing to the Laplace domain solution for observation well head (12) gives:

$$h(s) = \frac{Q}{2\pi T}\frac{s}{s^2 + \omega_D^2}\frac{h_{DO}}{C_{DS}} \tag{21}$$

This Laplace domain solution could not be inverted analytically, so numerical inversion methods were used. However, when only the steady sinusoidal response is needed, it can be directly inverted to the steady time domain by setting the Laplace variable equal to the complex frequency, $s = i\omega$, in equations (12-15), easing calculations (Barker, 1988). This method relies on the fact that the bilateral Laplace transform is equivalent to the continuous Fourier transform for $s = i\omega$, and is often used in electrical engineering literature. Like Rasmussen et al.'s (2003) solution, the modulus and complex argument describe the amplitude and phase of responses such that

$$|h| = \frac{Q_0}{2\pi T}\left|\frac{h_{DO}}{C_{DS}}\right| \tag{22}$$

and

$$\varphi = arg\left[\frac{h_{DO}}{C_{DS}}\right] \tag{23}$$

where φ is the difference between observation phase and pumping phase, $\varphi_h - \varphi_0$. While it is possible to fit observation responses to equation (21) directly by optimizing hydraulic parameters, the smaller responses encountered in less connected wells and shorter period tests proved difficult to process with standard curve fitting techniques. Solving for the amplitude and phase components allowed the use of frequency domain analysis.

Frequency Domain Analysis

Frequency domain analysis involves looking at signals with respect to frequency, rather than time. Analyzing a periodic signal in the frequency domain allows the desired component to be distinguished from random noise, drift, and periodic components of a different frequency. In the frequency domain, drift would appear where frequencies approach zero, non-periodic noise would appear as being scattered across the frequency domain, and the periodic components would appear at their respective frequencies, with the desired frequency easily distinguished from others. Thus, the signal generated from pumping at a known frequency can be identified and analyzed even when it is obscure in the time domain.

A time domain signal can be converted to the frequency domain via several transforms, including the Fourier transform. The discrete Fourier transform (DFT) converts a signal into a summation of many sinusoid functions of different frequencies. The output of the DFT is a complex exponential for each discrete frequency value; the angle of this complex number (argument) and its magnitude in the complex plane give the phase and amplitude of the sinusoid at that frequency. The DFT can be computed very efficiently using a fast Fourier transform (FFT) algorithm. Here, we used the native FFT algorithm in Matlab®. We computed the FFT for the formation injection and each observation well response at each different period length test, then found the phase and amplitude at the frequency corresponding to the imposed pumping period.

Digital filtering can remove unwanted frequency components. A low-pass filter attenuates all frequencies above the filter criteria and allows lower frequencies to “pass”, a high-pass filter attenuates low frequencies and passes high ones, and a band-pass filter attenuates all frequencies above and below a specified range, or “passband”. We utilized a high-pass filter to remove drift from the observation head responses. The filter, designed using Matlab®’s Filter

Design and Analysis toolbox, was a high-pass Butterworth filter with the stopband at 50% of pumping frequency and passband at 90% of pumping frequency.

A band-pass filter would yield the cleanest signal because it removes all noise and drift, leaving only the desired frequency. However, we avoided this approach because it can give misleading results. Any time domain function can be approximated by a sum of sinusoids at many different frequencies and varying amplitude and phase. For example, the FFT of a linear function has spectral power across the entire frequency domain, with the greatest amplitude at the lowest frequency. Band-pass filtering this result would pass only the desired frequency component and the signal would be a clear sinusoid with the amplitude of that frequency component used in the approximation. To avoid interpreting these artifacts of filtering, we use a high-pass filter to remove drift and use the leftover noise as qualifying criteria for the presence of a response. A signal at the pumping frequency must be greater than the amplitude of any other present frequencies (i.e. the dominant frequency) to be considered and included in parameter estimation.

The frequency domain given by the FFT is not continuous, but instead consists of discrete frequency points, often called FFT bins. An FFT of a time series with N points will have N bins. The bin values range from 0 to N-1, and are spaced by the bin resolution

$$bin\ resolution = \frac{F_s}{N} \tag{24}$$

where F_s is the sampling frequency of the time series (e.g. Dressler, 2006). The first bin value (0^{th} bin) is called the DC component, and it contains the mean of all time-series values. Head responses had very large DC components because they were not detrended and therefore not centered about zero before transformation. These components were attenuated by high-pass filtering, rather than removed individually, because non-zero, low frequency components were typically large as well. Filtering allowed the DC and other low frequencies to be removed in a single step.

If N is a multiple of the period, then the bin resolution will be such that a bin falls exactly on the frequency of the pumping period. Because of this, we truncated the time series data to a multiple of period before performing the FFT. This reduces spectral leakage, which means that the amplitude spectra are spread into surrounding bins, affecting FFT magnitudes. Although it is common to pad a time signal with trailing zeros to make its length a power of two, making the FFT algorithm run more efficiently, this technique did not result in any significant computation time savings using these relatively small datasets.

The FFT phase value cannot always be taken at face value. Because $n\pi$ is equal to $2n\pi$, a phase lag of more than 2π will not be apparent. The signal must be “unwrapped” to recover the true phase difference when that difference is more than one period. The phase component, which is the angle of the complex number output at each discrete frequency, is measured in radians counter-clockwise for positive imaginary components and clockwise for negative imaginary components, giving angles between $\pm \pi$. In the data obtained here, no phase lags were greater than 2π, with the greatest lag around $3\pi/2$. However, there were several cases where the measured phase difference (lag) for an observation well was positive, suggesting that it was *ahead* of the injection phase. This is clearly impossible, so 2π was subtracted from the phase in those cases. All phase lag values were confirmed to be reasonable by observing the filtered time domain responses and estimating the difference in peaks and troughs of the sinusoids, thus avoiding errors of 2π in the phase values.

CHAPTER 5

RESULTS

The data obtained from field experiments are presented in this section. First, the formation injection rates and head responses in the time domain are presented and organized by each period length test. Second, the frequency domain results are presented. Some example frequency versus FFT amplitude plots are shown and resulting magnitude and phase data are tabulated, leading to a comparison of amplitude and phase results for various head responses. Unmeasurable responses are shown and described. Third, the resulting parameter estimates are presented. All field results are from sinusoidal pumping tests conducted on July 21 and 22, 2015.

Head Responses

After the onset of sinusoidal pumping, the pressure response propagates through the aquifer and causes water level changes in the observation wells, and these changes are measured by the pressure transducers. The sinusoidal response to the sinusoidal formation injection exhibits a time delay and an amplitude decrease (referred to as phase lag and attenuation, respectively) that is a function of distance from the source well and the hydraulic properties of the aquifer. If the aquifer were spatially homogeneous, the response would be identical at all points equidistant from the source well. Given the similar well distances (~30-45m), the responses were highly varied in terms of phase lag and attenuation, indicating hydraulic heterogeneity. The response from FSE10a is one of the more attenuated and lagged responses despite being the closest to the source well. The following figures plot head vs time and formation injection vs time for each period (**Figure 11 - Figure 16**). For these figures, observation well responses are detrended by removing linear drift. This was accomplished using Matlab®'s *detrend* function, which computes the straight line of best fit to data using leastsquares and then subtracts this line from data. Thus, the effects of arbitrary transducer installation depth and drift from unequal pumping and injection are removed for clearer visual inspection.

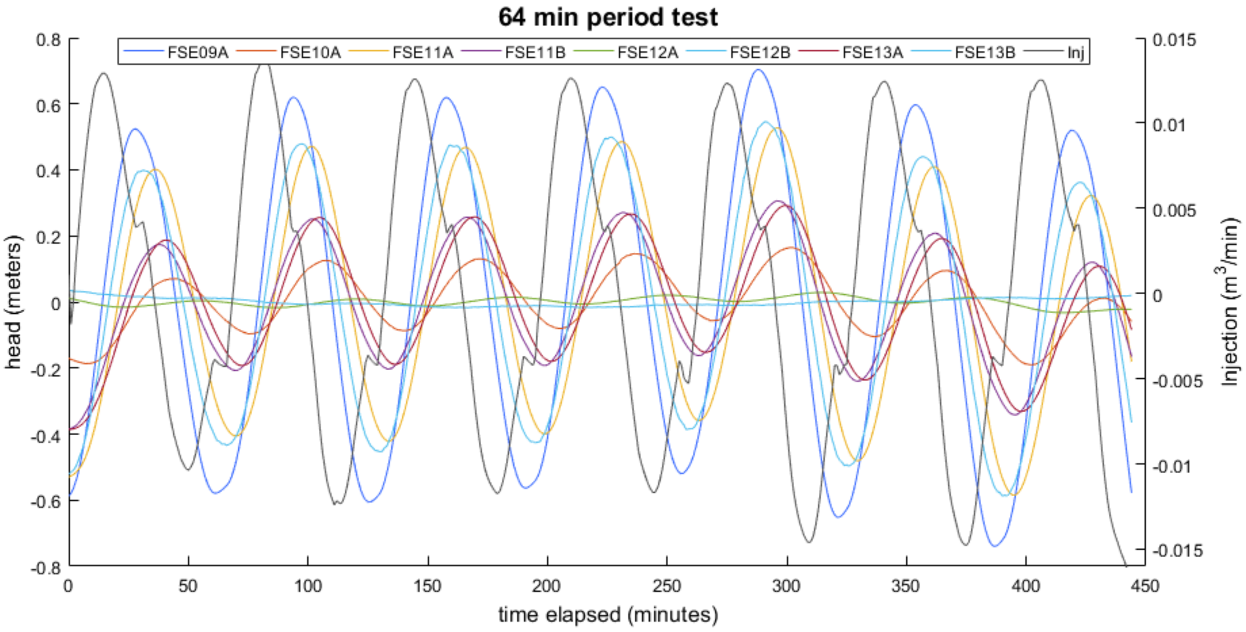

Figure 11. Plot of head response at observation points and formation injection – 64 min period

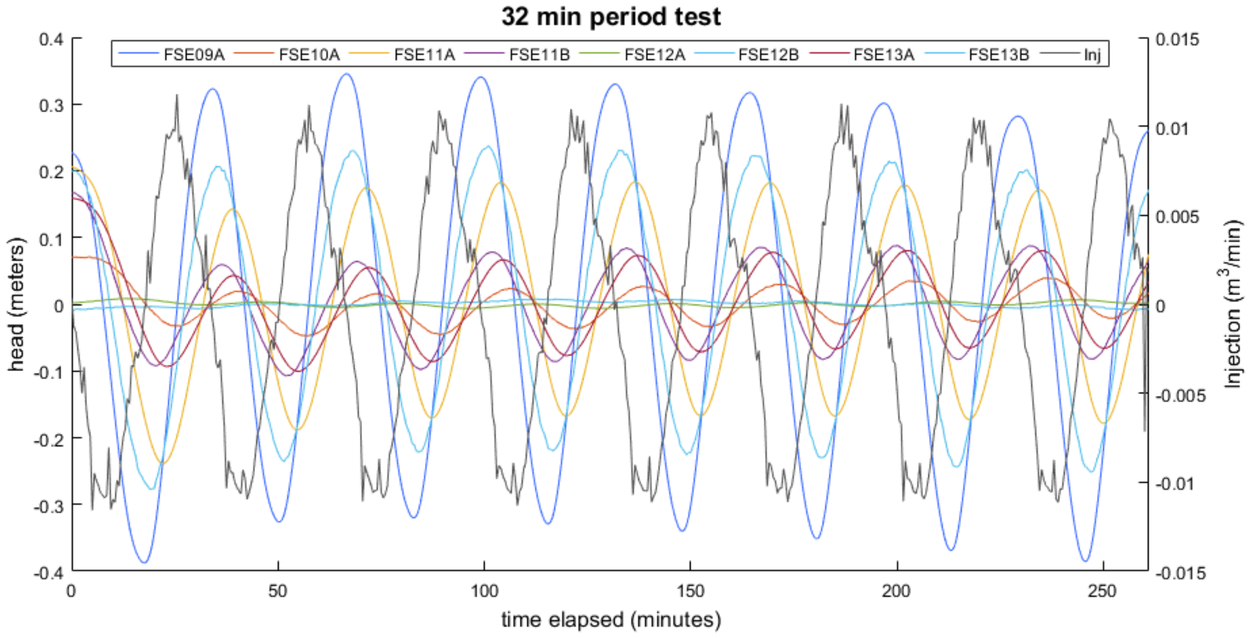

Figure 12. Plot of head response at observation points and formation injection – 32 min period

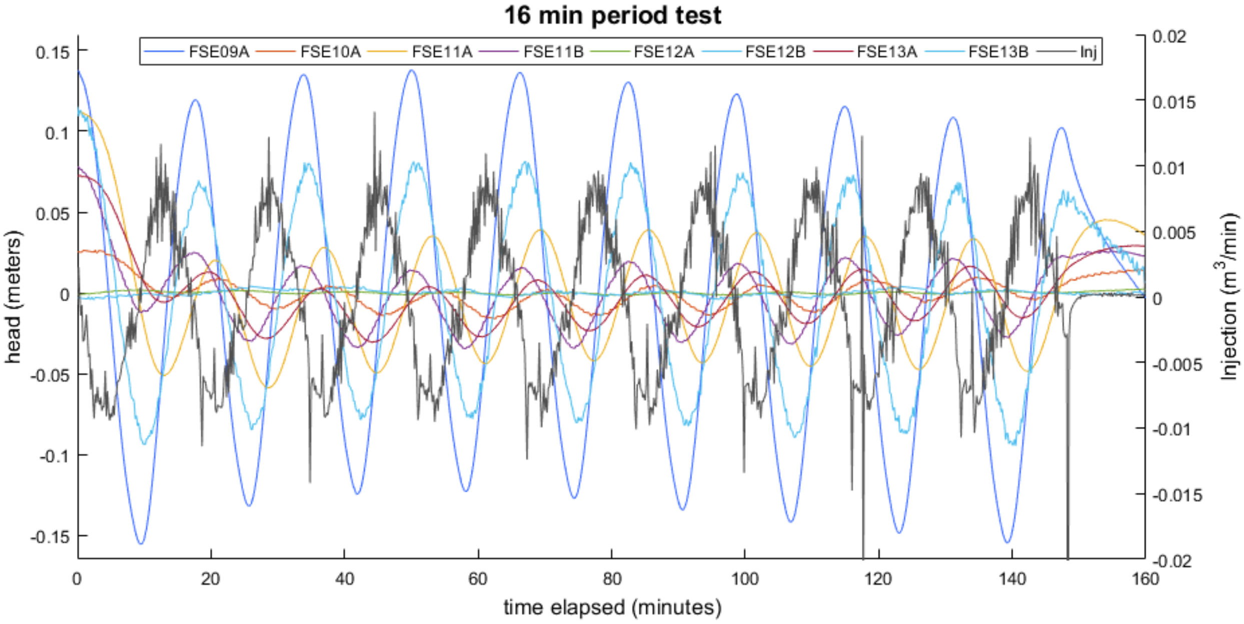

Figure 13. Plot of head response at observation points and formation injection – 16 min period

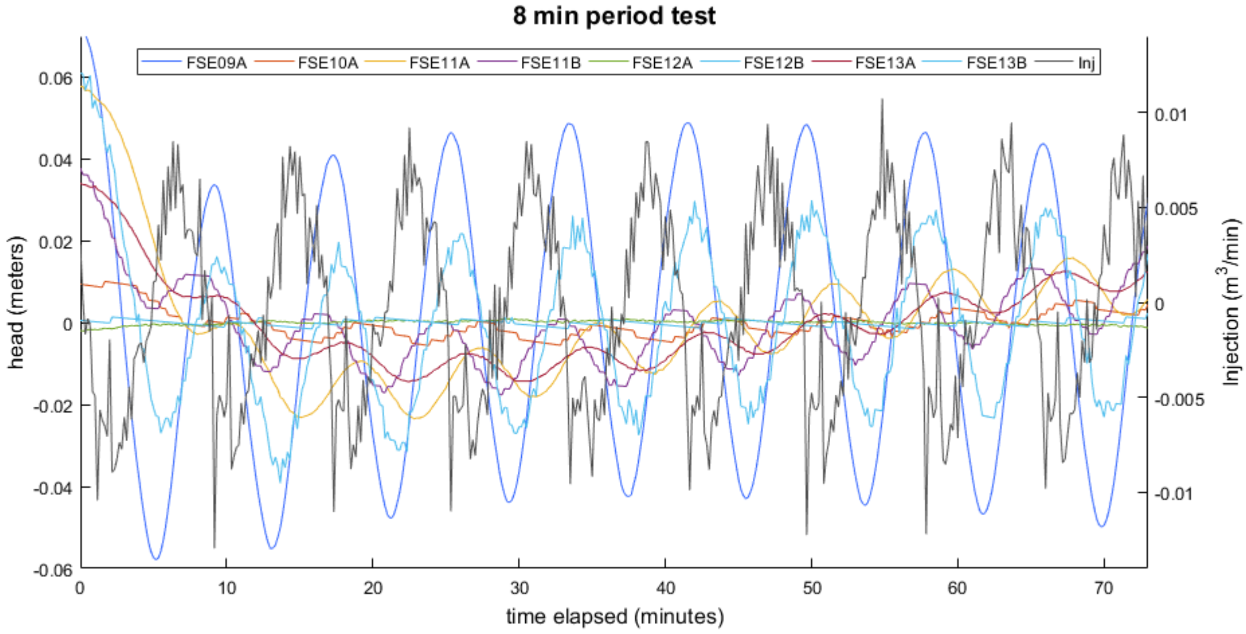

Figure 14. Plot of head response at observation points and formation injection – 8 min period

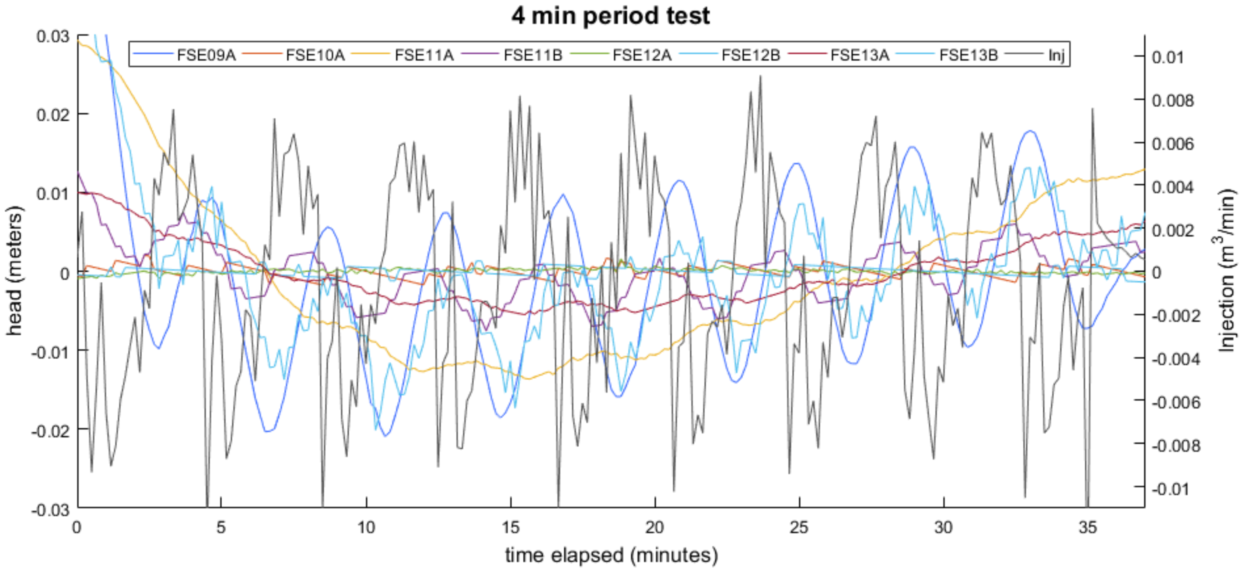

Figure 15. Plot of head response at observation points and formation injection – 4 min period

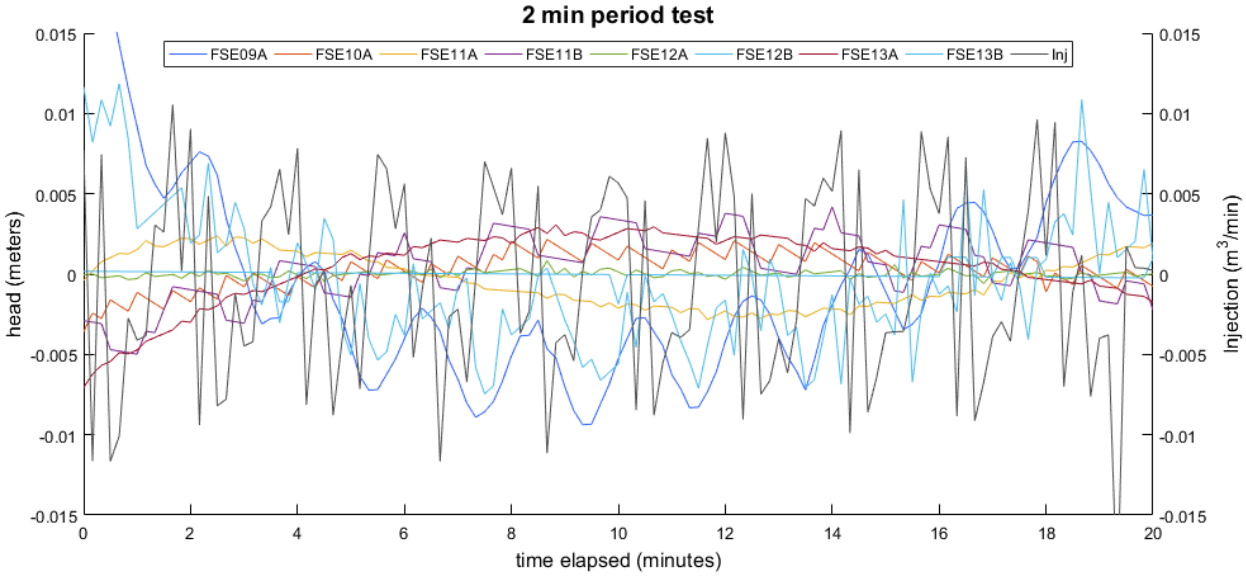

Figure 16. Plot of head response at observation points and formation injection – 2 min period

Observation of these plots offers a few key insights and explanations. Regarding injection rates, the noisy curves are a result of the calculation for formation injection (equation 9), which uses the head derivative in the pumping well given by $(h_{j+1} - h_j)/(t_{j+1}-t_j)$. This method gives a less smooth result as the size of the time step relative to the period becomes larger. Sampling intervals were 60 seconds for the 64-minute test and 30 seconds for the 32-minute test (64 samples per period), and 10 seconds for all shorter tests (12 samples per period for 2-minute period). This under-sampling effect, coupled with turbulence in the pumping well, results in noisier estimations of injection rates as period decreases. However, the real injection rate is assumed to be sinusoidal, and any noise in the data is avoided in the frequency domain.

Linear drift seen in observation wells (removed here by detrending) and a noticeable non-linear drift still present after detrending are likely caused by the unequal pumping and injection rates, described earlier. This would imprint an overall withdrawal or injection regime over the sinusoidal variation and would create a head response like that of a conventional pumping or slug test, plus a sinusoidal response (e.g **Figure 16**). Another cause of drift could be running an unequal number of injection and withdrawal cycles. For example, the 4-minute test inadvertently had 9 withdrawal cycles and only 8 injection cycles (**Figure 15)**. After the final withdrawal cycle, heads would have been recovering in the well field as the next test's (8-minute) withdrawal began.

Regarding the attenuation and phase lag in observation wells, FSE09a typically has the strongest response to pumping (i.e. least attenuation and lag), while FSE12a and FSE12b have the weakest response. Between these extremes, FSE 10a, FSE11a, FSE11b, FSE13a, and FSE13b exhibit a moderate response, although FSE10a is about 10 m closer to the pumping well than the others. It is interesting to note that attenuation and phase lag are not proportional. If that were the case, one would expect that smaller response amplitudes would also be further behind in phase than larger amplitudes. This is proved to be not true, for example, by comparing FSE11a (yellow) and FSE11b (purple) in the 16-minute test (**Figure 13**). Though the two points are equidistant from the pumping well, FSE11a has a larger amplitude than FSE11b, but it has a greater phase lag.

As the period length increases, responses become stronger. This is due to a combined effect of a larger total volume of water injected/withdrawn and a greater radius of penetration into the aquifer. When doubling the period length from 32 to 64 minutes, the total volume injected/withdrawn is doubled, but it is interesting to note that the formation injection exhibits a diminished return on longer periods, only increasing from about 0.010 to 0.012 m^3/min (**Figure 11, Figure 12**). There is an interesting change in relative phase lag between FSE09a (blue) and FSE11b (purple) as period decreases. In the 64 and 32-minute tests, FSE09a is closer in phase to the formation injection than FSE11b (**Figure 11, Figure 12**). Then, in the 16-minute test their phases are about equal, and finally FSE11b is ahead of FSE09a in phase for the 8, 4, and 2-minute period tests (**Figure 13 - Figure 16**). Comparisons of this sort can be performed more accurately by obtaining amplitude and phase values of the sinusoidal responses.

Frequency Domain Analysis

Amplitude and phase information was retrieved from the input and observation signals using the FFT. Executed through Matlab® code, head responses were clipped to the desired length, high-pass filtered, and transformed using FFT. Then the FFT bin corresponding to the pumping frequency was determined to index the frequency domain data, giving amplitude and phase values. Plotting the amplitude values versus frequency is the best way to visualize FFT results. Looking at a strong observation response from the 64-minute test, one can see a distinct

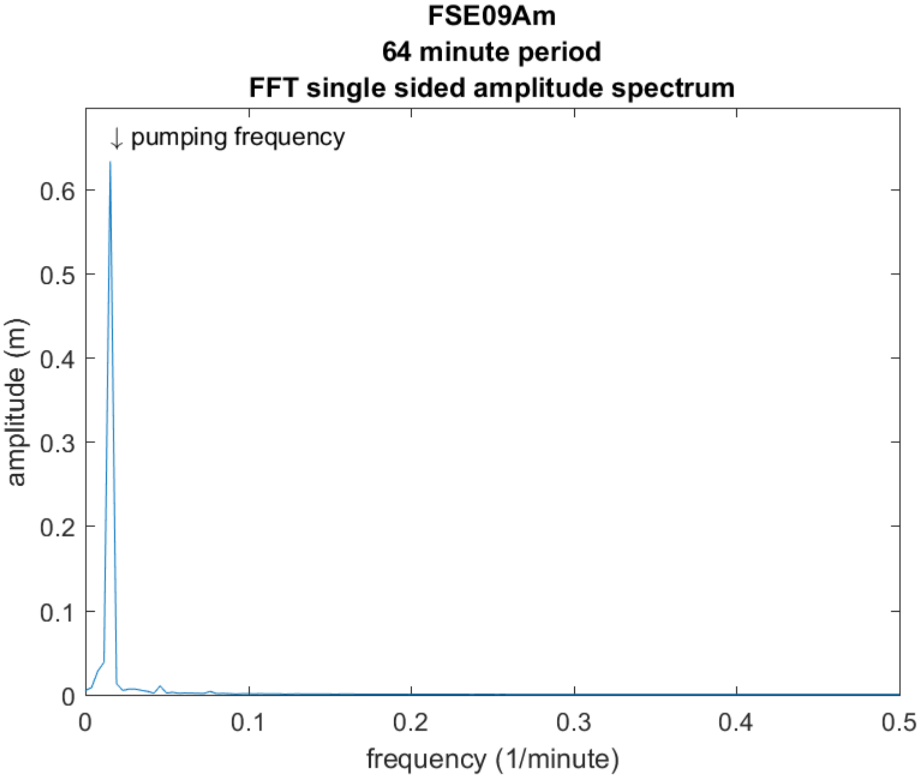

Figure 17. FFT amplitude for FSE09a, 64-minute period. The "m" after FSE09a refers to meters, as the original pressure data were in feet of head.

peak at the pumping frequency (~0.015 min^{-1}) and negligible presence of noise or other frequency signals (**Figure 17**). The two small spikes to the right of the main spike are harmonic components of the injected signal, present because the formation injection was not perfectly sinusoidal. At longer periods, all responses give very distinct spikes like this, and are even unambiguous in the time domain. **Figure 18** is the FFT amplitude of the weakest observation response for the 64-minute test, FSE12b, which still has a distinct signal at the input frequency and is much greater than any other frequencies present. For brevity, not all amplitude spectra plots are included. Most responses are similar to **Figure 17** and **Figure 18**, easily meeting the selected criteria; they have a strong peak at the pumping frequency and minimal spectral power at higher frequencies.

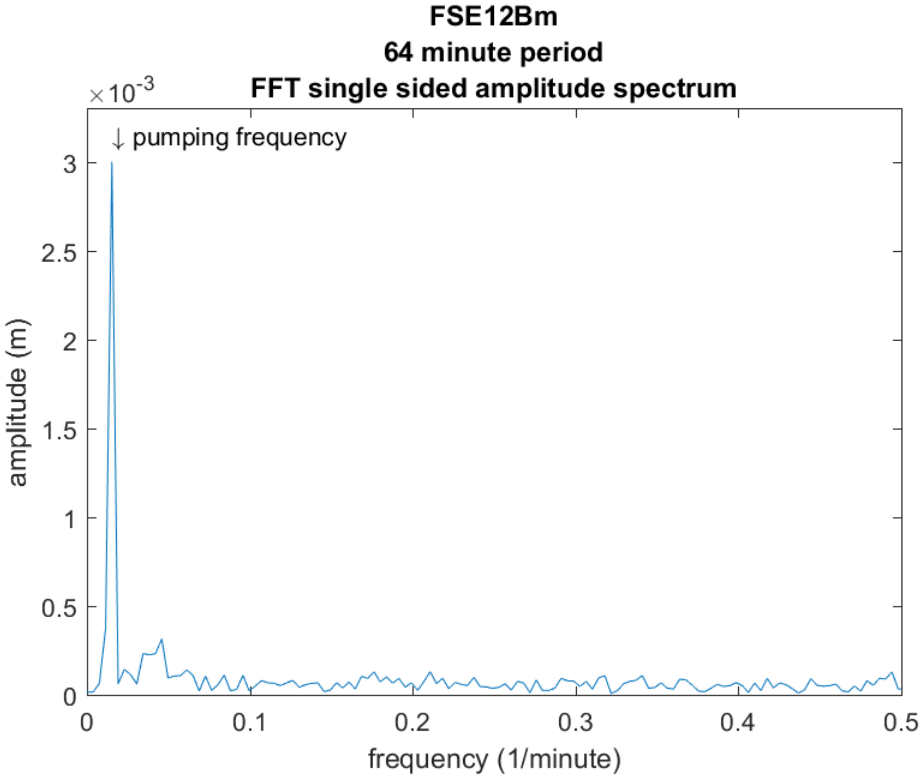

Figure 18. FFT amplitude for FSE12b, 64-minute period

Amplitude and Phase Values

The following tables summarize the amplitude and phase values of both formation injection (flow rate) and observation responses (heads). The columns are the test period length in minutes and the rows indicate the observation point. Distance from the pumping well is also included in the left most column. **Table 5** contains the amplitude data and **Table 6** contains attenuation values (observation amplitude divided by injection amplitude). **Table 7** contains the phase data. **Table 8** contains the phase lag values, calculated by subtracting the injection phase from the observation phase. For values highlighted in orange either the pumping frequency was not dominant, had amplitudes smaller than the transducer resolution, or both.

Table 9 is the same as **Table 8**, but six phase lags have been corrected (marked by an asterisk) by subtracting 2π. This correction was performed because the reported phase values for these observation points were ahead of the injection phase, which is not physically possible. **Table 6** and **Table 9** contain the amplitude and phase data, respectively, used in parameter estimation according to **Equations 22** and **23.**

Table 5. Summary of Amplitudes Calculated Using FFT

Amplitudes from FFT (m)							
radial dist. (m)		2	4	8	16	32	64
0	Injection (m^3/min)	0.005672	0.005659	0.006437	0.007605	0.009858	0.011857
36.27	FSE09A	0.003075	0.013175	0.045287	0.129637	0.338306	0.632773
30.04	FSE10A	7.78E-05	0.00065	0.002274	0.008012	0.031446	0.112316
43.71	FSE11A	0.000111	0.001027	0.007448	0.040506	0.176044	0.451991
43.71	FSE11B	0.001553	0.003564	0.008523	0.024095	0.083189	0.234259
47.01	FSE12A	3.67E-05	9.54E-05	0.000225	0.000752	0.003276	0.012364
47.01	FSE12B	0.000138	0.000191	0.000594	0.001248	0.002202	0.003006
39.89	FSE13A	0.000194	0.000716	0.003604	0.016358	0.073864	0.226382
39.89	FSE13B	0.002158	0.006642	0.023905	0.077579	0.228152	0.480833
	FSE14	0.002266	0.000541	0.006227	0.020334	0.085719	0.243699

Table 6. Summary of Attenuations (amplitude/injection rate)

Normalized amplitude (amplitude/injection rate)							
radial dist. (m)		2	4	8	16	32	64
0	Injection (m^3/min)	1	1	1	1	1	1
36.27	FSE09A	0.542125	2.328332	7.035451	17.0458	34.31699	53.36616
30.04	FSE10A	0.013726	0.114894	0.353305	1.053429	3.189778	9.472416
43.71	FSE11A	0.019626	0.181573	1.15701	5.326088	17.8575	38.11957
43.71	FSE11B	0.273753	0.629934	1.324059	3.168265	8.438558	19.75674
47.01	FSE12A	0.006463	0.016856	0.034934	0.098875	0.332329	1.042779
47.01	FSE12B	0.02435	0.0338	0.092237	0.164081	0.223407	0.253483
39.89	FSE13A	0.034218	0.126603	0.55985	2.150938	7.492591	19.09239
39.89	FSE13B	0.380573	1.173748	3.713701	10.20075	23.14321	40.55206
	FSE14	0.399475	0.095523	0.967406	2.673728	8.695175	20.55288

Table 7. Summary of Phases Calculated Using FFT

Phases from FFT							
radial dist. (m)		2	4	8	16	32	64
0	Injection	0.91686	1.50434	1.803328	2.011354	1.927141	-1.07805
36.27	FSE09A	-0.99137	-0.52528	-0.15714	0.23032	0.330132	-2.27411
30.04	FSE10A	1.971847	-2.56439	-2.04269	-1.34161	-1.03597	2.786119
43.71	FSE11A	-2.97389	-2.1717	-1.64097	-1.031	-0.65007	-2.93184
43.71	FSE11B	0.397429	0.536121	0.377653	0.161396	-0.14888	-2.91441
47.01	FSE12A	0.310016	2.675223	-2.96335	-2.60696	-2.33645	1.602203
47.01	FSE12B	-2.51017	-2.42034	-2.61567	-2.18956	-2.35918	0.94408
39.89	FSE13A	-1.96651	-1.3995	-1.0985	-0.80672	-0.72611	3.057637
39.89	FSE13B	-1.45236	-0.92123	-0.53329	-0.09104	0.041191	-2.52558
	FSE14	2.044452	-1.15382	-1.08011	-0.64865	-0.55692	-3.08691

Table 8. Summary of Phase Lags Calculated from Phases (above)

Phase lag from FFT (observation - injection)							
radial dist. (m)		2	4	8	16	32	64
0	Injection	0	0	0	0	0	0
36.27	FSE09A	-1.90823	-2.02962	-1.96047	-1.78103	-1.59701	-1.19606
30.04	FSE10A	1.054987	-4.06873	-3.84601	-3.35296	-2.96311	3.864173
43.71	FSE11A	-3.89075	-3.67604	-3.44429	-3.04236	-2.57721	-1.85379
43.71	FSE11B	-0.51943	-0.96822	-1.42567	-1.84996	-2.07602	-1.83636
47.01	FSE12A	-0.60684	1.170883	-4.76668	-4.61832	-4.26359	2.680257
47.01	FSE12B	-3.42703	-3.92468	-4.419	-4.20092	-4.28632	2.022134
39.89	FSE13A	-2.88337	-2.90384	-2.90183	-2.81807	-2.65325	4.13569
39.89	FSE13B	-2.36922	-2.42557	-2.33662	-2.1024	-1.88595	-1.44753
	FSE14	1.127592	-2.65816	-2.88344	-2.66	-2.48407	-2.00885

Table 9. Summary of Phase Lags After Corrections of 2π (*)

Phase lag from FFT - corrected							
radial dist. (m)		2	4	8	16	32	64
0	Injection	0	0	0	0	0	0
36.27	FSE09A	-1.90823	-2.02962	-1.96047	-1.78103	-1.59701	-1.19606
30.04	FSE10A	-5.2282*	-4.06873	-3.84601	-3.35296	-2.96311	-2.41901*
43.71	FSE11A	-3.89075	-3.67604	-3.44429	-3.04236	-2.57721	-1.85379
43.71	FSE11B	-0.51943	-0.96822	-1.42567	-1.84996	-2.07602	-1.83636
47.01	FSE12A	-0.60684	-5.1123*	-4.76668	-4.61832	-4.26359	-3.60293*
47.01	FSE12B	-3.42703	-3.92468	-4.419	-4.20092	-4.28632	-4.26105*
39.89	FSE13A	-2.88337	-2.90384	-2.90183	-2.81807	-2.65325	-2.14749*
39.89	FSE13B	-2.36922	-2.42557	-2.33662	-2.1024	-1.88595	-1.44753
	FSE14	-5.15559	-2.65816	-2.88344	-2.66	-2.48407	-2.00885

Ambiguous Responses

Only for the shorter period tests, 2 and 4-minute periods, do some of the responses fail to pass selection criteria (i.e. dominant frequency and greater than the transducer resolution). Amplitudes below the transducer resolution can be present at the pumping frequency because of random noise, not necessarily a hydraulic response, or because of a partial time domain response. The latter cause is a result of the summation in the FFT. For example, a perfect sinusoid with an amplitude of 1 mm that is present for just half of the time domain would have an FFT amplitude of 0.5 mm at that frequency. **Figure 20** through **Figure 27** show the FFT amplitude for responses that did not pass these criteria.

Figure 19 is the shortest period (8-minute) for which FSE12b has a qualifying response. With a Levelogger resolution of 1.0 mm, this response amplitude of just over 0.5 mm is approaching the limit of a detectable signal because a sinusoid's amplitude is half of the peak minus trough height. Even though it is barely above the transducer resolution, the FFT amplitude plot shows that the pumping frequency is at least three times greater than any other frequency present.

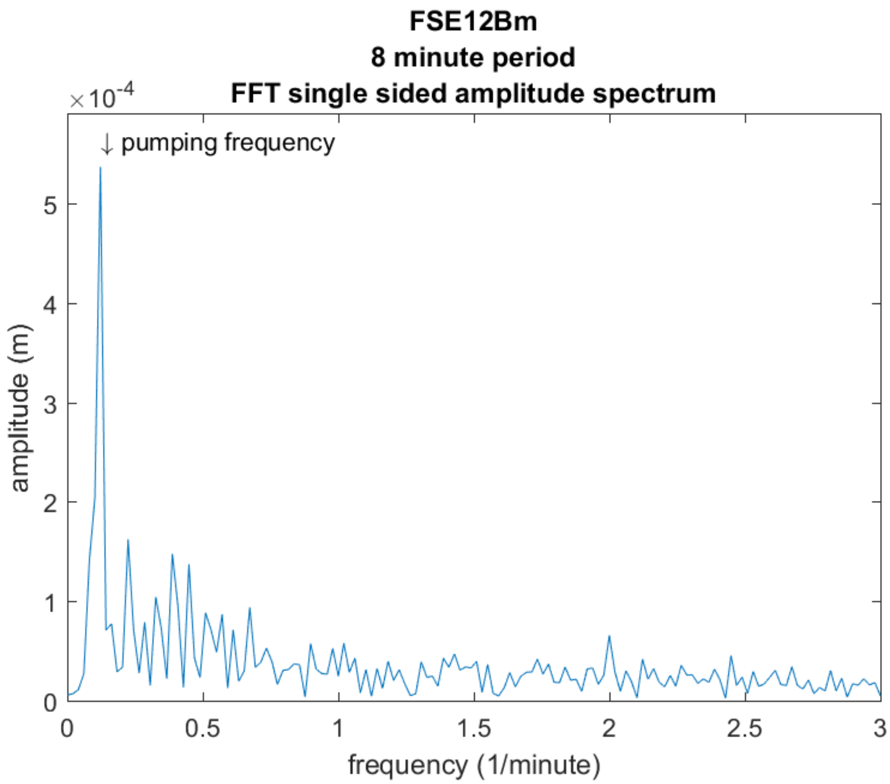

Figure 19. FFT amplitude for FSE12b, 8-minute period. Shown as an example that narrowly passes the criteria because the dominant frequency is just above the transducer resolution.

The FFT amplitude plot for FSE 10a is an example of the pumping frequency not being the dominant frequency (**Figure 20**). Not only are other frequencies within the domain greater, but it is not even a spike relative to other nearby frequencies. The response to pumping is not distinguishable and is well below the background noise. Because of its low signal-to-noise ratio, it should not be considered a robust response. The following figures are for all observation well responses that did not meet the criteria. The amplitude and phase values for these responses were not used in parameter estimation.

Both the time and frequency domain results of head responses for FSE12b, 4 and 2-minute periods, are shown in **Figure 24** and **Figure 25**, respectively. The time data are raw, meaning they have not been detrended or filtered. Each increase or decrease in head occurs as a single step of about 1.0 mm, which is the resolution of the Levelogger used in FSE12b. Blindly accepting values given by the FFT, or using a bandpass filter, could lead one to mistake the signal output for a response induced by pumping. In each of these cases the FFT amplitude at the pumping frequency is well below half of the transducer resolution.

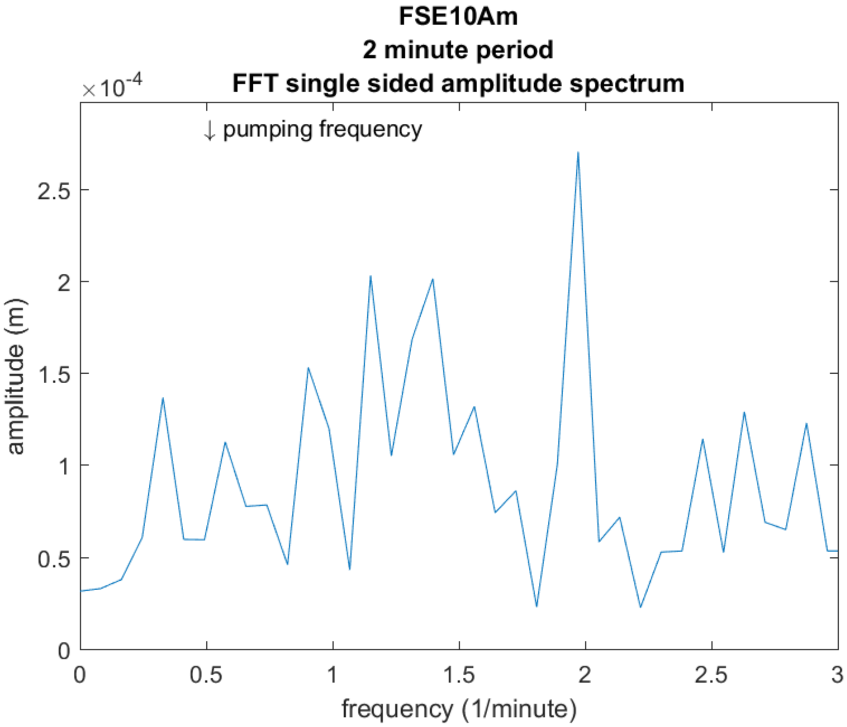

Figure 20. FFT amplitude for FSE10a, 2-minute period. Pumping frequency is not dominant and is below the transducer resolution.

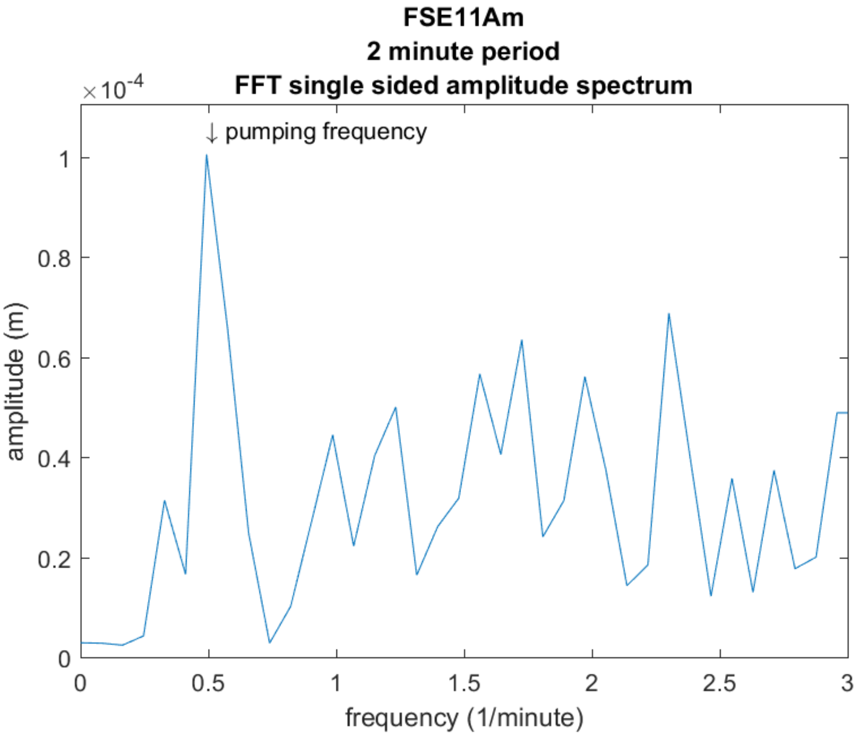

Figure 21. FFT amplitude for FSE11a, 2-minute period. Although the pumping frequency is dominant, it is below the transducer resolution.

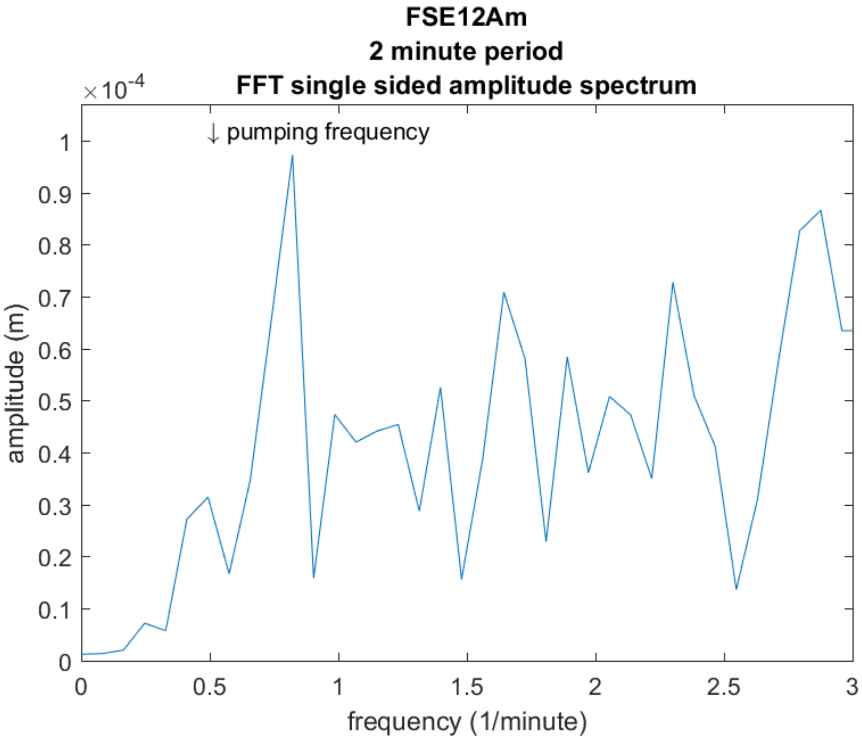

Figure 22. FFT amplitude for FSE12a, 2-minute period. Pumping frequency is not dominant and is below the transducer resolution.

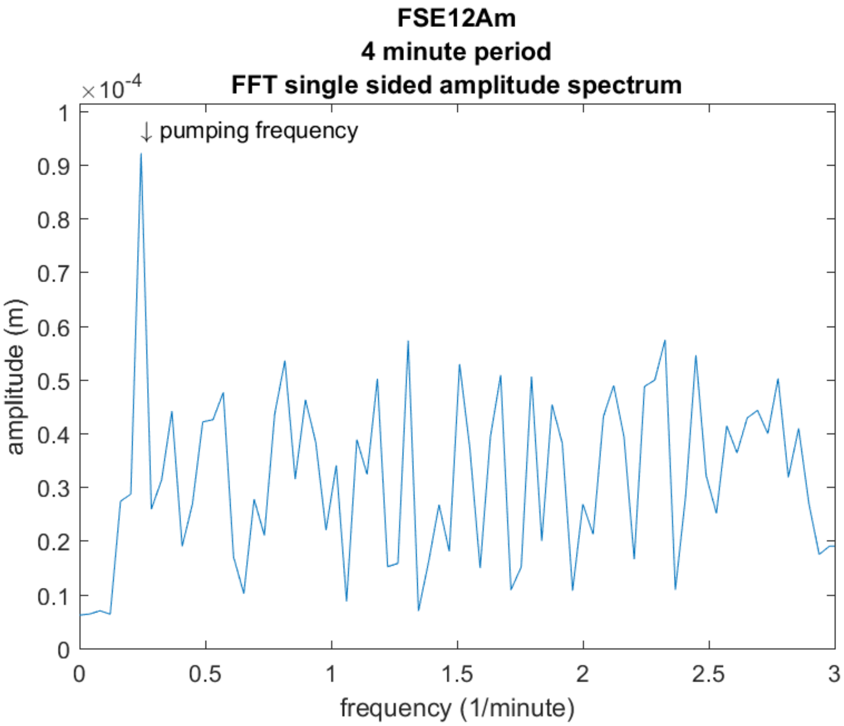

Figure 23. FFT amplitude for FSE12a, 4-minute period. Although the pumping frequency is dominant, it is below the transducer resolution.

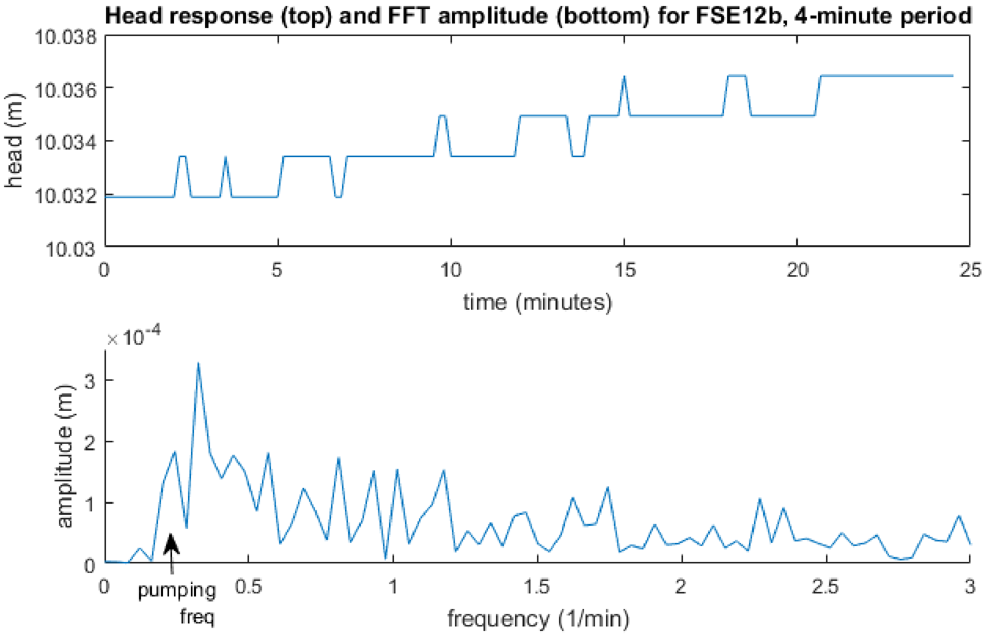

Figure 24. Time and frequency domain response for FSE12b, 4-minute period. Unfiltered time series data included to show steps of ~1 mm, the transducer resolution.

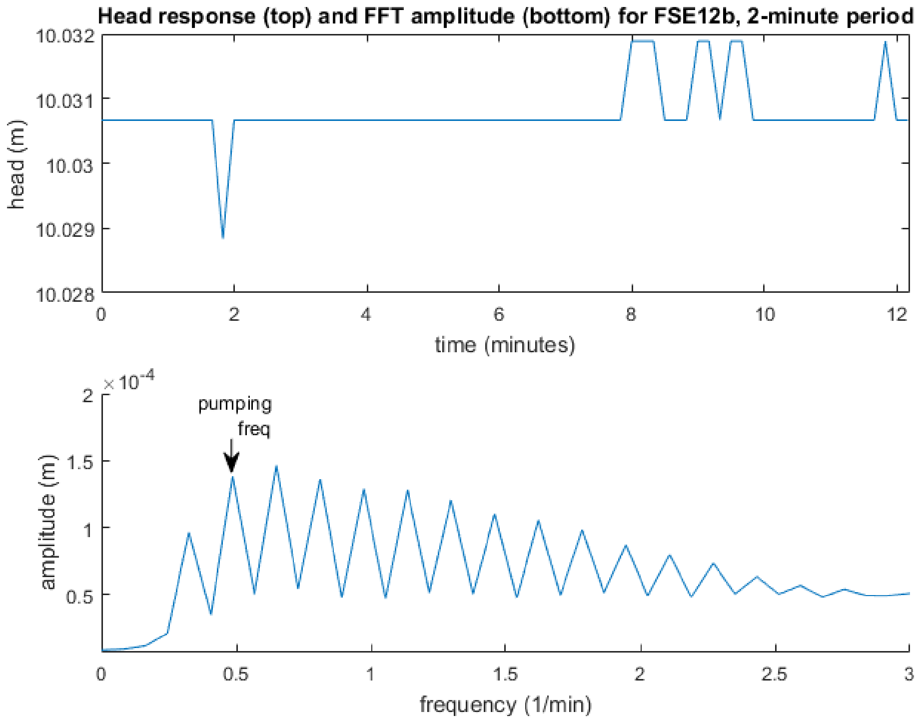

Figure 25. Time and frequency domain response for FSE12b, 2-minute period. Unfiltered time series data included to show steps of ~1 mm, the transducer resolution.

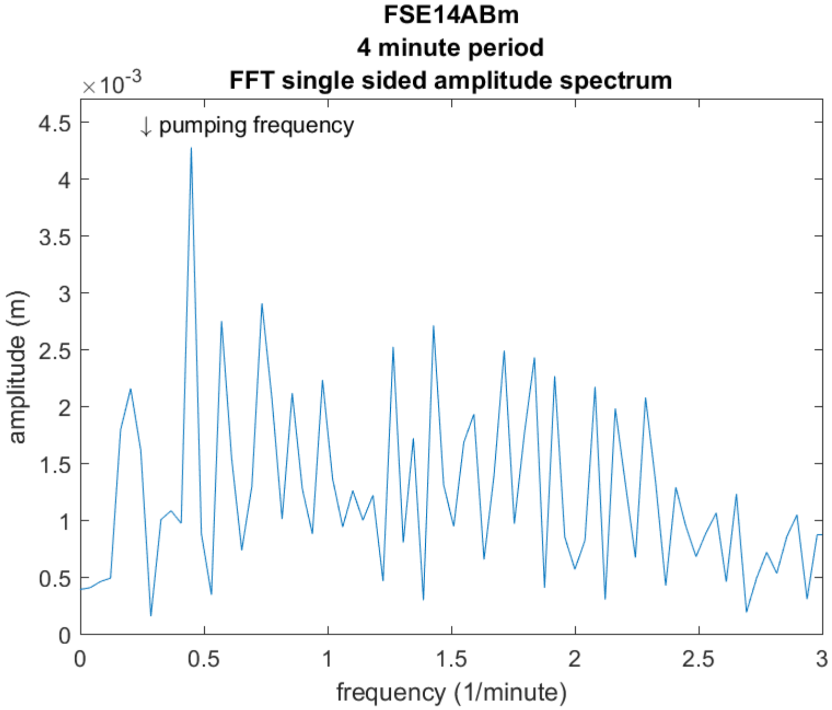

Figure 26. FFT amplitude for FSE14, 4-minute period. Pumping frequency is not dominant.

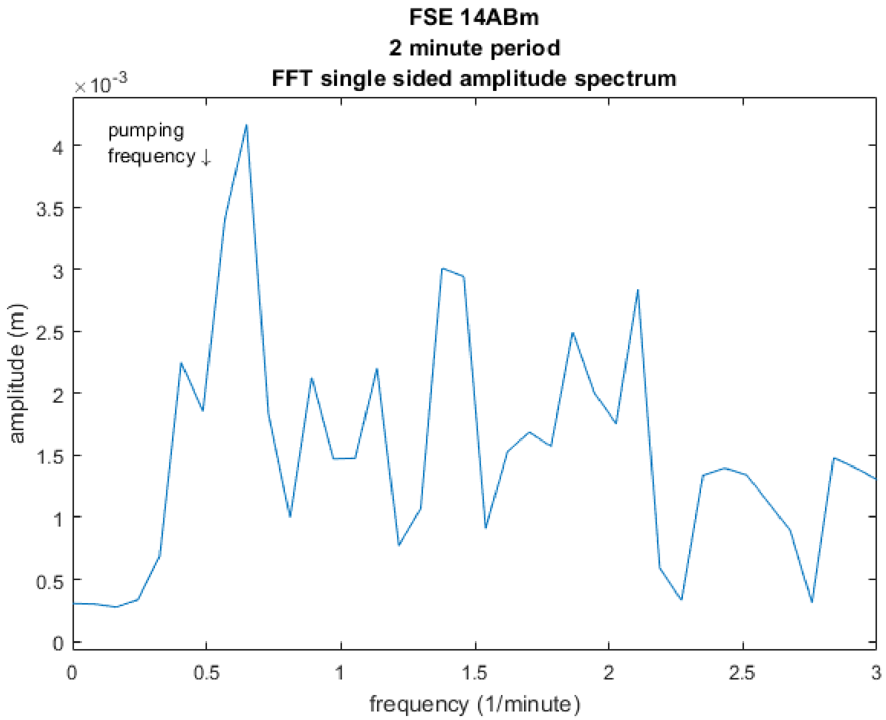

Figure 27. FFT amplitude for FSE14, 2-minute period. Pumping frequency is not dominant.

Comparing phase lag and attenuation

Using the attenuation and phase lag derived from frequency domain analysis, one can more accurately and quantitively describe the same behaviors discussed after observing the detrended head responses. **Figure 28** shows the amplitude of responses for each test and the distance from the pumping well. For all period lengths, FSE09a has the strongest response in terms of amplitude, followed by FSE13b. FSE11a is the third strongest response for long periods (16-64 minutes), but then drops below FSE11b for shorter periods (2-8 minutes). These are followed by FSE14, FSE13a, and FSE10a in decreasing amplitude. FSE12a and b are the weakest responders, with “a” slightly higher than “b” for long periods (32 and 64 minutes) and vice versa for shorter periods (8 and 16 minutes). Both points had unreliable responses for 2 and 4-minute periods, possibly indicating that they were outside of the radius of influence for those tests. Note that these values are “normalized amplitudes” (**Table 6**).

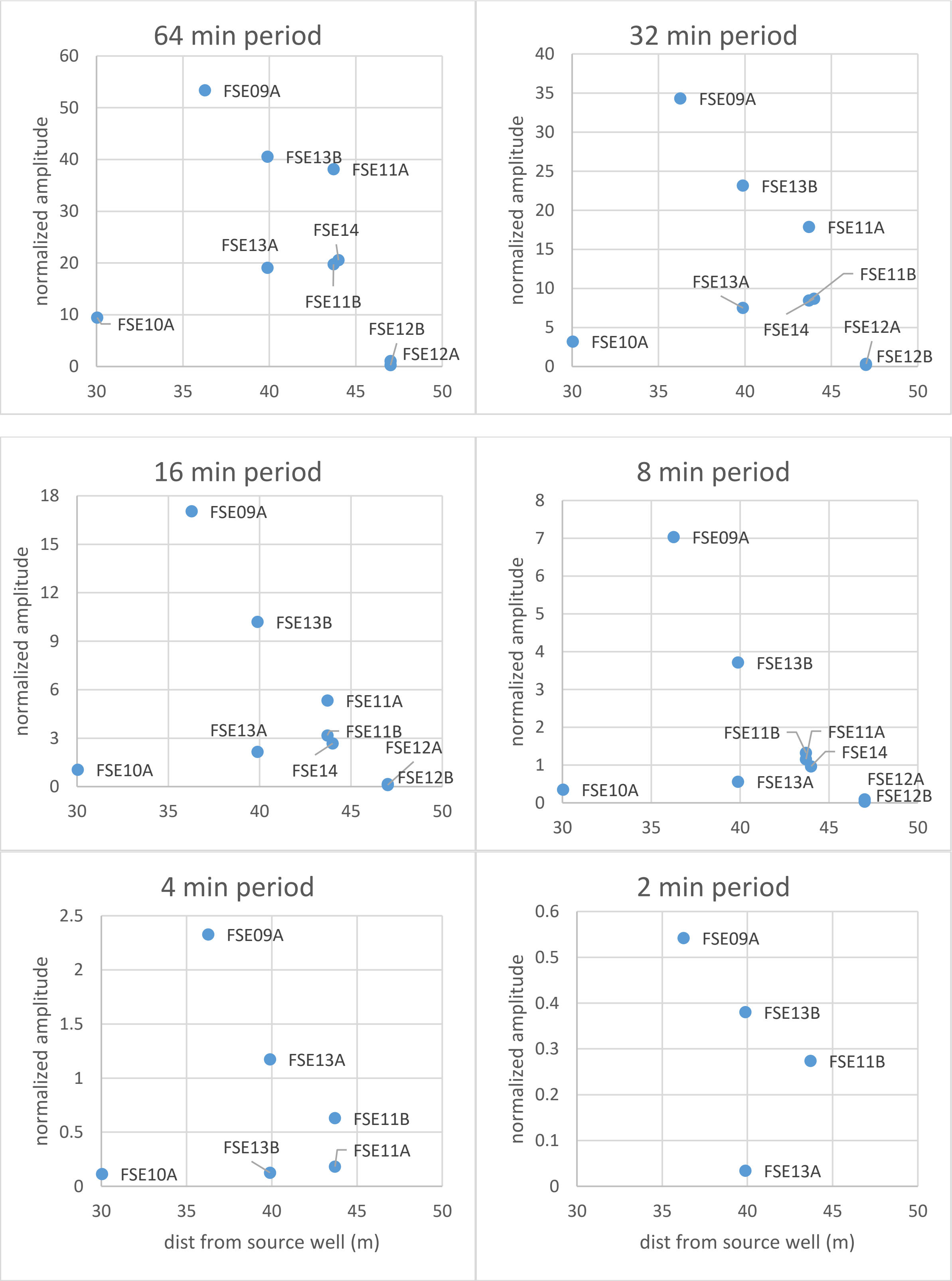

Figure 28. Normalized amplitude vs distance from pumping well. 64-minute period (top left) through 2-minute period (bottom right)

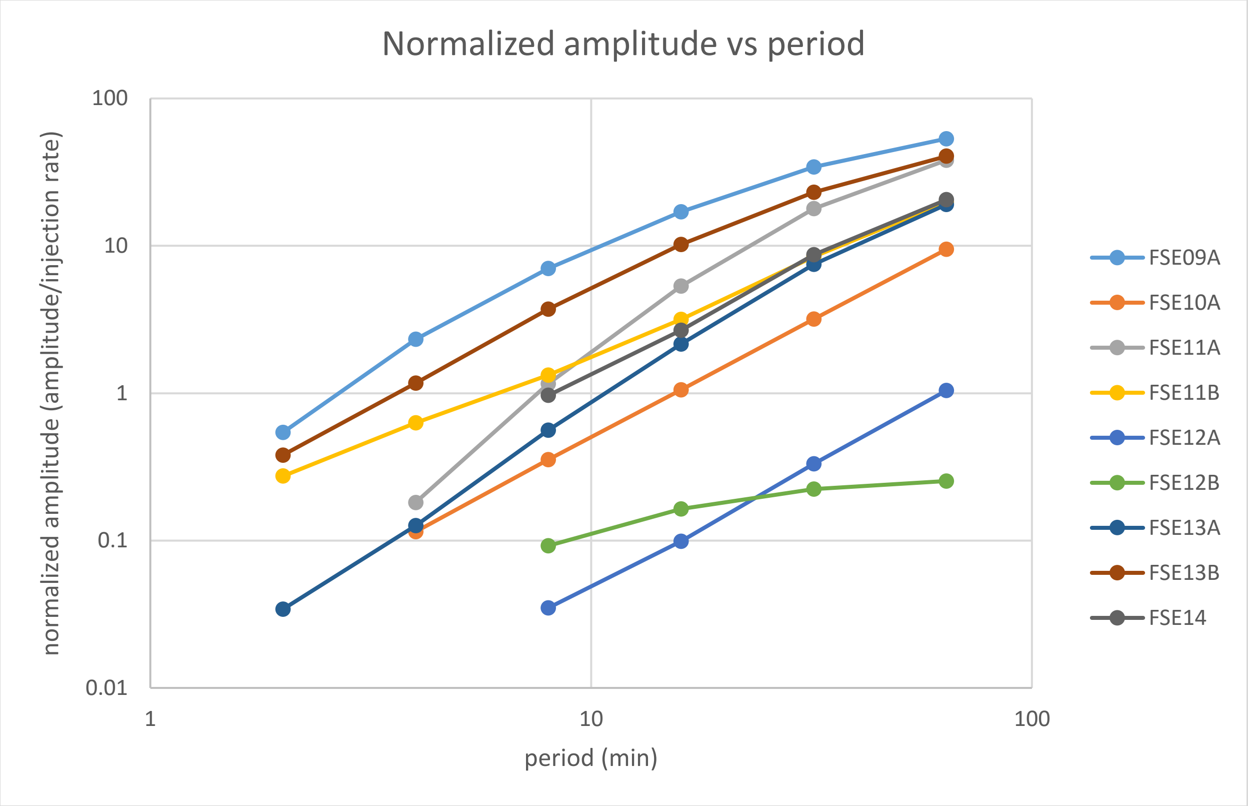

Figure 29. Observation amplitudes normalized by formation injection rate amplitude, plotted against period length. Both axes are logarithmic.

Plotting the normalized amplitude vs period (**Figure 29**) shows that response amplitudes always increase with period length, due to both the increased volume of water injected/withdrawn and the effects of period length, which include radius of influence and the fact that shorter wavelengths are dampened more quickly than long wavelengths moving through a medium. There is a logarithmic relationship between amplitude and period length, much like the logarithmic relationship between drawdown and time in a constant rate test. The graph succinctly summarizes the individual responses from **Figure 28**. The total volume of water injected/withdrawn is easily calculated (assuming sinusoidal injection) by taking the definite integral over one half period of the injection rate with respect to time, which simplifies to $P/\pi * Q_{max}$. Dividing the response amplitudes by this total volume injected may better reflect the effects of period alone (**Figure 30**). As expected, these normalized amplitudes increase as period increases. However, amplitude decreases over all periods for FSE12b, and from 32 to 64-minute periods for FSE09a and FSE13b.

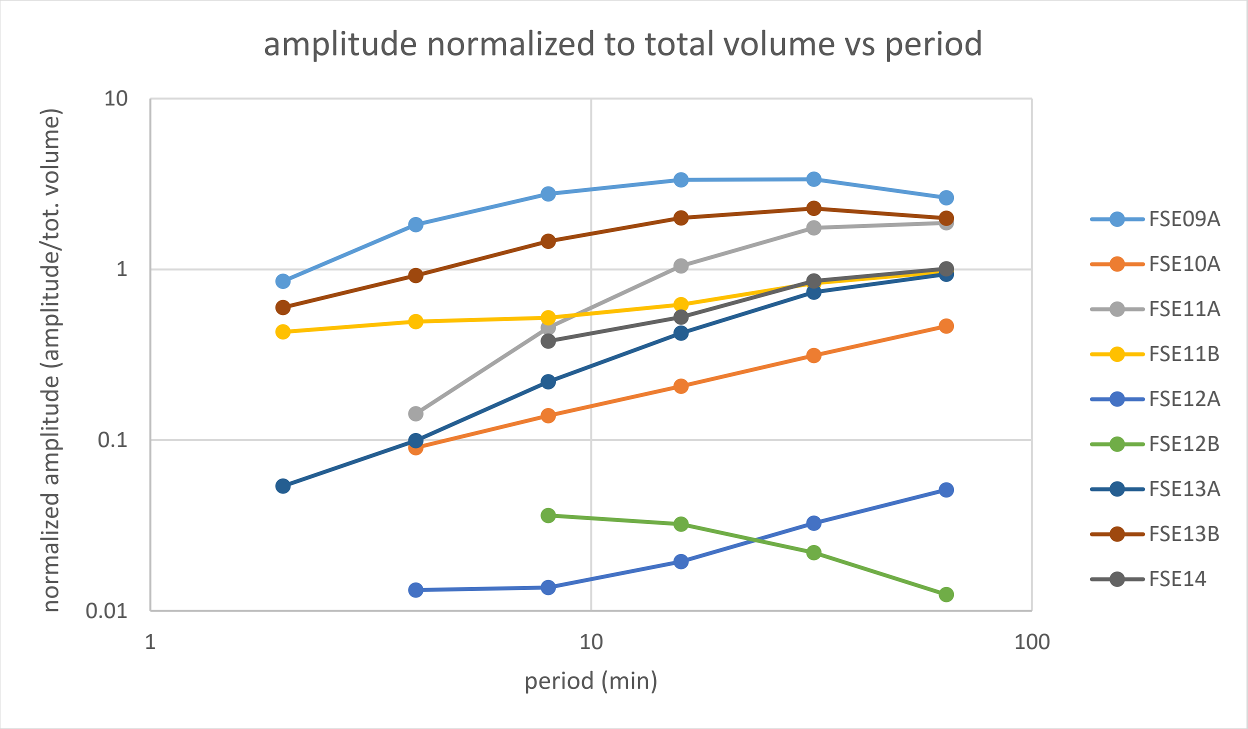

Figure 30. Observation amplitudes normalized by total volume injected, plotted against period length. Both axes are logarithmic.

Phase lags for each test are plotted against distance from the pumping well (**Figure 31**). Greater phase lag represents greater lag time between the sinusoidal input and sinusoidal observation, which varies as a function of distance traveled and aquifer properties. As expected, phase lag generally increases with distance, but the relationship is not consistent, reflecting aquifer heterogeneity. The phase lags of different observation points tend to be more clustered for long periods and more varied for short periods. The phase lags of observation points relative to one another follow similar trends as amplitudes, with FSE09a, FSE11b, and FSE13b having the shortest lag times, FSE12a and b the longest, and FSE10a, FSE11a, FSE13a, and FSE14 in between those extremes. FSE10a's phase lag approaches those of FSE12a and b even though the latter two are about 50% farther from the pumping well, which suggests that FSE10a is poorly connected.

Phase lag decreases with period length (**Figure 32**). This is intuitive considering that a given time delay will be a smaller phase lag if the period is longer. The exceptions to this trend are FSE12b, for 32 and 64-minute periods, FSE09a and FSE13b for the 2-minute period, and, most drastically, FSE11b.

Attenuation and phase shift are plotted against one another for each response (**Figure 33**). These plots are similar to the “characteristic curves” presented by Ahn and Horne (2011). In their concentric ring model, these displayed different trends for varying heterogeneity structures and were invariant for varying parameters with the same heterogeneity structure (Ahn and Horne, 2011). With our data, the trends group together according to connectivity, as determined by diffusivity (discussed next). The groups converge for large attenuation, which corresponds to large pumping periods, and diverge for small values of attenuation. It is worth noting that all trends observed by Ahn and Horne (2011) for their ring model displayed increasing phase shift for decreasing attenuation. Here, FSE09a, FSE13b, and, most notably FSE11b, began to decrease in phase shift as attenuation decreased.

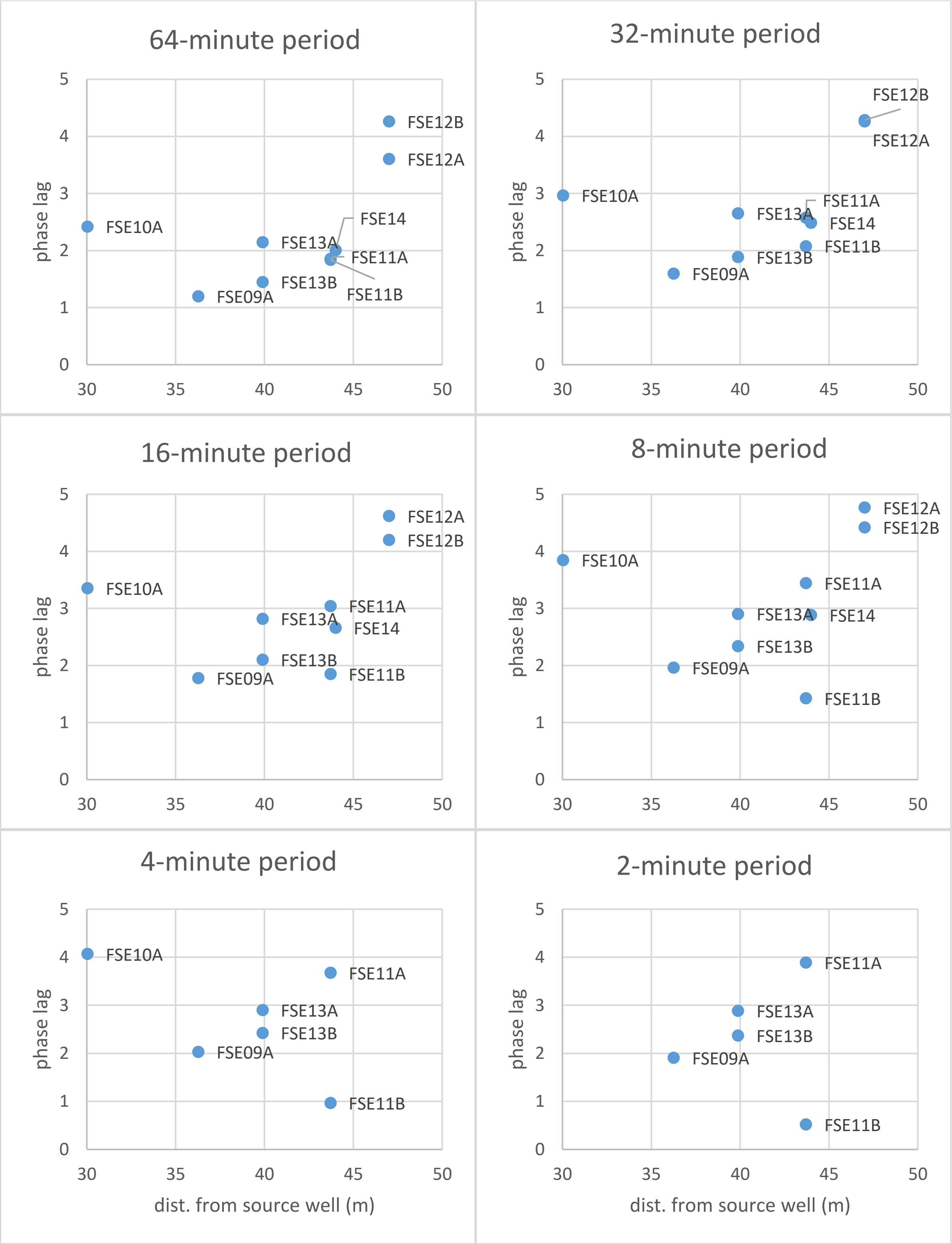

Figure 31. Phase lags vs distance from pumping well. 64-minute period (top left) through 2-minute period (bottom right). Larger values represent greater lag time.

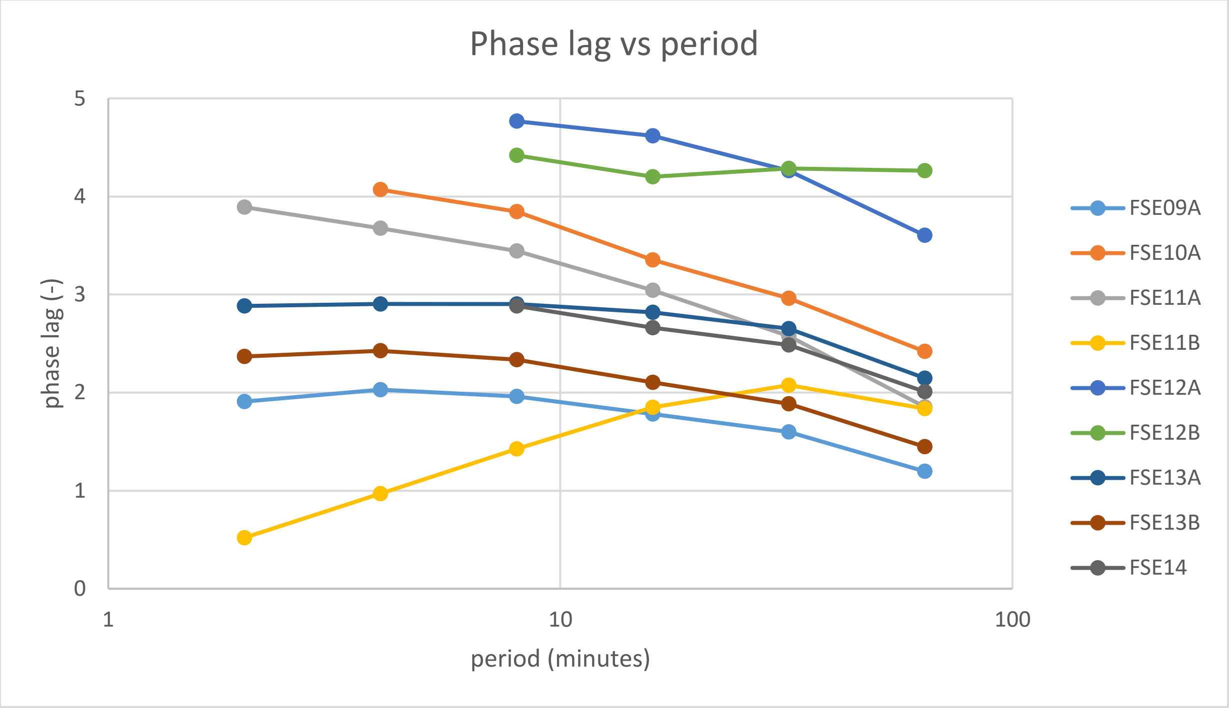

Figure 32. Observation phase lags as a function of period.

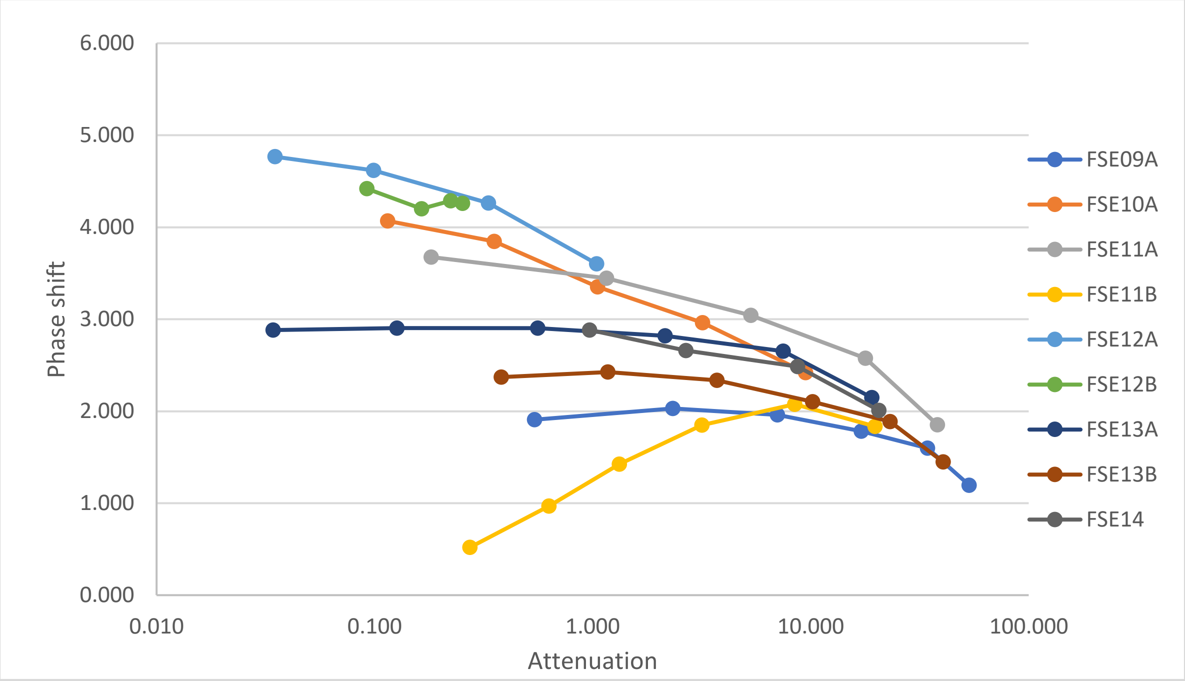

Figure 33. Semi-log characteristic curves, after Ahn and Horne (2011). Phase shift is observation phase minus injection phase and corrected for phase wrap, and attenuation is observation amplitude divided by injection amplitude (table 9 and table 6, respectively). Non-qualifying responses (orange cells in tables) are not included.

Parameter Estimation

Parameter estimates are obtained using optimization techniques native to Matlab®. The objective function computes equations 22 and 23, which are the amplitude and phase components of equation 21, and compares those to the FFT amplitude and phase of the field data to give the total percent error from both components. Parameters which minimize this total error are found using the global minimum search algorithm *patternsearch* in Matlab®. This algorithm proved very effective at finding the global minimum rather than a local minimum, regardless of initial guess values used. This is an important feature because the objective function contains local minima that result in low error, but give parameter estimates that are orders of magnitude off from those of the global minimum (**Figure 34 - Figure 36**).

Diffusivity and storativity are the two independent variables, so it is helpful to calculate the objective function for a range of these variables and plot the result to visualize its possible solutions. Looking at the function's surface, one can see many local minima (**Figure 36**). Because optimization algorithms are usually gradient based, the solution may converge to one of these points unless the initial guess values start the solver in the correct region. Solutions given by optimization must therefore be checked either by examining the objective function or comparing the modeled head response to field data to ensure that the given parameters are reasonable. The Matlab® global search method described above helped avoid this problem, but solutions were still double checked for certainty. Another potential issue is that the objective surface is relatively flat over a wide range of D near the global minimum (**Figure 34**). After adjusting the plot so that the z-axis is logarithmic, the exact global minimum becomes clearer (**Figure 35**). The solver's stopping criteria must be fine enough to be sensitive to these small changes in gradient to find the true minimum.

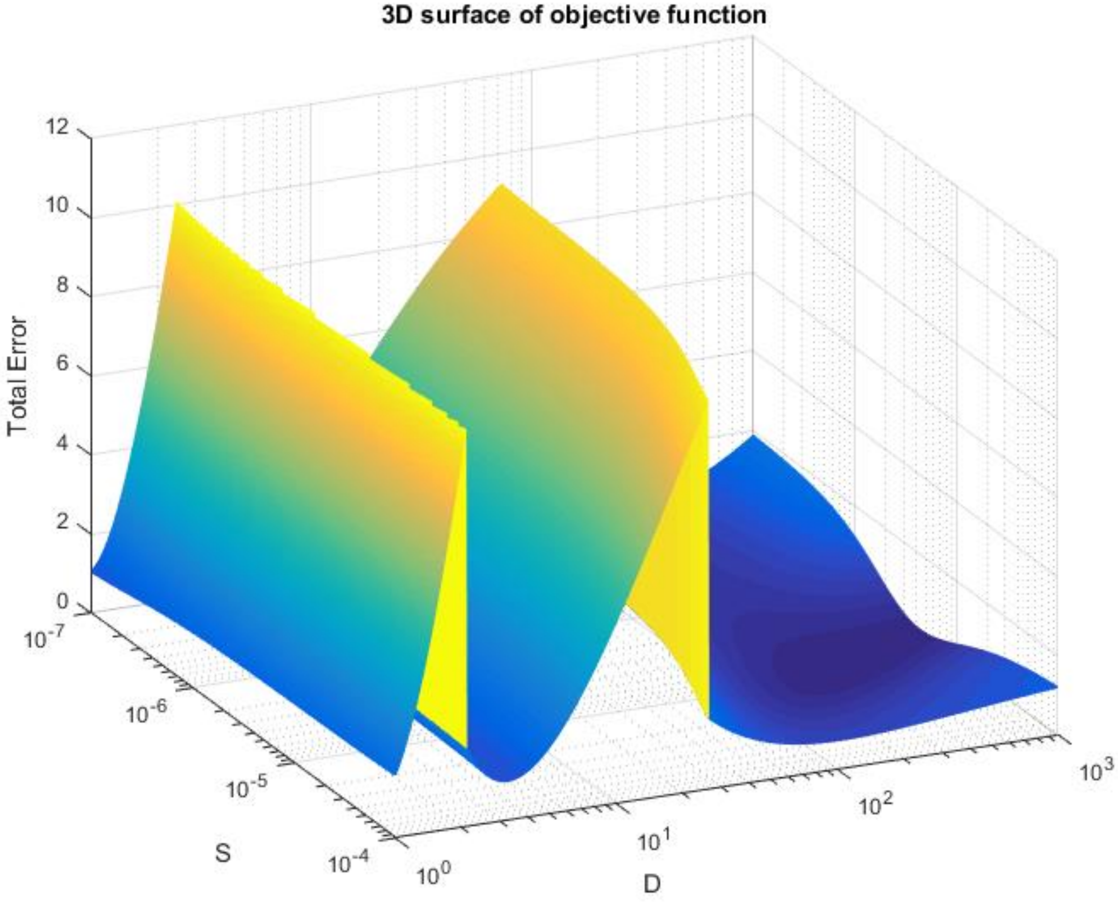

Figure 34. Semi-log 3D plot of objective function for a range of diffusivity (D) and storativity (S) values. From FSE 9, 32-minute test. Total error is normalized phase error plus normalized amplitude error.

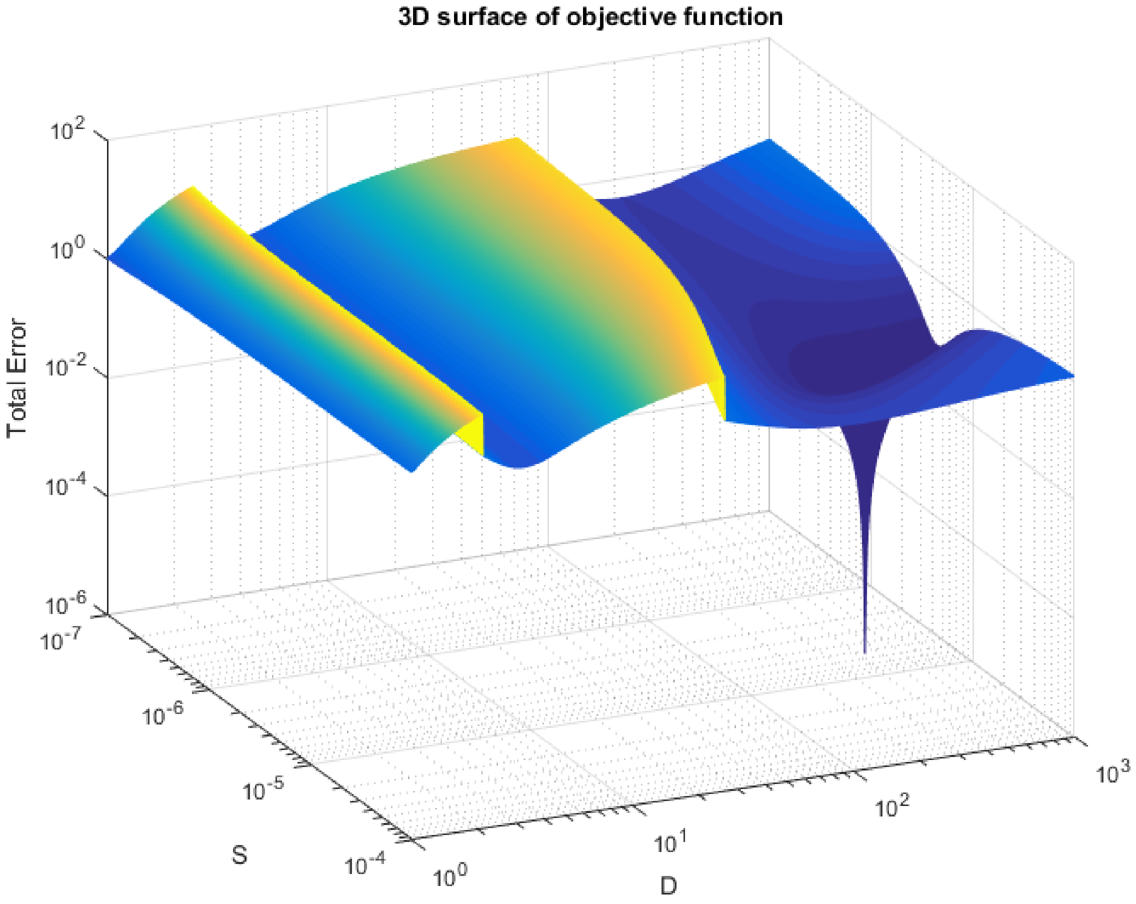

Figure 35. Same as figure above, except z-axis is logarithmic to show global minimum

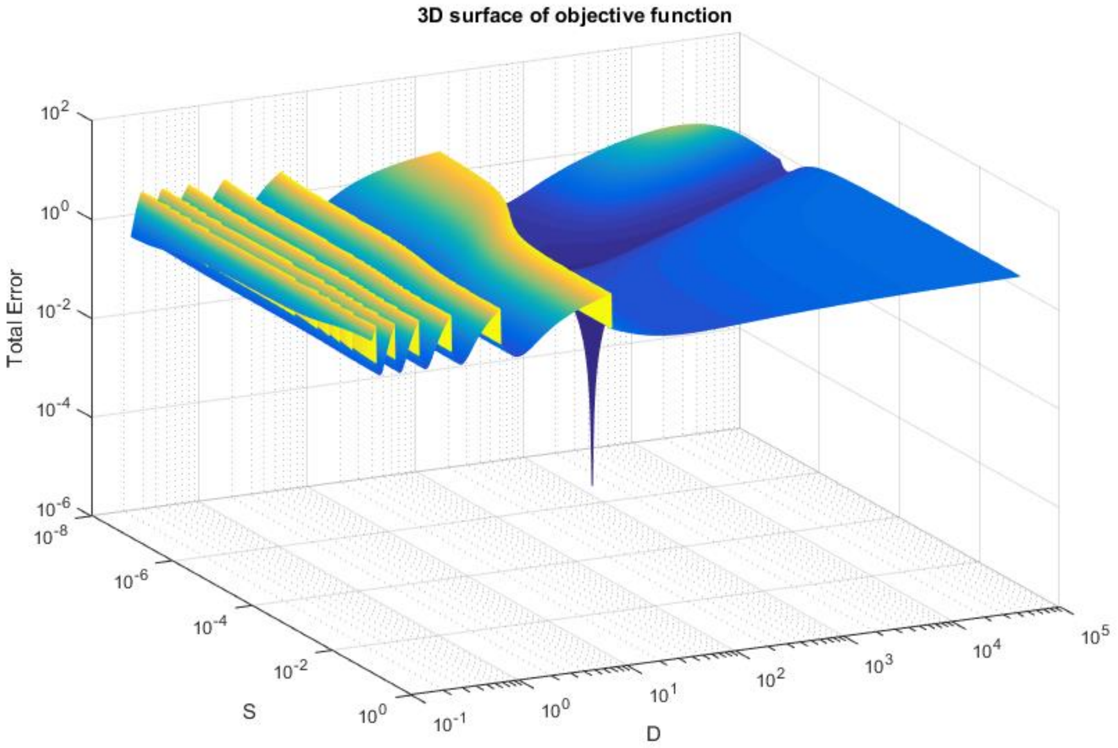

Figure 36. Same as above, except larger range of D and S

Parameter estimates obtained from the optimization procedure described above are summarized in **Table 10**. Unlike phase lag or amplitude alone, the solutions that yield parameter estimates incorporate phase lag and amplitude, as well as radial distance from the pumping well and wellbore storage coefficients, making for more useful comparisons. Each parameter is plotted against period length in **Figure 37** through **Figure 39**, which is an effective way to visually compare the responses and the overall trends with period length. Recalling the phase lag and amplitude results, the strongest responses (large amplitude and small phase lag) were typically FSE09a, FSE11b, and FSE13b, and the weakest were FSE10a, FSE12a, and FSE12b. These same relative response strengths correlate well with diffusivity (**Figure 37**), as expected based on previous works (Guiltinan and Becker, 2015; Renner and Messar, 2006). FSE09a, FSE13b, and FSE11b have the largest diffusivity estimates, with FSE11b increasing sharply for the shorter period tests. FSE10a, FSE12a, and FSE12b have the smallest diffusivities, and FSE11a, FSE13a, and FSE14 plot in the middle. The range between highest and lowest diffusivity at a given period length is always less than two orders of magnitude, except for the 2 and 4-minute tests for which FSE11b about three orders of magnitude greater than the lowest diffusivity measured.

The relative differences between wells are greater for storativity than for transmissivity; diffusivity appears to correlate well with the inverse of storativity (**Figure 38**). The correlation with transmissivity does not appear to be quite as strong (**Figure 39**), suggesting that storativity may be the more significant parameter controlling the diffusivity ratio, *T/S*.

Table 10. Parameter Estimates

Period (mins)	**FSE09A**			**FSE10A**			**FSE11A**		
	D	S	T	D	S	T	D	S	T
2	1.9E+03	4.3E-05	8.2E-02						
4	1.6E+03	1.1E-05	1.8E-02	1.1E+02	6.2E-04	7.0E-02	2.4E+02	2.1E-04	4.9E-02
8	1.6E+03	4.0E-06	6.2E-03	6.2E+01	3.8E-04	2.3E-02	1.7E+02	5.2E-05	8.6E-03
16	1.3E+03	2.7E-06	3.6E-03	3.4E+01	2.6E-04	8.7E-03	1.4E+02	1.3E-05	1.8E-03
32	8.7E+02	2.9E-06	2.5E-03	2.2E+01	1.7E-04	3.6E-03	1.3E+02	8.1E-06	1.0E-03
64	6.4E+02	4.3E-06	2.8E-03	1.8E+01	1.3E-04	2.3E-03	1.2E+02	1.1E-05	1.4E-03
	FSE11B			**FSE12A**			**FSE12B**		
2	1.0E+05	1.0E-05	9.9E-01						
4	5.9E+03	3.4E-05	2.0E-01						
8	1.1E+03	5.0E-05	5.3E-02	1.1E+02	1.6E-03	1.8E-01	1.2E+02	6.1E-04	7.6E-02
16	3.1E+02	4.5E-05	1.4E-02	5.8E+01	1.1E-03	6.6E-02	6.1E+01	6.9E-04	4.2E-02
32	1.5E+02	3.0E-05	4.4E-03	3.0E+01	6.9E-04	2.0E-02	3.0E+01	1.0E-03	3.0E-02
64	1.0E+02	2.4E-05	2.5E-03	1.5E+01	4.4E-04	6.7E-03	1.4E+01	1.8E-03	2.6E-02
	FSE13A			**FSE13B**			**FSE14**		
2	4.2E+02	6.5E-04	2.7E-01	1.2E+03	5.3E-05	6.5E-02			
4	2.2E+02	3.5E-04	7.7E-02	7.7E+02	2.7E-05	2.1E-02			
8	1.3E+02	1.5E-04	2.0E-02	6.2E+02	1.1E-05	6.9E-03	2.4E+02	5.6E-05	1.3E-02
16	8.1E+01	7.7E-05	6.3E-03	5.2E+02	6.8E-06	3.6E-03	1.6E+02	4.1E-05	6.5E-03
32	5.7E+01	4.1E-05	2.3E-03	3.8E+02	6.0E-06	2.3E-03	1.2E+02	2.2E-05	2.6E-03
64	4.7E+01	3.6E-05	1.7E-03	3.0E+02	8.0E-06	2.4E-03	9.9E+01	2.0E-05	2.0E-03

Diffusivity (m^2/min) is highlighted blue, storativity (dimensionless) yellow, and transmissivity (m^2/min) green, for clarity. Empty boxes indicate that the response did not pass criteria.

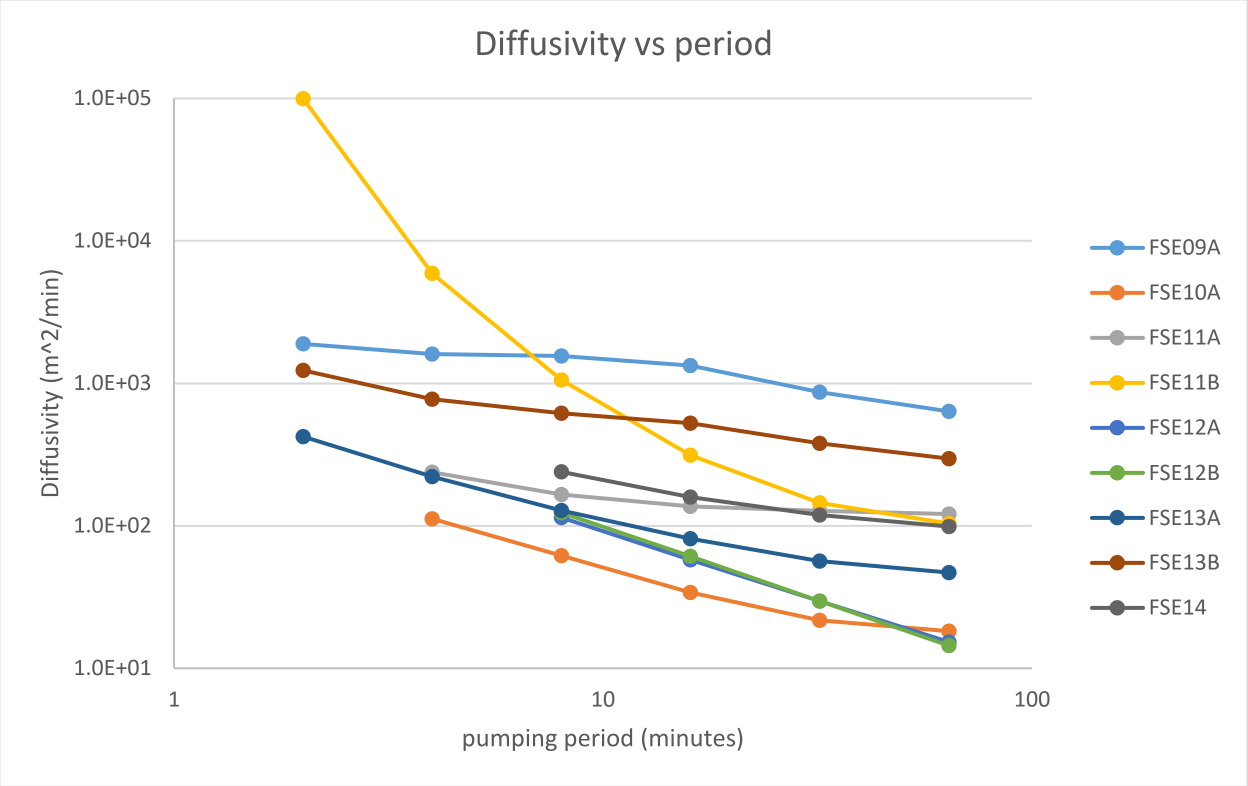

Figure 37. Diffusivity plotted as a function of pumping period. Both axes are logarithmic.

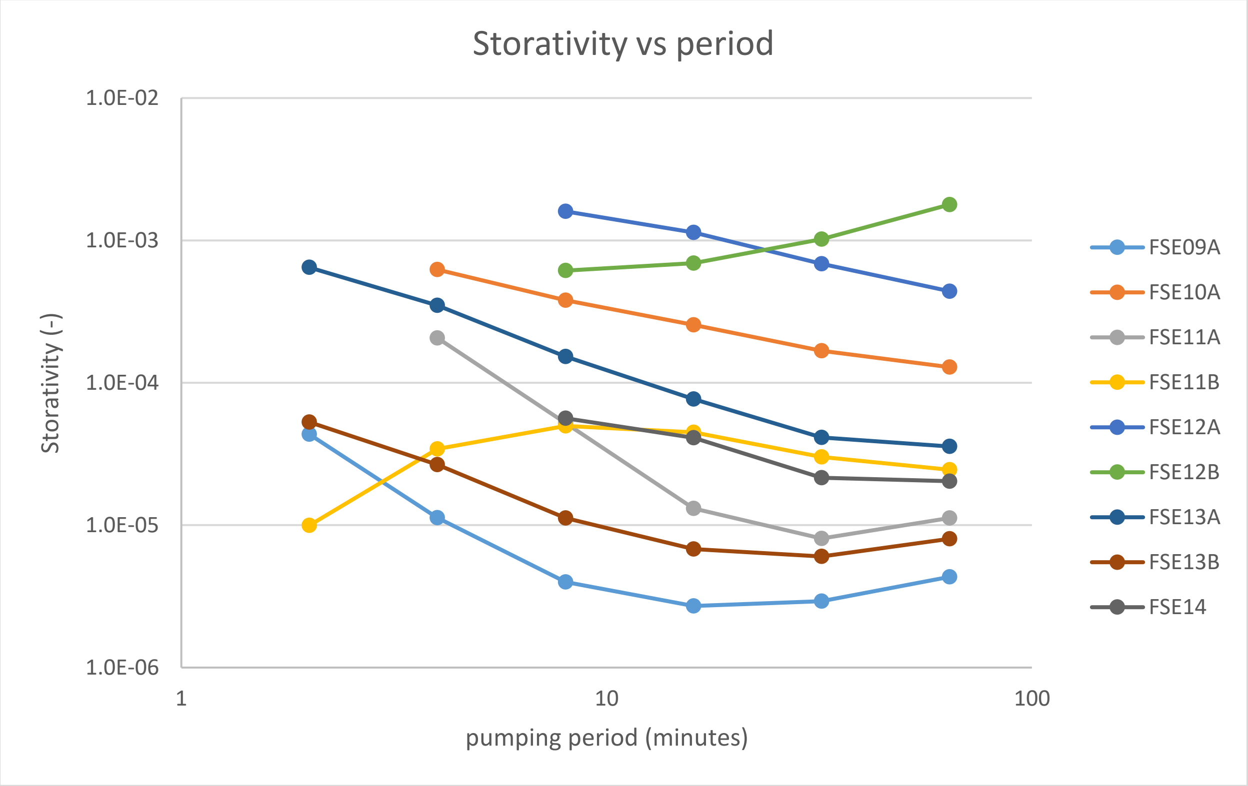

Figure 38. Storativity plotted as a function of period. Both axes are logarithmic.

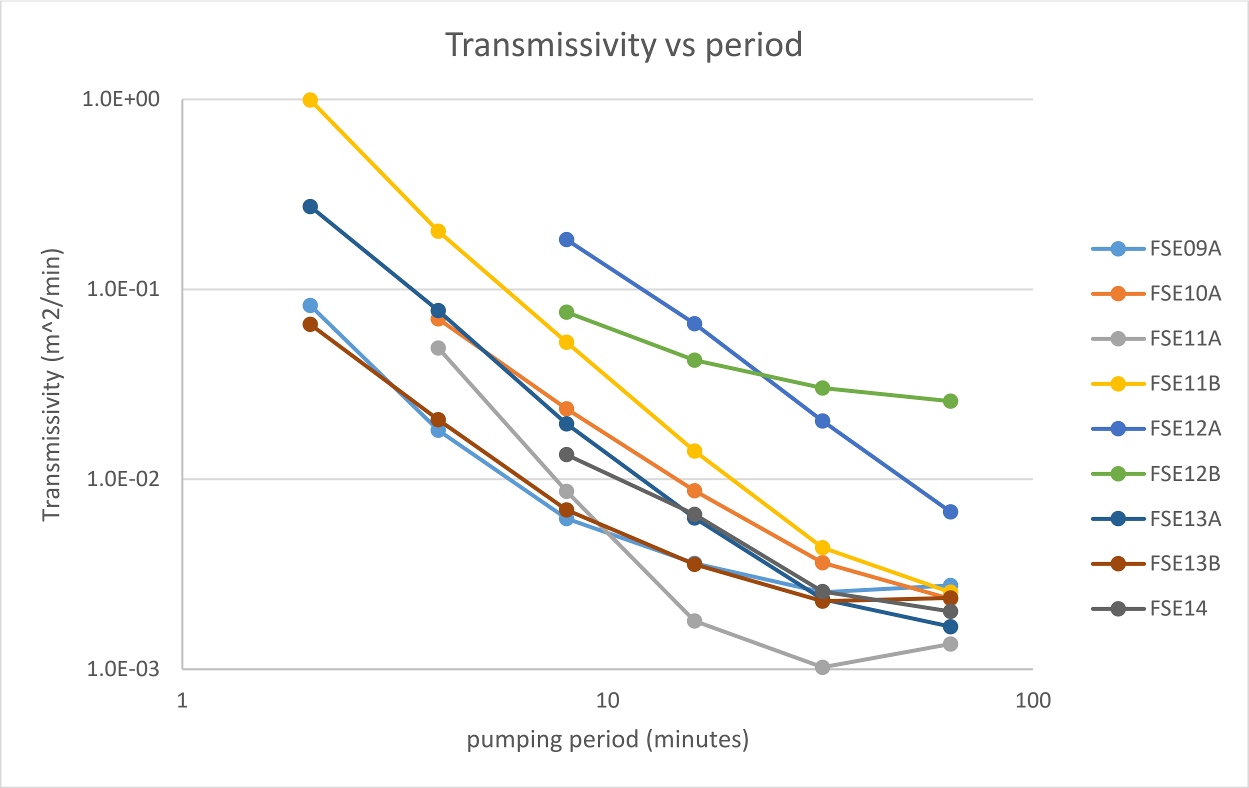

Figure 39. Transmissivity plotted as a function of period. Both axes are logarithmic.

CHAPTER 6

DISCUSSION

Discussion of method

This study adds to the growing body of work utilizing a periodic hydraulic stress for aquifer characterization and supports the idea that this type of testing is well suited for fractured rock or other low storativity aquifers, for which pressure diffuses outward quickly. In our tests borehole storage significantly affected responses, causing an apparent phase delay and amplitude decrease of head in the borehole compared to head in the fracture. The low storativity inherent in fractured rock aquifers probably leads to the significance of borehole storage. The small, repeated hydraulic responses from short period tests necessary to keep the radius of influence within the scale of the well field could be detected and analyzed with more confidence than the transient data of a conventional pumping test. Frequency domain analysis proved to be an effective approach to acquiring the information from these responses, but some background understanding of the Fourier transform is needed to avoid errors.

Most significant of the possible errors is “phase wrap”, or a phase lag of greater than 2π between pumping and observation wells, which is discussed thoroughly in (Cardiff and Sayler, 2016). This can occur because the time domain signal is approximated by a sum of sinusoids in the frequency domain, which do not reflect the starting point of the time signal. Hence a greatly shifted sinusoid with a phase value of 9π would have a computed phase of either $\pm\pi$. The problem arose for several phase lag calculations here, not because phase lags were greater than 2π, but because the observation well phase was ahead of the pumping phase, as given by the FFT. This is clearly not feasible so the problem was easily detected, and subtracting 2π gave the appropriate phase lag value. It serves as an example of the need for extra care to be taken before interpreting data from periodic tests.

Analyzing responses in the frequency domain enabled the use of even the most obscure time domain signals. ***Figure 40*** is an example of an obscure time domain signal that was easily visible in the frequency domain. After linear detrending (top), there is no noticeable periodic component; after clipping and filtering (middle), some periodicity is noticeable, though analyzing this time domain response would through curve fitting would be difficult; but in the frequency domain (bottom), the imposed pumping frequency (1/2 minute) is clear. Non-qualifying responses failed more often due to the limit of the transducer resolution than the quality of the signal (i.e. signal-to-noise ratio). The time domain data used here only consisted of 4 to 6 periods of oscillation. Increasing the number of periods would enhance the frequency response and could further improve the excellent signal to noise ratio. Advancements in transducer technology coupled with frequency domain analysis could allow the use of ever smaller responses, which has implications for investigating finer scale heterogeneity and for using natural periodic fluxes to investigate aquifers at the basin scale.

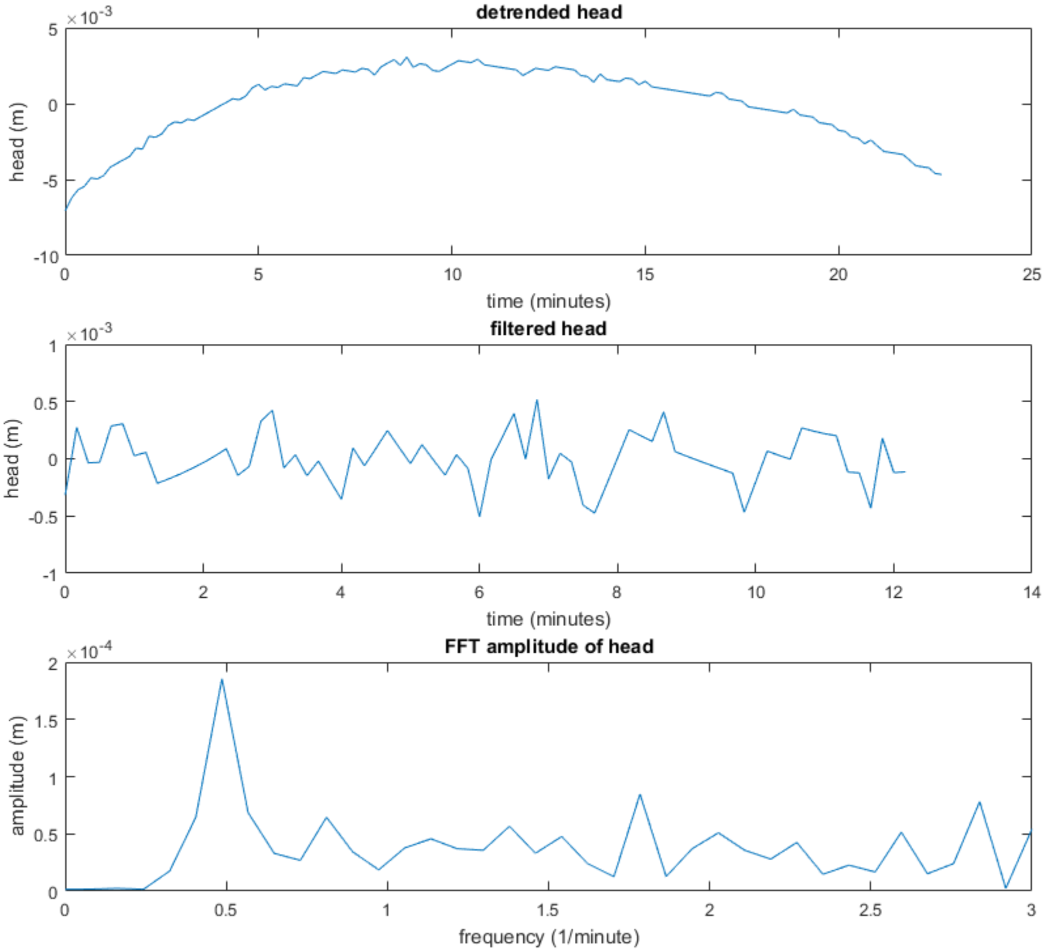

Figure 40. FSE13a, 2-minute period response. Top is head in the time domain after linear detrending, middle is time domain of filtered head after high pass filter, bottom is filtered head amplitude in frequency domain.

Period dependence

Diffusivity estimates from Guiltinan and Becker (2015), which were measured in a single bedding plane fracture, decreased as period length increased, described by a negative power law relationship (Guiltinan and Becker, 2015). Diffusivities obtained here were also described by a negative power law function (**Figure 41**). Some responses fit this type of curve better than others, with r-squared values ranging from 0.85 to 1, but all followed the same general trend of sharply decreasing diffusivity with increasing period at shorter periods, and then becoming horizontally asymptotic at longer periods. The power law relationship seen by Guiltinan and Becker (2015) tended to be more robust than the relationship seen here. One explanation for this may be that their site was a single bedding plane fracture, while this site was a more complex fracture network with higher heterogeneity. The mean of all diffusivity estimates was calculated for each test. The mean values followed the power law relationship with period. The relationship was more robust when using the geometric mean, because the very large diffusivities from FSE11b do not weigh as heavily as they do for the arithmetic mean (last two plots, **Figure 41**). These trends are generally in agreement with those observed in previous periodic field tests in fractured rock (**Table 1**). Suggested mechanisms for these trends are discussed below.

Guiltinan and Becker (2015) and Renner and Messar (2006) described the mechanism for this relationship conceptually, positing that as period length increases water has more time to fill dead end or backbone fractures that contribute to storage but not flow (Guiltinan and Becker, 2015; Renner and Messar, 2006). This would increase storativity while leaving transmissivity unchanged, thereby decreasing diffusivity. Rabinovich et al. (2015) explored the period dependency using a simple model with a low conductivity spherical inclusion, which showed that as period decreases, hydraulic gradient outside the inclusion increases more than inside the inclusion (Rabinovich et al., 2015). This tendency for flow to favor higher conductivity regions at shorter periods led to higher effective conductivity estimates. Both explanations arrive at essentially the same conclusion, though the latter focuses on the effect on transmissivity (conductivity) while the former focuses on the effect on storativity.

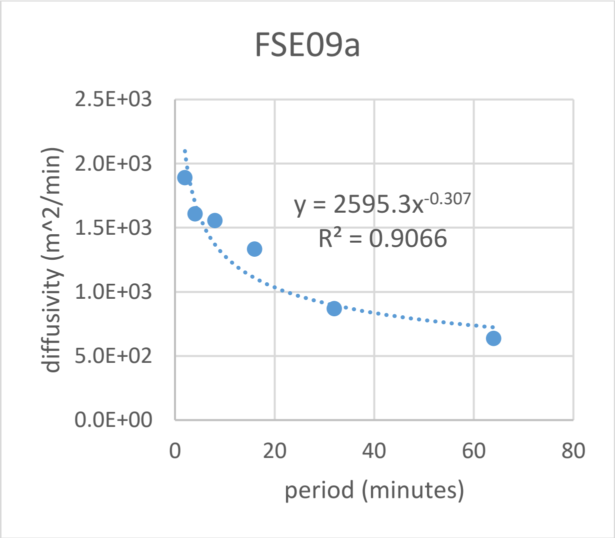
FSE09a
2.5E+03
2.0E+03
1.5E+03
1.0E+03
5.0E+02
0.0E+00
diffusivity (m^2/min)
y = 2595.3x^-0.307
R² = 0.9066
0
20
40
60
80
period (minutes)

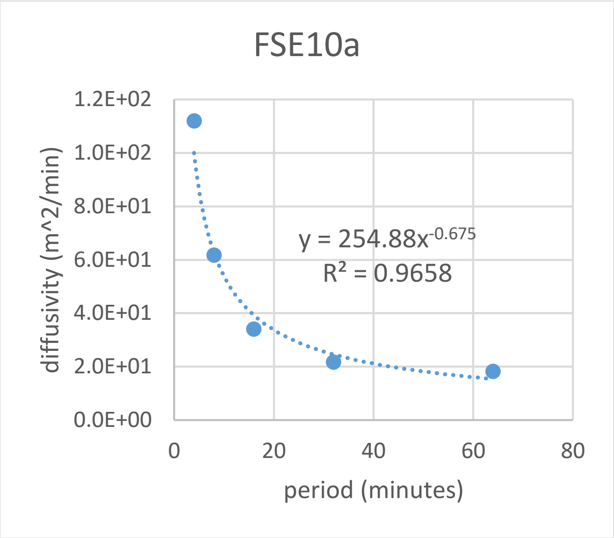
FSE10a
1.2E+02
1.0E+02
8.0E+01
6.0E+01
4.0E+01
2.0E+01
0.0E+00
diffusivity (m^2/min)
y = 254.88x^-0.675
R² = 0.9658
0
20
40
60
80
period (minutes)

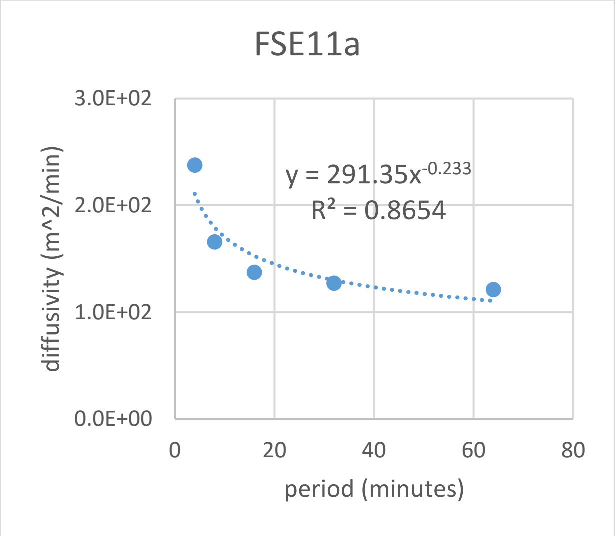
FSE11a
3.0E+02
2.0E+02
1.0E+02
0.0E+00
diffusivity (m^2/min)
y = 291.35x^-0.233
R² = 0.8654
0
20
40
60
80
period (minutes)

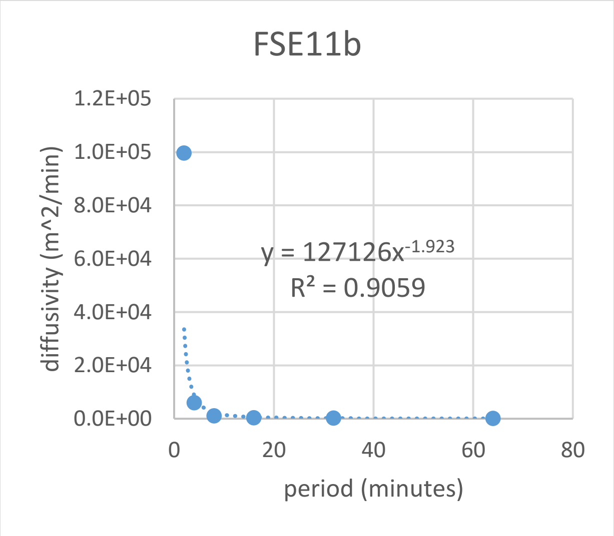
FSE11b
1.2E+05
1.0E+05
8.0E+04
6.0E+04
4.0E+04
2.0E+04
0.0E+00
diffusivity (m^2/min)
y = 127126x^-1.923
R² = 0.9059
0
20
40
60
80
period (minutes)

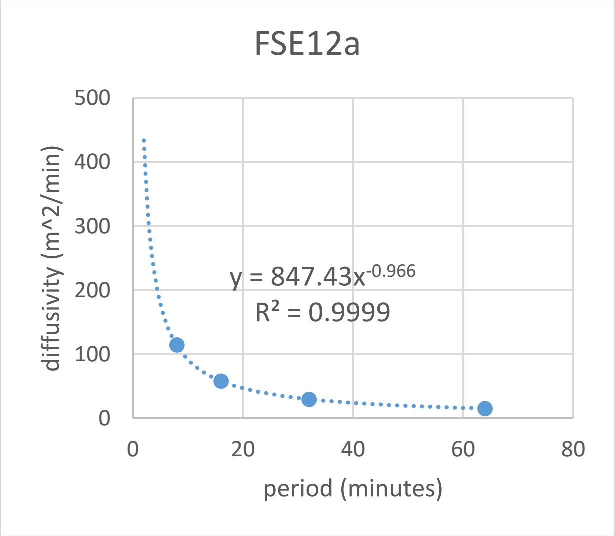
FSE12a
500
400
300
200
100
0
diffusivity (m^2/min)
y = 847.43x^-0.966
R² = 0.9999
0
20
40
60
80
period (minutes)

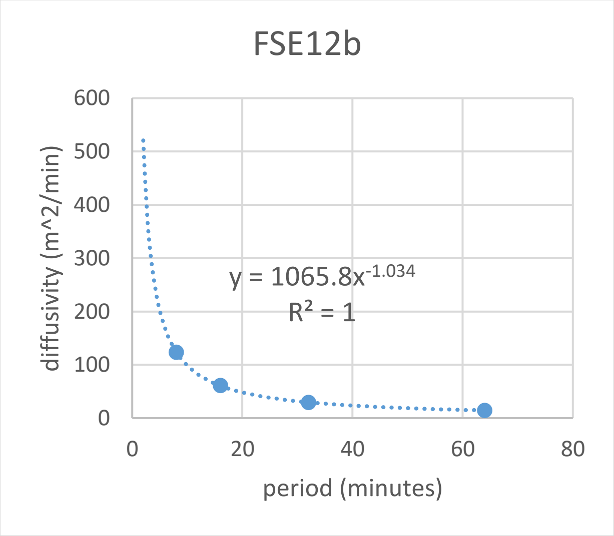
FSE12b
600
500
400
300
200
100
0
diffusivity (m^2/min)
y = 1065.8x^-1.034
R² = 1
0
20
40
60
80
period (minutes)

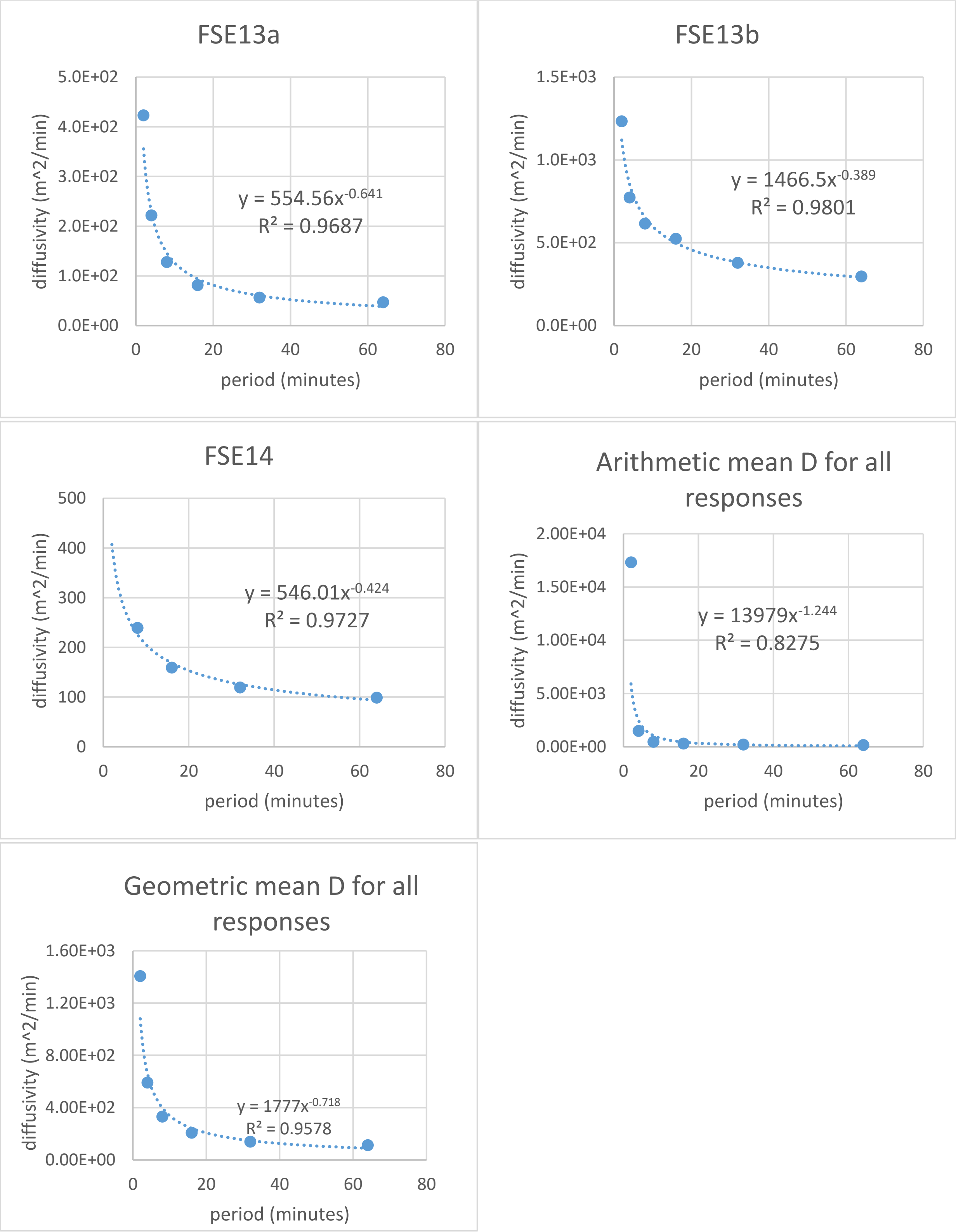

Figure 41. Diffusivity versus period for each response and power function trendline of best fit. Second-to-last row, right is the mean of all observation diffusivities for each period. Using geometric mean resulted in robust power law relationship (bottom left).

Here, the period dependence appears to be driven by changes in transmissivity while changes in storativity affect the differences between observation wells. This is apparent in **Figure 38** and **Figure 39**, where storativity estimates vary greatly between different wells and to a lesser degree between different period lengths, while transmissivity estimates vary greatly between period length and to a lesser degree between wells. Similarly, storativity was more variable than transmissivity for different well pairings, shown in Figures 12 and 13 from Guiltinan and Becker (2015). However, their storativity estimates increased with period, whereas storativity estimates from this experiment mostly decreased with period (**Figure 38**). Both here and in their study, differences in storativity appear to drive the different diffusivity estimates for observation wells, which reflects connection among wells. Differences in transmissivity follow the inherent period relationship, either caused by the tendency for flow to prefer higher conductivity regions at shorter periods, shown by Rabinovich et al. (2015) or due to hydromechanical effects of shorter periods causing fracture dilation, thus increasing aperture and conductivity, as suggested by Guiltinan and Becker (2015) or a combination of the two.

Calculating the mean of all responses of each period length for T and S shows that transmissivity follows the negative power law relationship and storativity does not (**Figure 42**). Using the geometric mean instead of arithmetic mean, which is better suited to representing differences of several orders-of-magnitude in parameter estimates did not significantly change the power law relationship for transmissivity, but did improve the relationship for storativity (**Figure 43**). The power law relationship of transmissivity is consistent with the findings of the low conductivity inclusion model presented in Rabinovich et al. (2015), and their effective conductivity versus period plot in Figure 10 is similar to mean transmissivity in **Figure 42** (Rabinovich et al., 2015).

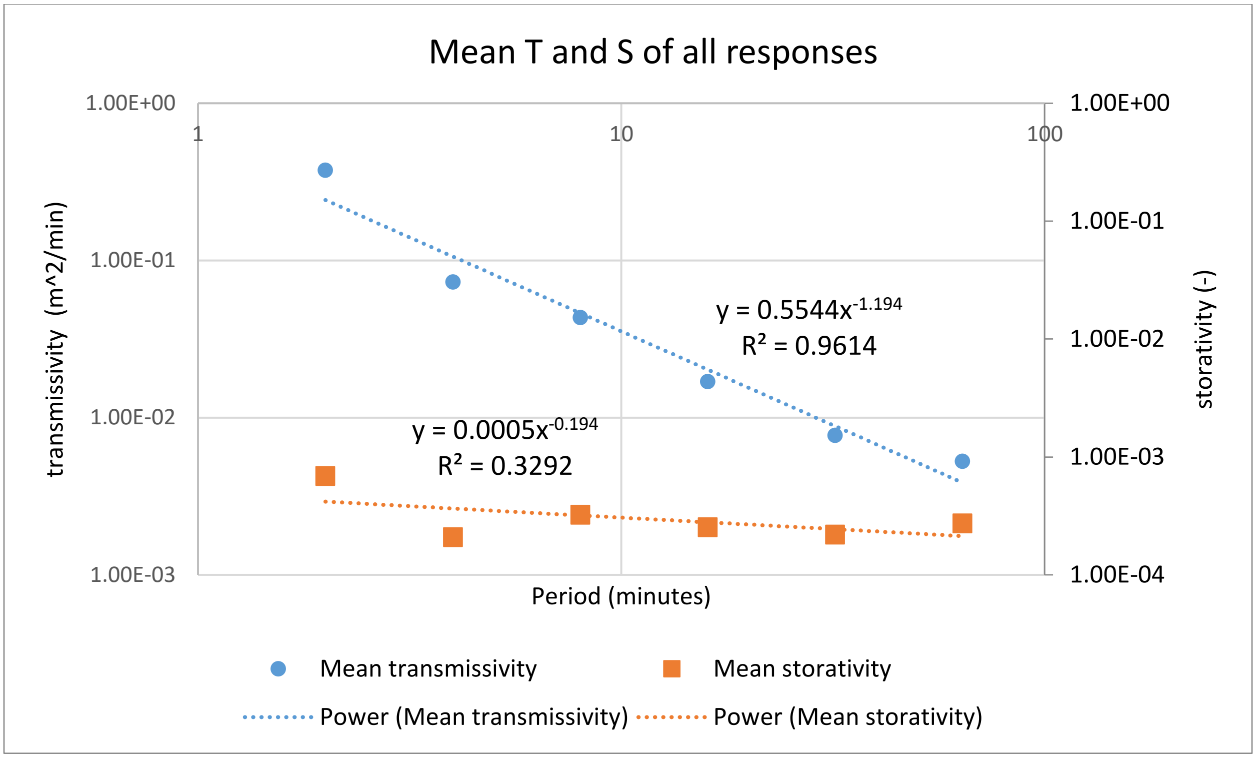

Figure 42. Mean of all responses at each period length.

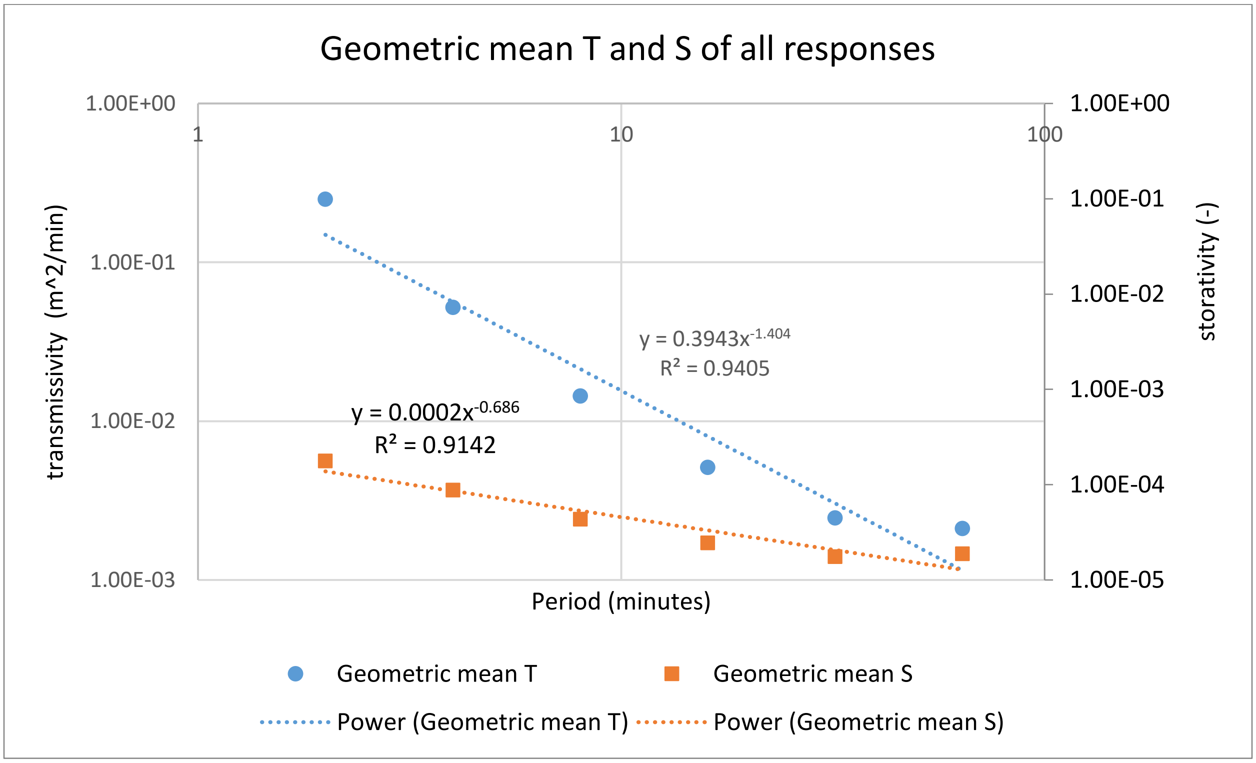

Figure 43. Geometric mean of all responses at each period length.

Guiltinan and Becker (2015) questioned the role of hydromechanical fracture dilation on transmissivity estimates, pointing to the known non-linear relationships between changes in effective stress and aperture. It is intuitive that as period decreases there is less time for water to move into the formation, resulting in a greater hydraulic force to reduce effective stress and cause a fracture to open. Transmissivity is related to fracture aperture by the cubic law, so a small change in aperture could greatly affect transmissivity (T), according to

$$T = \frac{b^3 \rho g}{12\mu} \tag{25}$$

where *b* is the fracture aperture, g is gravity, ρ is water density, and μ is viscosity. While there have been numerous cases where the cubic law does not hold, it can still be applied to a wide range of fractures (Rutqvist and Stephansson, 2003).

Experiments conducted in conjunction with those presented here (in the same well field, though not simultaneously) measured strain along a fiber optic cable caused by periodic fracture dilation. Distributed acoustic sensing (DAS) technology measured the strain along the cable, which was coupled to the borehole wall across the fracture opening using an inverted plastic liner (Becker et al., 2016). A full discussion of the geomechanical response to hydraulic pressure changes is beyond the scope of this work. But preliminary results describing fracture aperture from this study can shed some light on the hydromechanical effect on transmissivity. Rearranging equation 24 to solve for aperture, *b*, gives

$$b = \sqrt[3]{\frac{12T\mu}{\rho g}} \tag{26}$$

The smallest estimated transmissivity for FSE10a is 2.3e-3 m^2/min, for the 64-minute period test (**Table 10**), which corresponds to an aperture of about 0.36 mm according to the cubic law. The greatest measured fracture opening/closing amplitude at the major transmissive fracture in FSE10 was about 1 nanometer (Becker et al., 2017). Adding 1 nm to 0.36 mm is as insignificant as it sounds in terms of transmissivity, resulting in a change of less than 0.004%, whereas *T* varies by more than an order of magnitude in parameter estimation from longest to shortest period (**Table 10**). To create an effective fracture transmissivity of the greatest viable estimate for FSE10a, 7.0e-2 m^2/min, the fracture would need to dilate by 0.76 mm. Dilation would be larger at the source well where changes in effective stress are much greater, so the possibility of aperture changes of the required size cannot be ruled out based on these observation well measurements alone. Further work using the strain sensing capabilities of DAS and other devices that measure aperture would better constrain this. It is interesting to note that the change in fracture aperture (expressed by transmissivity) versus period length curve (**Figure 44**) has the same shape as Rabinovich et al.'s curve showing change in gradient versus period length, their proposed driver of the increase in conductivity with decreasing period (Rabinovich et al., 2015). Thus, if both are contributing factors to the period dependency it may be difficult to distinguish the effect of one from the other.

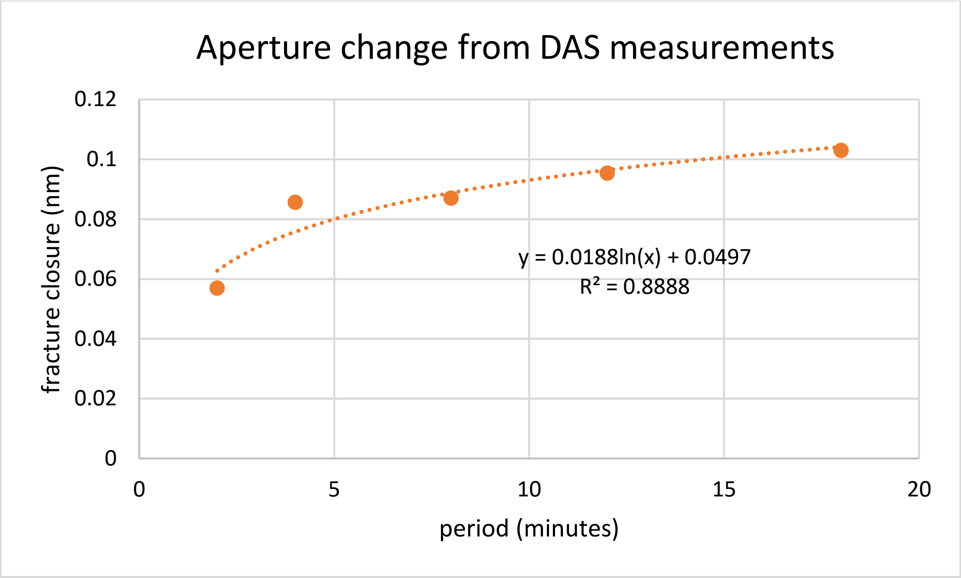

Figure 44. Aperture change for FSE10 (nanometers) from DAS measurements. For these experiments, injection was a square wave (not sinusoidal) and period lengths were shorter (2, 4, 8, 12, 18 minutes). From Becker et al. (2017)

Formation Information

The wide variation in parameter estimates is proof of the aquifer heterogeneity. A homogenous aquifer would yield identical results for all observation wells. It also suggests that the period lengths of induced pumping were adequately sensitive to the localized scale of the well field. Because penetration radius is proportional to period length, shorter periods provide information from nearer in vicinity to the pumping well whereas longer periods are more diffuse, as shown by the sensitivity maps in Cardiff et al. (2013). Diffusivity is assumed to best describe hydraulic connection between wells, based on conclusions of previous work (Guiltinan and Becker, 2015; Knudby and Carrera, 2006). The diffusivity estimates obtained here reflect hydraulic connections that are consistent with past characterizations at this site. The main difference, however, is that the fracture zones A and B seem to be more connected than previously assumed. This is probably because pumping tests were acquiring information beyond the scale of the well field, where the upper and lower zones may be disconnected. Near the well field this appears not to be the case, as strong connections were measured between the pumping interval, FSE6a, and the lower zone in FSE11b and FSE13b.

Interestingly, some of the highest estimated transmissivities were for FSE12a and b, which were the least connected observation points in terms of diffusivity, phase lag, and attenuation. Transmissivity alone does not reflect connection or accurately predict transport of contaminants, heat, tracers, or pressure. Instead, the ratio of transmissivity to storativity (diffusivity) is more useful, as Knudby and Carrera found that apparent diffusivity correlated well with early tracer arrival time (Knudby and Carrera, 2006). The utility of diffusivity as a predictor of hydraulic connection may be best explained by describing flow as being pipe-like, where higher diffusivity represents more pipe-like flow. For example, imagine two pipes, one filled with sand and the other empty, that have the same transmissivity. For this to be true, the sand filled pipe would have a much larger diameter than the open pipe and its storativity would therefore be larger, so diffusivity would be larger in the small pipe than the large, sand filled pipe. Although both pipes could transmit equal flow, velocity would be greater in the small, open pipe.

The marked deviation at short period tests of FSE11b from expected trends with period length and from other observation points may be an example of detecting a highly-channelized, or more pipe-like flow path. Diffusivity for FSE11b rose more rapidly than other observation points. A possible explanation for this behavior is that there exists a highly-channelized conduit between the pumping well and FSE11b. Because the short period tests are sensitive to nearby features and the most conductive heterogeneities, this conduit was the dominant flow path. As the testing period increased, radius of interrogation expanded and pressure gradients became more diffuse, so this conduit was less weighted in the sensing of the aquifer. Had there been a larger scale fracture zone of connection to FSE11b, its estimated diffusivity would not have decreased relative to other wells. Instead, it changes greatly relative to other wells as period changes, suggesting that it is a very localized heterogeneity.

Another outlier response is FSE12b, for which amplitude decreases and phase lag increases relative to FSE12a from the 16 to 64-minute period test. Its amplitude normalized by total pumped volume also decreased with increasing period, an atypical trend. However, its estimated diffusivity does not exhibit any marked trend changes. The increase in phase lag and decrease in amplitude points intuitively to less connection to the pumping well, though if this were the case one would expect a decrease in estimated diffusivity. Storativity, however, increases for FSE12b, while storativity for most wells decreases. Using the pipe analogy above, this would indicate less pipe-like flow to the well at the larger testing scales (greater period).

Figure 45 is an updated version of conceptual model presented earlier in the site description (**Figure 8**), showing the degree of hydraulic connection to the pumping well based on average estimated diffusivity values for each observation point. It depicts the improved resolution of heterogeneity throughout the well field, though it does not show results based on different periods or sensitive regions. Examining responses to constant rate pumping (**Figure 6**), the early time drawdowns are highly varied, then converge after several hours. Responses from periodic pumping tests, with a maximum period of 64 minutes, are related to these early time drawdowns. These results indicate a three-dimensional network of diverse connectivity, whereas results from constant rate pumping tests lead to a two-dimensional interpretation with well groupings (gray planes; **Figure 45**). While neither interpretation is wrong, each depends on the scale of the problem being investigated. To understand larger scale flow paths or steady state conditions, the 2D zonal interpretation is probably a better representation. To understand inter-well connections and flow paths within the well field, the 3D network interpretation given here is probably more representative.

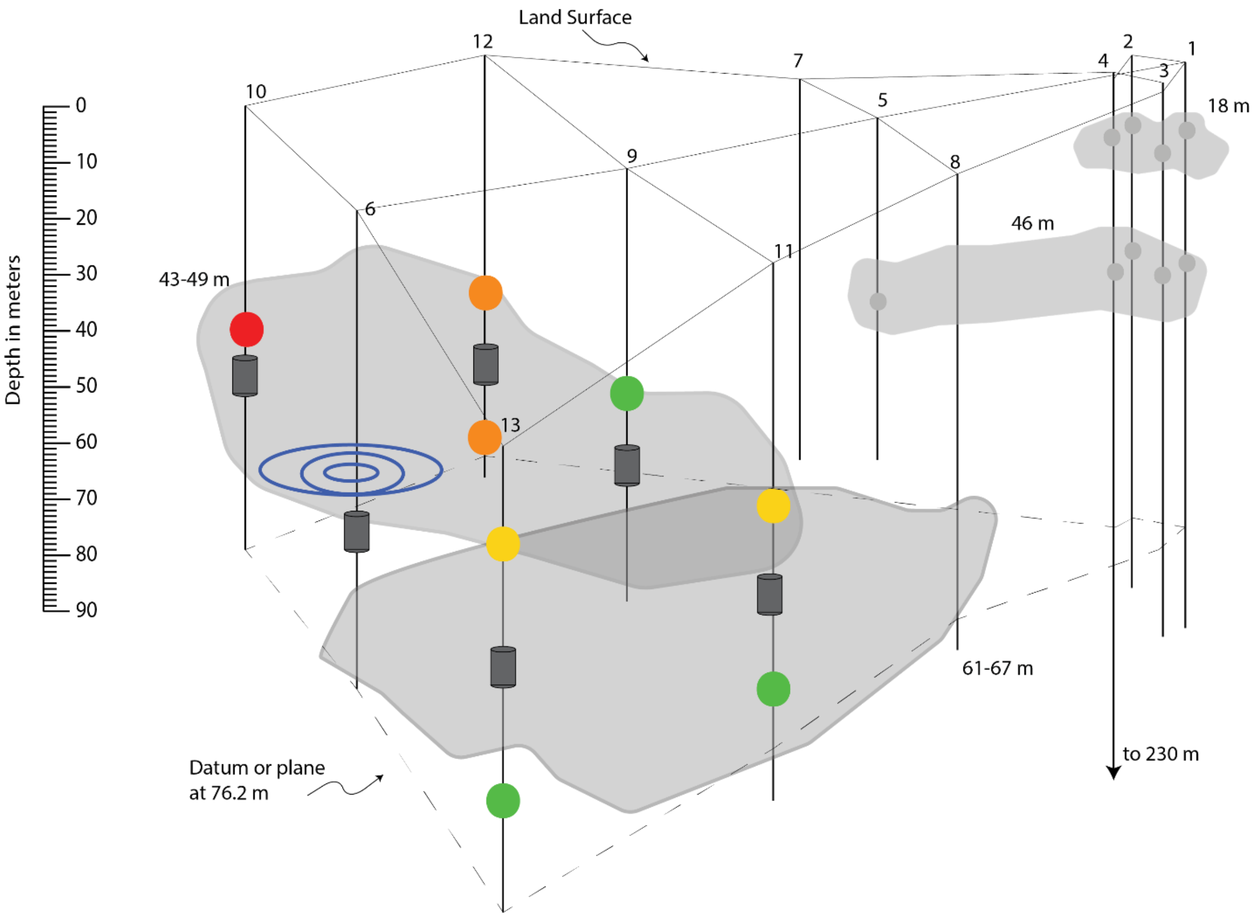

Figure 45. Revised conceptual model with well connection based on diffusivity estimates. Colors represent relative degree of connection with green being the strongest connection, followed by yellow, orange, and red. Dots above packers are A zone, below packers are B zone. FSE14 not shown because it did not have a packer installed. Revised after Tiedeman and Hsieh (2001).

CHAPTER 7

CONCLUSION

Periodic hydraulic tests were performed in a bedrock fracture network at a well-characterized research site in New Hampshire. A dual pump system was used to alternate injection and production at sinusoidal flow rates in the source well. Resulting head oscillations in observation wells were monitored with pressure transducers. An analytic solution for a sinusoidal source term that incorporates observation wellbore storage was derived and arranged to solve for amplitude and phase components. Amplitude and phase of hydraulic responses were then computed through frequency domain analysis. Frequency analysis enabled the use of very small signals, with the resolution of the measuring device often being reached with a strong signal to noise ratio.

Because of the smaller radius of influence and improved sensitivity to local features, the hydraulic parameter estimates better reflected the inter-well heterogeneity than traditional pumping tests. Performing tests at multiple frequencies resulted in a range of interrogated areas that were sensitive to different distances from the pumping well. The diffusivity estimates are the best indication of hydraulic connection to the pumping well, and a qualitative depiction of these average estimates for each well are represented spatially in **Figure 45**. Not reflected in this figure is the sharp increase in diffusivity and hydraulic connection measured in FSE11b for short periods. This could be an indication of a highly-channelized portion of the fracture zone in close vicinity to the pumping well.

The period dependency of hydraulic parameters was investigated by relating measured fracture dilation to transmissivity through the cubic law. Based on fracture aperture changes measured with downhole fiber optic cable in the same well field (Becker et al., 2017), the resulting transmissivity changes via the cubic law are not large enough to account for estimated transmissivity variation found here. These results indicate that the period dependence of transmissivity is not a simply a function of changes in fracture aperture. Additionally, trends of hydraulic parameters with period length vary from well to well, suggesting that period dependency is not a fundamental property of fracture flow. That said, transmissivity did follow trends of the mechanism reported by Rabinovich et al. (2015), while storativity exhibited high variability between observation wells.

The range of oscillation frequencies tested in these experiments corresponds to early time drawdown observed in previous constant rate pumping tests. Drawdown versus time plots from constant rate tests (Figure 2, Tiedeman and Hsieh, 2001) show highly variable responses which then converge at later time. These early time responses were qualitatively similar to estimated diffusivity from periodic tests. The order of hydraulic response was FSE 11, FSE 9, FSE 10, and FSE 12 in the pumping tests, which is consistent with the largest to smallest diffusivities estimated in the periodic tests.

The difference between early and late time trends exemplifies the need to perform tests at a scale useful for the problem being investigated. Late time drawdown data for this well field gives the model of horizontally connected fracture zones developed by Tiedeman and Hsieh (2001), whereas these periodic tests suggest a more complex 3D network of connectivity. Through time, pumping develops an increasingly zonal flow structure in the fracture network. However, the inter-well 3D flow structure is likely of greater significance to heat and solute transport in bedrock systems.

APPENDIX A: STANDARD OPERATING PROCEDURE FOR PERIODIC PUMPING USING VOLTAGE CONTROL

For our experiments, a periodic pressure signal was induced in the pumping well by alternating between withdrawal and injection pumps every half period. This process was automated using an operating mode in the VFD that cycled between pumping rates at a defined time interval. The acceleration parameter was then adjusted to achieve a sinusoidal pumping rate for those tests, though the pumping rate was approximated to a sine wave with an “S” acceleration curve. A more precise sine curve and more user-friendly operation can be achieved using external voltage control, described here.

The pumps used were Grundfos® Redi-Flo 2 model MP1 (Grundfos Pumps Corporation, Downers Grove, IL) and the VFDs controlling them were Baldor® H2 Variable Frequency Drives (Baldor Electric Company, Fort Smith, AR) designed specifically for Grundfos pumps. The VFD controls pump motor speed by varying the input frequency and voltage, and can be adjusted through keypad operation, internal programs and functions, or external controls. One of these external controls is an analog input that accepts a 0-10 VDC signal and matches motor speed per the voltage received. Using a voltage output module (Campbell Scientific® SDM-

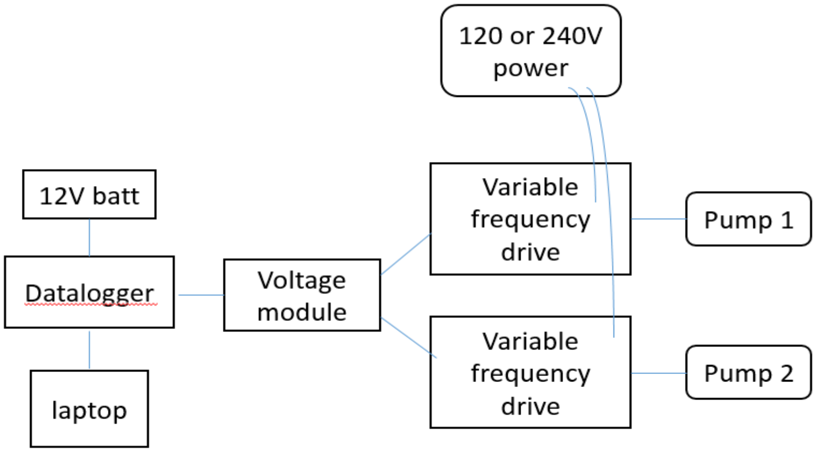

Figure 46. Diagram of control setup

CV04), this 0-10 volt signal can be programmed with the sine function to provide a true sinusoidal variation of pumping rates and period and amplitude values can be easily adjusted. The diagram (**Figure 46**) shows the components of the control system; their wiring is explained next.

Datalogger and Voltage Module Setup

The datalogger (Campbell Scientific® CR800 used here) controls the voltage module by allowing communication with a PC and by outputting 12V power. In many cases a datalogger will be needed for other equipment such as pressure transducers, so its use is not superfluous. Five wires connect the voltage module to the datalogger (**Figure 47**, **Figure 48**). The first connection is 12V to 12V, then ground, C1 to C1, C2 to C2, and C3 to C3.

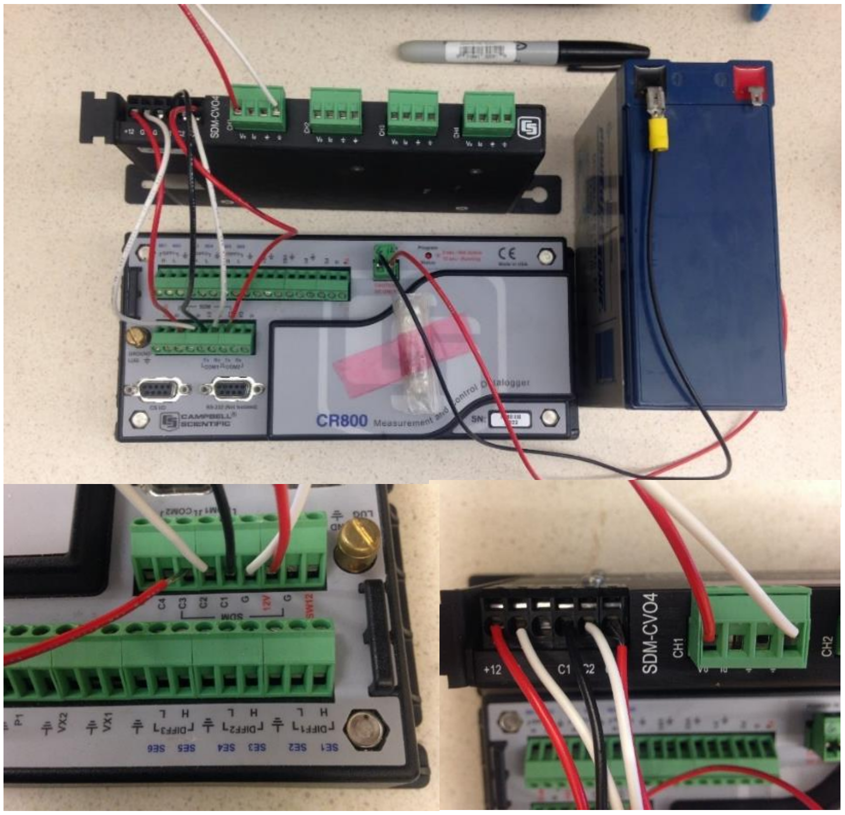

Figure 47. Wiring for datalogger and voltage control module

Once all connections are secured in the spring-loaded blocks of the voltage module and screw blocks of the datalogger, hook up the 12V battery to the power terminal and an RS-232 port to USB. Within the *PC400* software select the correct datalogger and press connect (**Figure 49**). Once the software is successfully connected to the datalogger, hit the “set clock” button to synchronize the datalogger’s clock with the PC’s clock. Then send the desired program to the datalogger. A text version of the program used is included at the end of this appendix and can be pasted into *CR Basic Editor* to create a program if the file is not available. Once sent to the datalogger a message will pop up saying “program compiled” and it will begin to run. This can be confirmed under the “monitor data” tab and by checking the output channels with a voltmeter.

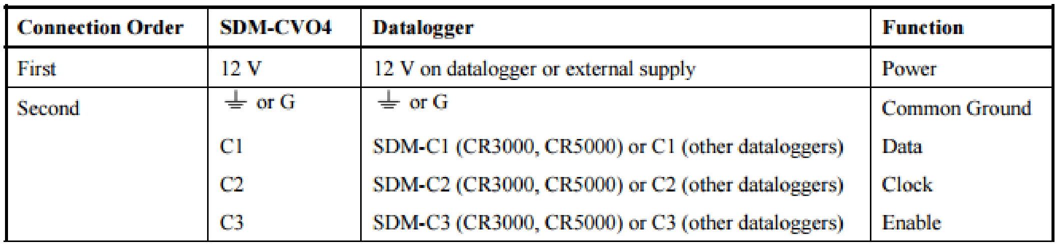

Connection Order	SDM-CVO4	Datalogger	Function
First	12 V	12 V on datalogger or external supply	Power
Second	⏚ or G	⏚ or G	Common Ground
	C1	SDM-C1 (CR3000, CR5000) or C1 (other dataloggers)	Data
	C2	SDM-C2 (CR3000, CR5000) or C2 (other dataloggers)	Clock
	C3	SDM-C3 (CR3000, CR5000) or C3 (other dataloggers)	Enable

Figure 48. Datalogger to voltage module wiring (from Campbell Scientific SDM-CV04 manual)

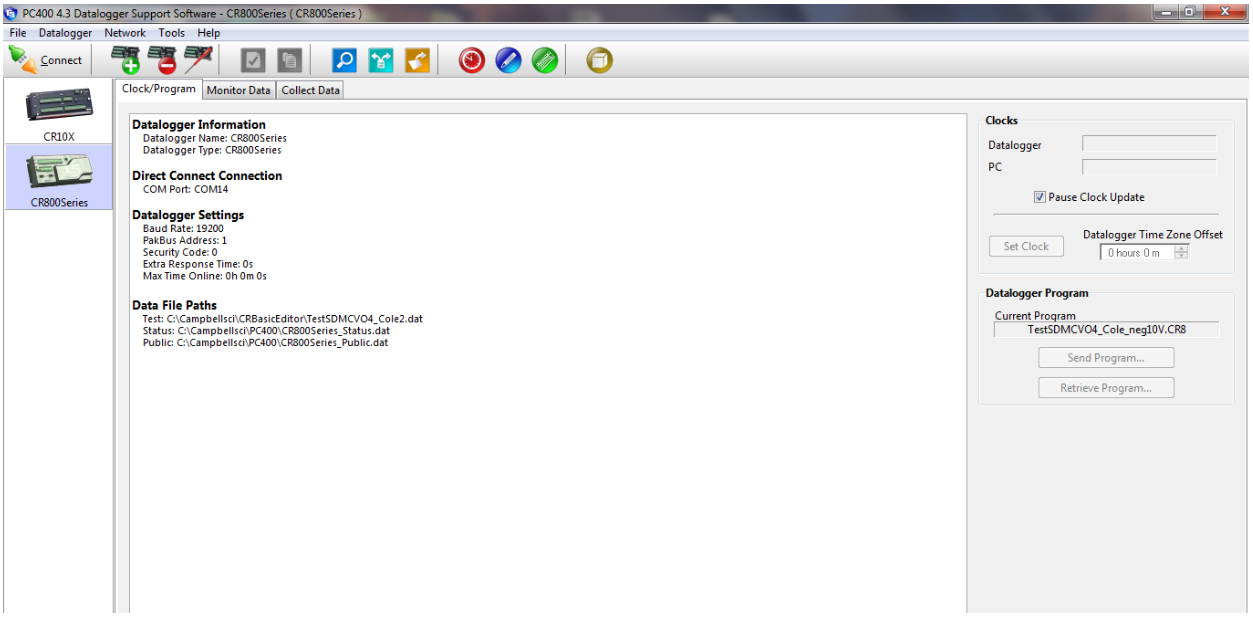

Datalogger Information
Datalogger Name: CR800Series
Datalogger Type: CR800Series

Direct Connect Connection
COM Port: COM14

Datalogger Settings
Baud Rate: 19200
PakBus Address: 1
Security Code: 0
Extra Response Time: 0s
Max Time Online: 0h 0m 0s

Data File Paths
Test: C:\Campbellsci\CRBasicEditor\TestSDMCVO4_Cole2.dat
Status: C:\Campbellsci\PC400\CR800Series_Status.dat
Public: C:\Campbellsci\PC400\CR800Series_Public.dat

☑ Pause Clock Update

Datalogger Time Zone Offset: 0 hours 0 m

Datalogger Program
Current Program: TestSDMCVO4_Cole_neg10V.CR8

Figure 49. Screenshot from PC 400 software homescreen

This program tells the voltage module to continuously output a voltage that varies over time as a sine function for channels 1 and 2. The two channels are offset by pi and centered about the x axis so that while one output is positive, the other is always negative (a negative voltage received by the VFD is treated as zero). The period length can be easily adjusted by changing the value of the constant "Period". Amplitude can also be adjusted this way, but pump flow rates are dependent on the output setting in the VFD (explained below) and head, so adjustments made in the program are not absolute.

<u>VFD Setup</u>

The wiring for an analog input into the VFD is straightforward. It runs in the "standard run, 2 wire" operating mode (see VFD manual, page 3-18). Pin J-24 is the internal 24V return and connects to J-8 to enable operation and J-9 to enable forward motor running. J-8 is connected with an inline switch so that it can be easily shut off (**Figure 50**Error! Reference

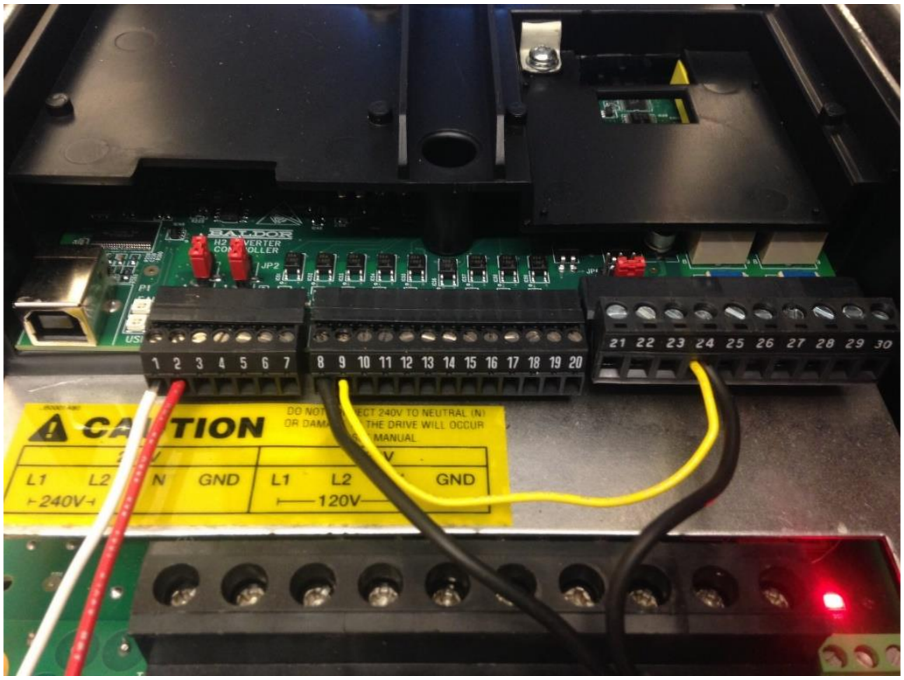

Figure 50. Beneath cover of VFD: J-level pins and correct wiring

source not found.). There are other connections shown in the manual for this operating mode, but only J-8 and 9 are necessary. From the voltage module, the ground connects to J-1 and V_0 connects to J-2. Once it is wired, the operating mode must be set by going on the keypad > level 1 blocks > Input setup > operating mode > standard run 2 wire. Finally, the min and max output parameters should be adjusted to meet desired pumping rates (main > basic parameters). Desired rates are determined through manual keypad operation to find the output speed (Hz is default unit) needed to overcome static head to set as the minimum value and peak flow rate as the maximum value. The motor will run at the minimum output when 0 volts is received as the analog input, at maximum output when 10 volts is received, and scaled linearly for all values in between.

Program Text for CRBasic Editor

```
'CR800 Series Datalogger
'To create a different opening program template, type in new
'instructions and select Template | Save as Default Template
'date:
'program author:

'Declare Public Variables
'Example:
Public PTemp, batt_volt
Public SDMOutput(4)
Public ElapSecs
Public Injection, Withdrawal
'Enter Period in Seconds

'Declare Other Variables
'Example:
'Dim Counter

'Declare Constants
'Example:
Const PI = 3.141592654
Const Period = 60
Const Amp = 10000

'Define Data Tables.
DataTable (Test,1,9999) 'Set table size to # of records, or -1 to autoallocate.
```

```
		DataInterval (0,1,Sec,-1)
		Minimum (1,batt_volt,FP2,0,False)
		Sample (1,PTemp,FP2)
		Sample (2,SDMOutput()/1000,FP2)
		Sample (1,Injection,FP2)
		Sample (1,Withdrawal,FP2)
EndTable

'Define Subroutines
'Sub
		'EnterSub instructions here
'EndSub

'Main Program
BeginProg
		Scan (1,Sec,0,0)
				PanelTemp (PTemp,250)
				Battery (batt_volt)
				'Enter other measurement instructions
				'Call Output Tables
				'Example:
				CallTable Test
				ElapSecs = Timer (1,Sec,0 )
				SDMOutput(1)=Amp*SIN (ElapSecs*2*PI/Period)
				SDMOutput(2)=Amp*SIN (ElapSecs*2*PI/Period+PI)
				Injection = SDMOutput(1)/1000
				Withdrawal = SDMOutput(2)/1000
				SDMCVO4 (SDMOutput(),2,0,0)
		NextScan
EndProg
```

APPENDIX B: MATLAB CODE AND DATA FILES

Included in the CD-ROM "Appendix B" are the injection and drawdown data and the codes used to analyze the data. *SI_sinusoidal_data.mat* is a Matlab® data file containing a data table for each period-length test. Within each table is a column labeled: time (seconds since beginning of pumping), Inj_m3pm (formation injection in cubic meters per minute), and head for each observation well (meters). The three Matlab® script files (*.m) were used to analyze hydraulic responses from the data file above. *Hipass_sinusoid.m* is a routine for filtering the data, computing the FFT, and extracting phase and amplitude values. *Borestore1.m* is a routine which contains the borehole storage analytic solution and compares modeled amplitude and phase from this solution to computed amplitude and phase from the data. *Patsearch_borestore.m* is a routine containing the built-in *patternsearch* optimization method. This minimizes the total error between modeled and actual amplitude and phase in *borestore1*. Comments within the script files contain more specific instructions for their use.

REFERENCES

Ahn, S., and Horne, R.N., 2011, The Use of Attenuation and Phase Shift to Estimate Permeability Distributions from Pulse Tests, *in* SPE Annual Technical Conference and Exhibition, Denver, CO.

Barker, J., 1988, A Generalized Radial Flow Model for Hydraulic Tests in Fractured Rock: Water Resources Research, v. 24, p. 1796–1804.

Barton, C.C., Camerlo, R.H., and Bailey, S.W., 1997, Bedrock Geologic Map of Hubbard Brook Experimental Forest and Maps of Fractures and Geology in Roadcuts Along Interstate 93, Grafton County, NH: USGS Misc. Investigation Series Map I-2562.

Becker, M.W., Ciervo, C., Cole, M., Coleman, T., and Mondanos, M., 2017, Fracture hydromechanical response measured by fiber optic distributed acoustic sensing at milliHertz frequencies: Geophysical Research Letters, v. 44, p. 7295–7302, doi: 10.1002/2017GL073931.

Becker, M.W., Cole, M., Ciervo, C., Coleman, T., and Mondanos, M., 2016, Measuring Hydraulic Connection in Fractured Bedrock with Periodic Hydraulic Tests and Distributed Acoustic Sensing: Workshop on Geothermal Reservoir Engineering, v. 41, p. 1–11.

Becker, M.W., and Guiltinan, E., 2010, CROSS-HOLE PERIODIC HYDRAULIC TESTING OF INTER-WELL CONNECTIVITY: Workshop on Geothermal Reservoir Engineering, v. 35, p. 1–6.

Berger, W.H., 2013, General Overview of the Ice Ages: Calspace Courses, http://earthguide.ucsd.edu/virtualmuseum/climatechange2/01_1.shtml (accessed January 2017).

Bromley, G.R.M., Hall, B.L., Thompson, W.B., Kaplan, M.R., Luis, J., and Schaefer, J.M., 2015, Late glacial fluctuations of the Laurentide Ice Sheet in the White Mountains of Maine and New Hampshire , U . S . A .: Quaternary Research, v. 83, p. 522–530, doi: 10.1016/j.yqres.2015.02.004.

Cardiff, M., Bakhos, T., Kitanidis, P.K., and Barrash, W., 2013, Aquifer heterogeneity characterization with oscillatory pumping: Sensitivity analysis and imaging potential: Water Resources Research, v. 49, p. 5395–5410, doi: 10.1002/wrcr.20356.

Cardiff, M., and Sayler, C., 2016, Strategies for avoiding errors and ambiguities in the analysis of oscillatory pumping tests: Journal of Hydrology, v. 540, p. 1016–1021, doi: 10.1016/j.jhydrol.2016.06.045.

Dressler, K., 2006, SINUSOIDAL EXTRACTION USING AN EFFICIENT IMPLEMENTATION OF A MULTI-RESOLUTION FFT, *in* Proc. of the 9th Int. Conference on Digital Audio Effects, Montreal, Canada, p. 247–252.

Golder Associates, 2010, Fractured Bedrock Field Methods and Analytical Tools:, http://www.sabcs.chem.uvic.ca/May 24 Final FBRock ReportFBFMAT-Vol1.pdf.

Guiltinan, E., and Becker, M.W., 2015, Measuring well hydraulic connectivity in fractured bedrock using periodic slug tests: Journal of Hydrology, v. 521, p. 100–107, doi:

10.1016/j.jhydrol.2014.11.066.

Hollaender, F., Hammond, P.S., and Gringarten, A.C., 2002, Harmonic Testing for Continuous Well and Reservoir Monitoring: SPE Annual Technical Conference and Exhibition, San Antonio, Texas, U.S.A, 29 Sept-2 Oct,.

Johnson, C.D., and Dunstan, A.H., 1998, Lithology and fracture characterization from drilling investigations in the Mirror Lake area, Grafton County, New Hampshire:, http://pubs.er.usgs.gov/publication/wri984183.

Johnson, A.H., Peters, S.P., Brien, J.B.O., and Widmann, B.L., 1996, Stratigraphy and ductile structure of the Presidential Range, New Hampshire: Tectonic implications for the Acadian orogeny: , p. 417–436.

Knudby, C., and Carrera, J., 2006, On the use of apparent hydraulic diffusivity as an indicator of connectivity: Journal of Hydrology, v. 329, p. 377–389, doi: 10.1016/j.jhydrol.2006.02.026.

National Academies of Sciences - Engineering - Medicine, 2015, Characterization, Modeling, Monitoring, and Remediation of Fractured Rock: Washington, DC, The National Academies Press, 2015, doi: 10.17226/21742.

Novakowski, S., 1989, Analysis of Pulse Interference Tests: Water Resources Research, v. 25, p. 2377–2387.

Rabinovich, A., Barrash, W., Cardiff, M., Hochstetler, D.L., Bakhos, T., Dagan, G., and Kitanidis, P.K., 2015, Frequency dependent hydraulic properties estimated from oscillatory pumping tests in an unconfined aquifer: Journal of Hydrology, v. 531, p. 2–16, doi: 10.1016/j.jhydrol.2015.08.021.

Rabinovich, A., Dagan, G., and Miloh, T., 2013a, Dynamic effective properties of heterogeneous geological formations with spherical inclusions under periodic time variations: Geophysical Research Letters, v. 40, p. 1345–1350, doi: 10.1002/grl.50319.

Rabinovich, A., Dagan, G., and Miloh, T., 2013b, Effective conductivity of heterogeneous aquifers in unsteady periodic flow: Advances in Water Resources, v. 62, p. 317–326, doi: 10.1016/j.advwatres.2013.09.002.

Rasmussen, T.C., Haborak, K.G., and Young, M.H., 2003, Estimating aquifer hydraulic properties using sinusoidal pumping at the Savannah River site, South Carolina, USA: Hydrogeology Journal, v. 11, p. 466–482, doi: 10.1007/s10040-003-0255-7.

Renner, J., and Messar, M., 2006, Periodic pumping tests: Geophysical Journal International, v. 167, p. 479–493, doi: 10.1111/j.1365-246X.2006.02984.x.

Rutqvist, J., and Stephansson, O., 2003, The role of hydromechanical coupling in fractured rock engineering: Hydrogeology Journal, v. 11, p. 7–40, doi: 10.1007/s10040-002-0241-5.

Sayler, C., Cardiff, M., and Fort, M.D., 2017, Understanding the Geometry of Connected Fracture Flow with Multiperiod Oscillatory Hydraulic Tests: Groundwater, p. 1–12, doi: 10.1111/gwat.12580.

Tiedeman, C.R., Goode, D.J., and Hsieh, P.A., 1997, Numerical Simulation of Ground-Water

Flow Through Glacial Deposits and Crystalline Bedrock in the Mirror Lake Area , Grafton County, New Hampshire.:

Tiedeman, C.R., and Hsieh, P.A., 2001, Assessing an Open-well Aquifer Test in Fractured Crystalline Rock: Groundwater, v. 39, p. 68–78.

Tsang, C., and Neretnieks, I., 1998, Flow channeling in heterogeneous fractured rocks: Reviews of Geophysics, p. 275–298, doi: 10.1029/97RG03319.

USGS, 2016, Multidisciplinary Characterization of Contaminant Transport in Fractured Rock — Mirror Lake, New Hampshire:, https://toxics.usgs.gov/sites/mirror_page.html (accessed January 2016).

Winter, T.C., 1984, Geohydrologic Setting of Mirror Lake, West Thornton, New Hampshire.: